Development of Iron-Based Soft Magnetic Composites with Novel Coating Materials

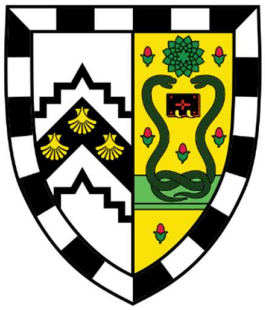

Ben Dyer

Gonville & Caius College

Department of Engineering

University of Cambridge

This dissertation is submitted for the degree of

Doctor of Philosophy

September 2021

Declaration

I declare that, this dissertation Is the result of my own work and includes nothing which is the outcome of work done in collaboration except as declared in the Preface and specified in the text. It is not substantially the same as any that I have submitted, or, is being concurrently submitted for a degree or diploma or other qualification at the University of Cambridge or any other University or similar institution except as declared in the Preface and specified in the text. I further state that no substantial part of my dissertation has already been submitted, or, is being concurrently submitted for any such degree, diploma or other qualification at the University of Cambridge or any other University of similar institution except as declared in the Preface and specified in the text. It contains fewer than 65,000 words including appendices, footnotes, tables and equations but excluding the bibliography and has fewer than 150 figures.

Ben Dyer

September 2021

Abstract

"Development of Iron-Based Soft Magnetic Composites with Novel Coating Materials"

Soft Magnetic Composites (SMCs) are an exciting class of material, with the potential to replace steel laminations as the magnetic core material used in electric motors. The main advantage of SMCs is their isotropic magnetic properties, allowing for radically different design concepts as compared to the 2-dimensional magnetic properties of steel laminations. If this key characteristic can be effectively exploited, SMC materials may provide a step improvement in the performance of electric machines, progressing the global shift towards the electricifaction of transportation methods.

SMC materials consist of a base magnetic powder with an electrically resistive coating. The coating acts to contain eddy currents within each individual powder particle, greatly reducing core losses at increased frequencies. The coated powder is compacted into a solid using traditional powder metallurgy techniques. However, this compaction process induces microstresses into the base magnetic powder which are deleterious to magnetic performance. In order to remove these stresses, the component is subjected to a post compaction heat treatment process. Current coating systems degrade below the annealing temperature of iron, and therefore full stress relief is not achieved. An ideal coating system would be thermally stable above the annealing temperature of iron, as well as being able to form a thin, uniform layer on the surface of the base magnetic powder.

In this work, existing commercially available SMCs were studied to understand the key heat treatment mechanisms. Ancorlam - the flagship magnetic powder produced by GKN Hoeganes - was found to have reduced mechanical strength at high density, where magnetic properties are optimal. At such high densities, there is insufficient porosity for effective thermal oxidation bonding, the mechanism responsible for the increase in strength during heat treatment. A full understanding of the thermal oxidation bonding process was attained and used to increase the cured strength of Ancorlam.

This understanding of current SMCs and their heat treatment mechanisms was used to develop novel coating systems for use with iron-based SMCs. Two separate classes of coating material were developed each with indivudal merits over commercially available Ancorlam; liquid glass-based and silane based coatings. Liquid glass-based coatings produced superior mechanical properties whilst silane-based coatings produced superior magnetic properties. These new coating systems provide key steps in the development of SMCs towards being able to offer greater power density and ultimately enable new applications for electric motors.

Ben Dyer

September 2021

Acknowledgments

First and foremost, I would like to express by profound thanks to my supervisor Dr John Durrell, whose endless enthusiasm and energy have made my time in Cambridge most enjoyable. I am extremely grateful to have had a supervisor with whom I get along so well with and has provided incredible knowledge and all of the support I could have ever wished for. My deep thanks are extended to my second supervisor, Professor Norman Fleck who was instrumental in setting up this project opportunity and providing the early direction for the research.

I am incredibly grateful to Tony Dennis who has acted as a brilliant laboratory manager, accommodating my project so well and the unique experimental challenges it has brought. Tony has in many ways acted as a third supervisor, providing a sounding board for my research problems and guiding me towards the path ahead.

A special mention to Harry Druiff, whose great humour has provided the most enjoyable working environment and helped to keep me on the pathway to success. Many thanks to Graham Smith, Simon Marshall and Alex Casabuena Rodriguez who helped me with compaction, mechanical testing and SEM imaging. I would like to express my gratitiude to Stefan Savage, Terry Stocks and Daniel Flack in the workshop for making special arrangements to accommodate my research through difficult restrictions, without which my project could simply not have gone ahead. A special mention to Len Howlett for accommodating my experimental work in the fume cupboard and for passing on his incredible polishing skills for preparing SEM samples.

I would like to express my apprecitation to the Engineering and Physical Sciences Research Centre for the award of a research council grant and industrial sponsors GKN Hoeganaes for CASE top up funding. GKN have provided both financial, material and academic support, sponsoring numerous trips to their facilities in Germany and the USA in order to further advance my research. A special mention to Kylan McQuaig, Bruce Lindsley, Katie Jo Sunday, Neal Kraus, Dr Lars Wimbert, Alex Wartenberg and all of the team for their regular input to my project.

I would like to thank all members of the Bulk Superconductivity Group, for finding a home for my unique project and welcoming me in from the very beginning.

I would also like to thank Liv for her unwavering support and being instrumental to allowing me to persue my sporting amibitions alongside my research work. Finally, I am eternally grateful to my parents for their ultimate support and guidance in everything I do.

Contents

List of Figures

List of Tables

1 Introduction

1.1 Motivation

Electrical motors are an integral part of the modern world. They are used in a multitude of applications from everyday devices and appliances to industrial processes. Electrical motors can be found at some point in the manufacturing process of every single product. As a result electric motors are the single biggest consumer of electricity, consuming almost half of all global electricity consumption [1]. In effect this means that almost every second power plant is producing electricity for the sole purpose of running electric motors.

Energy consumption from electric motors is expected to rise for the foreseeable future. One particular area for growth is the transportation sector. As of 2017 the transport sector was the largest contributor to UK greenhouse gas emissions, with a share of 28% [2]. UK government plans to phase out sales of conventional gasoline and diesel vehicles by 2040 have been brought forward to 2035, as advised by the Committee on Climate Change (CCC) [3] [4]. Sales of electric vehicles have risen accordingly, with ultra-low emission vehicles accounting for 2.7% of all new car registrations in 2018, an order of magnitude increase in five-years [5].

A similar shift towards greener travel is also required in the air transportation sector, with passenger numbers forecast to double over the next twenty years [6]. Currently there are no electric nor hybrid transoceanic passenger aircraft owing to the high energy density requirements of the jet engine. Aircraft electrical systems operate at a higher frequency than the standard 50 Hz found in most appliances to allow for reduced mass and volume of components. The current practical limit is around 400 Hz, above which magnetic losses become too large resulting in overheating of components. Increasing the efficiency of electric motors at these frequencies is a key enabling factor for the advent of electric aircraft and greener air transportation.

At the heart of all electric motors is a soft magnetic core material which acts to transmit magnetic flux. These soft magnetic materials generate core losses through hysteresis, eddy current and anomalous losses. Thus, an ideal soft magnetic material combines high resistance and saturation magnetisation with a low coercive field. However, it is difficult to find a material which exhibits all of these properties. Currently most motor designs use laminated cores, comprised of steel laminations with insulating materials or air gaps between each layer. The insulating coating reduces current flow from one layer to another in order to minimise eddy current losses. These materials have been optimised by minimising the thickness of each lamination layer. However, a limit has been reached where manufacturing costs and complexity sharply increase with further reductions in lamination thickness.

Soft magnetic composite (SMC) materials are an alternative technology which do not possess this limitation. These are composite materials made from particles of a magnetic powder coated with an electrically insulating coating, which are compacted under high pressure using traditional powder metallurgy techniques. Such techniques allow for significantly reduced dimensions of conducting material, therefore reducing core loss and ultimately improving electrical efficiency. Further advantages of SMCs include, but are not limited to; three-dimensional isotropic ferromagnetic behaviour, thermal isotropy, structural freedom for complex part designs, reduced weight and increased material utilisation [7] [8].

SMC materials have the potential to bridge the gap between traditional laminated cores and ferrite cores, illustrated in Figure 1. Laminated cores possess high magnetic flux density but are limited to low operating frequencies, whilst ferrite cores are able to withstand very high frequencies but possess low magnetic flux density.

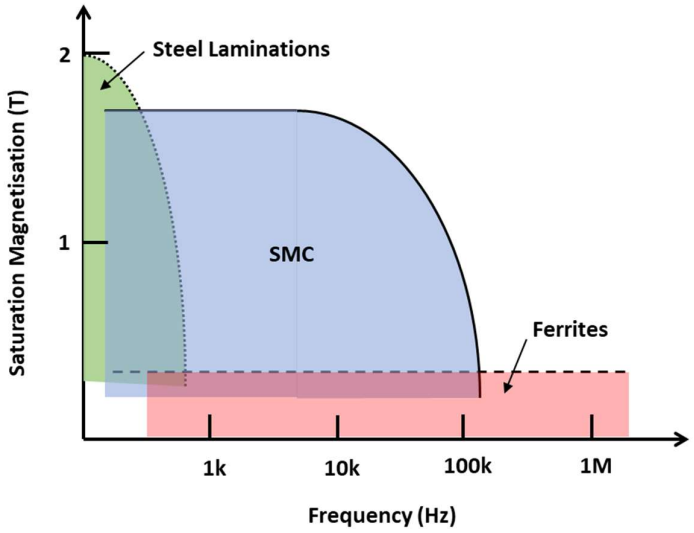

Figure 1: Operating regions of soft magnetic materials, adapted from [7].

Currently the electric motor is designed around the principle that steel laminations possess 2D magnetic isotropy. Furthermore, magnetic flux density decreases with depth from the surface of the laminated core due to the skin effect of the iron core material. Therefore, the laminated iron core can only be used at a magnetic flux density below the saturation magnetisation [9]. As skin effect is most prominent at low frequency, this is an issue in laminated steels which is minimised in SMC material operating at higher frequency.

SMCs have exciting potential as their 3D magnetic isotropy can be used to re-design electric motor structures with a 3D circulation of magnetic flux thus improving power to weight ratio [10]. Furthermore, SMCs possess 3D thermal isotropy thus the heat flux path is 3D and the whole external

surface of the electric drive can be used for heat dissipation, reducing issues of overheating [11]. Finally, SMCs are produced by powder compaction, which allows for both reduced production steps and greater freedom of design as more complex shapes can be produced in comparison with traditional steel laminations [12]. Thus, if SMCs can be proven to be superior to their alternatives at low to mid-range frequencies, manufacturers will be more inclined to invest in this new technology and re-design applications to exploit their unique properties.

1.2 Thesis Scope and Aims

The predominant limiting factor in the performance of soft magnetic composites is the thermal stability of the coating material. The compaction process induces dislocations and microstrain in the core material, increasing coercivity and degrading the magnetic properties of the final composite [13]. Eliminating these deleterious effects requires annealing of the material. However, current coatings degrade below the required annealing temperature, so full relief is not possible. Degradation of the coating material leads to metal-on-metal contact between the ferromagnetic powder particles, reducing resistivity and creating large eddy current paths. These eddy currents increase core losses and may lead to overheating of the component [7]. Thus, a coating material with increased thermal stability is required to allow for full stress relief of the compacted core material without degradation of the coating.

The objective of this research is to develop soft magnetic composite materials with high magnetic saturation, high magnetic permeability, low core loss and high mechanical strength for use in the 50 – 1000 Hz frequency range. In this frequency range, hysteresis losses are dominant and hence coercivity must be minimised through effective heat treatment.

Therefore, a new coating system is sought which can survive the necessary temperatures required for full stress relief of the compacted powder. Increased curing temperature will also give the potential for greater strength and permeability, which are inferior in SMC materials in comparison to their laminated steel competitors [14] [15] [16]. In addition to increased thermal stability, the ideal coating would also be magnetic to retain overall magnetic volume of the composite material. The scope of developing a new coating system covers the physical, morphological, electrical and chemical properties such as thickness, surface coverage, porosity, structure, strength, cohesion to the matrix, resistivity and chemical durability after treatment. This thesis will focus on developing a new coating system through a number of different coating materials and processes.

1.3 Thesis Outline

The aim of the research was to improve understanding of the SMC production process and then use this to develop new coating systems with improved properties over existing commercially available SMC materials.

In Chapter 2, the physical phenomena of magnetism and the key parameters pertaining to magnetic performance are introduced. An overview of powder metallurgy and the main processing steps is provided. Soft magnetic composite materials are introduced together with a review of current core powder and coating materials. The key requirements and challenges of designing an effective coating system are discussed.

In Chapter 3, the various processing methods to manufacture SMCs are presented, including mixing, coating, compaction and heat treatment. Experimental methods are described for subsequent analysis and testing of the produced SMC materials, including microstructural and chemical analysis, and magnetic, electrical and mechanical testing.

In Chapters 4, 5 and 6 the experimental results are presented and analysed. Each chapter starts with a literature review of the most relevant research papers. The results of the experimental work are presented in turn with a discussion of the findings. Figure 2 illustrates the process flowchart used in SMC development using blue boxes. The contribution to new knowledge is highlighted in green boxes which list the key variables investigated and techniques used to evaluate these new SMC materials.

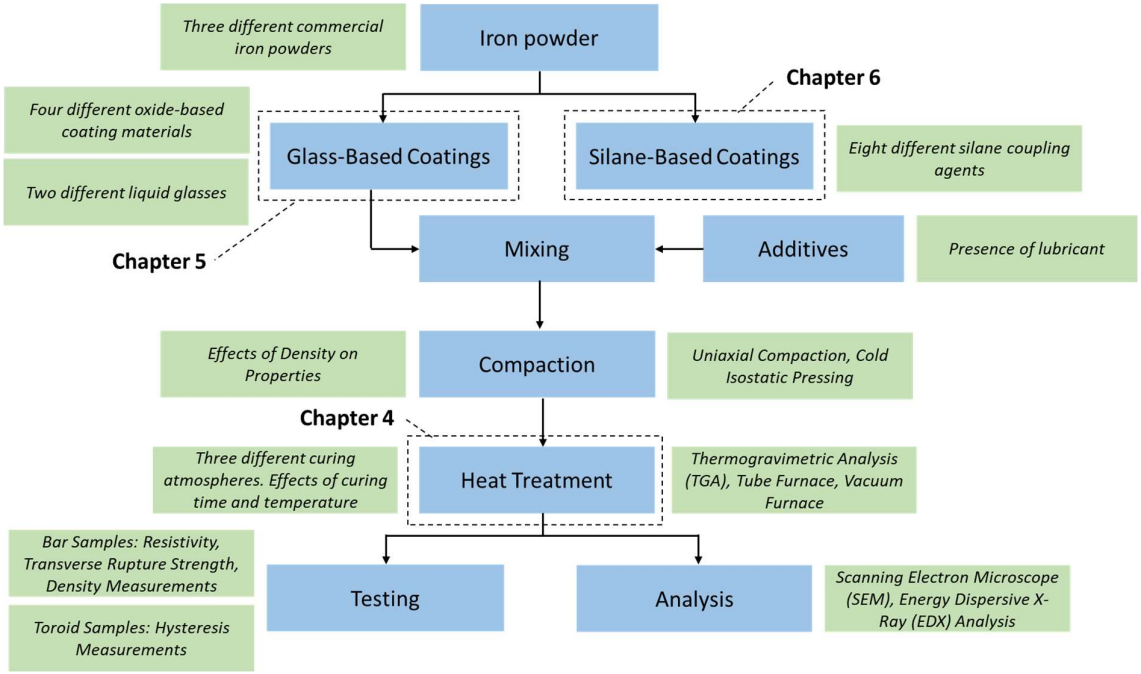

Figure 2: Process Flowchart of Experimental Work

In Chapter 4, the unexpected drop off in strength of commercially available Ancorlam powder at very high density was investigated. This led into a study of the heat treatment mechanisms of current SMC materials and the factors that most influence the curing process. This knowledge was used to tailor the heat treatment process to produce samples with increased mechanical strength.

In Chapter 5, the greater understanding of current SMC materials obtained in Chapter 4 was used to develop a new coating system. This coating system was based on the use of liquid glass as a binder material within which to disperse resistive nanoparticles. Liquid glass exhibits the additional benefit of acting as a binder material, thus contributing to the mechanical strength of the SMC material.

In Chapter 6, a second class of coating system was investigated, utilising silane coupling agents. Silanes were used in conjunction with other coating materials to produce a well adhered, thin and highly resistive coating system. This new coating system was applied to the base iron powder to produce SMC materials with superior magnetic properties to current commercially available powders.

In Chapter 7, the primary findings of each experimental chapter are discussed. The two new classes of coating system are compared to one another and commercially available SMC materials as a benchmark. Lastly, future work to be completed as a continuation of this thesis is recommended.

2 Background

2.1 Magnetism

The origin of magnetism lies at a sub-atomic level, in the spin and orbital motions of electrons and their interactions with one another. The spin of an electron refers to the rotation of the electron around itself, whilst the orbital motion of an electron refers to the movement of the electron around the nucleus of its atom. The spin and orbital motions of electrons give rise to magnetic moments, similar to an electric current circulating in a coil to produce a magnetic field. The direction of the motion of electrons defines the direction of the magnetisation in a material. The nucleus of an atom may also possess spin motion, but the corresponding magnetic moment is three orders of magnitude smaller than that of the electrons, as the magnitude is inversely proportional to the particle mass [17]. Therefore, we can neglect the magnetic moment of the nucleus.

2.1.1 Types of Magnetic Material

All materials are magnetic, only some are more magnetic than others. The difference depends on the existence and alignment of magnetic moments with or without the application of a magnetic field. Five types of magnetism can be defined; diamagnetism, paramagnetism, ferromagnetism, ferrimagnetism and antiferromagnetism [17].

Diamagnetism is a weak form of magnetism which arises only when an external magnetic field is applied. The applied field perturbs the orbit of the electrons and contributes to an additional component of angular momentum. This induced effect gives rise to a very small opposing magnetic moment, known as diamagnetism. All materials have a diamagnetic response, but it is only apparent in the absence of a stronger magnetic interaction.

Paramagnetism occurs in materials in which unpaired electrons give rise to permanent magnetic dipoles. However, in the absence of a magnetic field these individual dipoles are randomly aligned, resulting in no net magnetisation. When a magnetic field is applied, the dipoles align in the direction of the field resulting in a small net magnetisation.

In diamagnetic and paramagnetic materials, a net magnetisation occurs only in response to an externally applied field. However, ferromagnetic materials possess permanent magnetic moments even in the absence of an external field. This effect is due to uncancelled electron spins within their electron structure. The coupling interactions of electron spins of adjacent atoms cause alignment of magnetic moments. Regions where magnetic moments are aligned in the same direction are known as magnetic domains. The magnetisation of these domains will be discussed further in Section 2.2.

Antiferromagetic materials share mechanistic features with ferromagnetic materials but result in a much weaker interaction. In ferromagnetic materials, adjacent electron spins align in parallel to one another. However, in antiferromagnetic materials these adjacent electron spins align antiparallel to one another, thus cancelling each other out. Antiferromagnetic materials can be visualised as two interlocking sublattices of equal and opposite spontaneous magnetisation. Hence, if no external field is applied there is no net spontaneous magnetisation. In the presence of an applied field, the absolute value of one sublattice will differ slightly from that of the other, resulting in a small net magnetisation.

Similarly to antiferromagnetic materials, ferrimagnetic materials can be visualised as two interlocking sublattices only with each sublattice having different dipole moments. This results in incomplete cancellation and thus a net spontaneous magnetisation. In many respects ferrimagnetic materials behave like ferromagnetic materials, but with a lower net magnetisation.

For the purpose of this thesis the discussion is focused on ferromagnetic materials, in particular iron.

2.1.2 Magnetisation

When an external field is applied to a ferromagnetic material, the dipoles of individual atoms interact with and line up in the direction of the applied field. This realignment of dipoles provides an amplification of the applied field and results in a large magnetisation for relatively small applied fields. A region where all dipoles are aligned is referred to as a magnetic domain. The magnetisation of a ferromagnetic material from its demagnetised state to saturation magnetisation includes different magnetisation processes such as domain wall motion and domain rotation, both of which can be reversible or irreversible.

In a material, grain boundaries and imperfections act as pinning sites which hinder domain wall motion. For a small applied field, the domain wall is unable to rotate and instead it will bow around the pinning site. If the field is removed, the bowing terminates and the domain wall returns to its original orientation and thus this type of domain wall rotation is reversible. For increased applied fields, the domain wall releases from the pinning site and jumps to a new site. This domain wall motion is irreversible and results in a steep rise in magnetisation as all dipoles in the area between the original and new site change direction.

A sufficiently large applied field causes all domain walls to vanish due to the irreversible domain wall motion. Further increase in the applied field causes reversible domain rotation until fully aligned with the applied field. When all domains are aligned with the applied field the material is said to have reached saturation magnetisation.

2.1.3 Magnetic Induction

In practical applications the magnetic field is commonly characterised by the magnetic induction ***B***. Inside a material the magnetic induction is related to the applied magnetic field ***H*** and the total volumetric magnetic moment ***M*** (herein referred to simply as magnetisation) induced in the material by equation 2.1 [18].

$$\boldsymbol{B} = \mu_o (\mathbf{H} + \mathbf{M}) \qquad (2.1)$$

where $\mu_o = 4\pi\, x\, 10^{-7}\ \mathrm{H/m}$ is the permeability of free space. Magnetic induction ***B*** has units tesla (T) equivalent to $\mathrm{Wb/m^2}$, permeability μ_o has units $\mathrm{H/m}$, and magnetic field ***H*** and magnetisation ***M*** have units $\mathrm{A/m}$. The unit H is the Henry which is equivalent to $\mathrm{Wb/A}$. Note equation 2.1 holds true only in S.I. units and is not applicable for other unit systems.

2.1.4 Magnetic Permeability

Magnetic permeability is a physical property which characterises the degree of induced magnetism a material experiences under the influence of an external magnetic field. In the S.I. unit system, the permeability is referred to as the absolute permeability of the medium. Absolute permeability μ can be defined as the ratio of the magnetic induction ***B,*** established in a material by a magnetising field to the magnetic field strength ***H*** of the magnetising field, as given in equation 2.2.

$$\mu = \boldsymbol{B}/\boldsymbol{H} \qquad (2.2)$$

In the S.I. unit system, the units of permeability μ are H/m, magnetic induction ***B*** are $\mathrm{Wb/m^2}$ and magnetic field ***H*** are $\mathrm{A/m}$.

In simple terms, magnetic permeability measures the ability of a material to become magnetised. It is thus desirable for a magnetic material to have a high magnetic permeability. Any defects or nonmagnetic inclusions in the material greatly hinder the domain wall motion, making it more difficult to magnetise and thus reduce permeability.

For soft magnetic composites operating under AC frequencies, permeability can be measured from the required H-field to reach a set induction. In this thesis, the AC permeability is measured by the B-field of 1 T divided by the required H-field to reach an induction of 1 T, as illustrated in Figure 3.

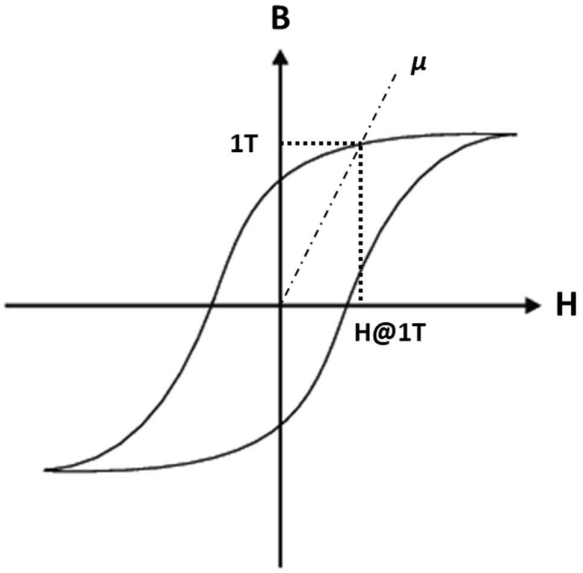

Figure 3: AC permeability of SMC materials, modified from [19]

2.1.5 Hysteresis Loop

When a ferromagnetic material is magnetised to saturation magnetisation $\boldsymbol{M_s}$ and the applied field is then removed, the material does not revert back to its initial demagnetised state. Domains will remain aligned in the direction of least energy causing a net magnetisation, known as remnant magnetisation $\boldsymbol{M_r}$. A reverse field applied in the opposite direction is required to reduce the magnetisation back to zero, known as the coercive field $\boldsymbol{H_c}$. If an alternating magnetic field is applied, the magnetisation of that material will trace out a hysteresis loop, as illustrated in Figure 4. The magnetic domain structures are illustrated at the initial unmagnetised state, the saturated state, the remnant state in zero field and the state at $\boldsymbol{H = -H_c}$ where the magnetisation returns to zero.

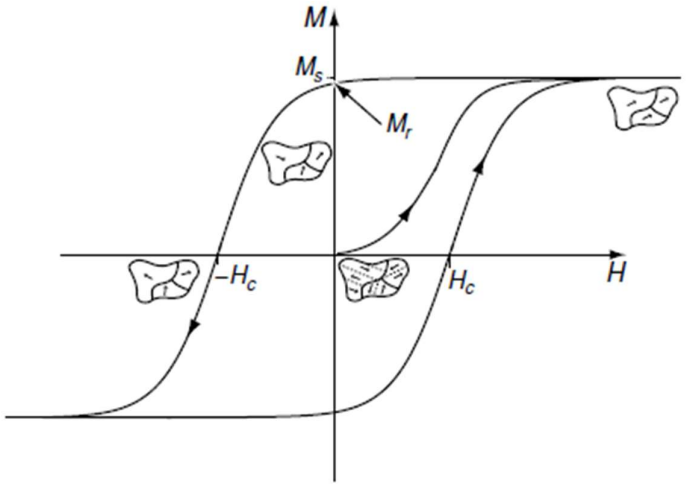

Figure 4: Schematic of ferromagnetic material hysteresis loop [17]

Magnetic properties including permeability, coercivity and saturation magnetisation are influenced by microstructural defects, chemical impurities and magnetic energies [20]. Magnetic energies include magnetostatic, magnetocrysalline and exchange energy which all compete with each other to form an internal magnetic domain structure. When an external field is applied, a fourth external energy known as Zeeman energy competes to align the magnetic spins with the applied field [21]. These external magnetic energies are heavily influenced by the composition and microstructure of the material.

Microstructural defects including dislocations and grain boundaries impede domain wall motion and hence are detrimental to magnetic properties of a soft magnetic core material. Coarser particle sizes allow for fewer grain boundaries which reduces coercivity and hence hysteresis losses. Furthermore, coarser particles allow for improved densities which reduces nonmagnetic inclusions and air gaps, maximising the overall magnetic volume and magnetic saturation [22].

Magnetic materials can be classified as either soft or hard based on how easily they can be magnetised and demagnetised [23]. Hard magnetic materials are more difficult to magnetise, but retain their magnetism after the applied field is removed and therefore are used as permanent magnets. Hard magnetic materials have high coercivity (typically in the order of 10 kA/m or greater) and produce broad, square ***M(H)*** loops. Soft magnetic materials are easily magnetised, but readily lose their magnetisation once the applied field is removed, thus are often used in temporary magnets. The main advantage of soft magnetic materials is that only a small amount of energy is dissipated when repeatedly reversing the magnetisation, hence they are useful in AC applications. Soft magnetic materials have low coercivity (typically in the order of 1 kA/m or lower) and possess narrow ***M(H)*** loops. This thesis is concerned exclusively with soft magnetic materials.

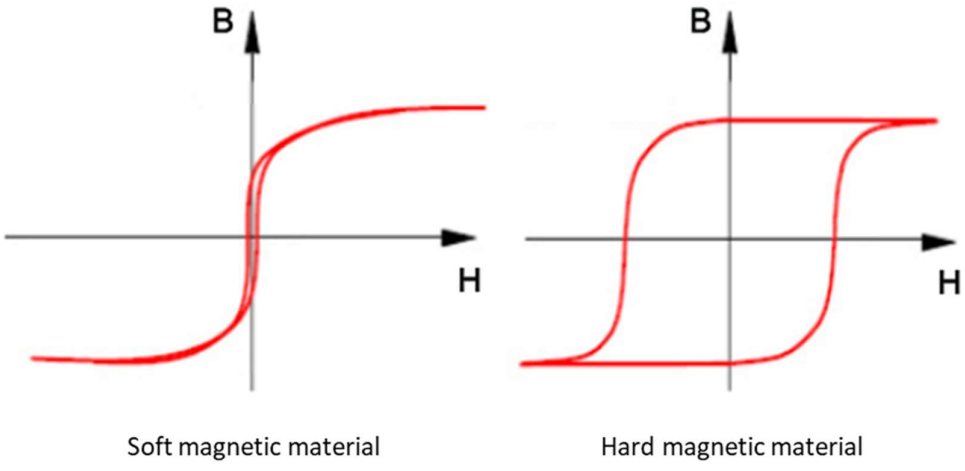

Figure 5: Hysteresis loop of soft versus hard magnetic material, adapted from [24].

The most common method of characterising a magnetic material is by measuring the hysteresis response using a toroid sample, often referred to as a hysteresisgraph [25]. This method will be covered in Section 3.2.2.

2.1.6 Core Losses

Core losses reduce magnetic performance, particularly at high frequencies, requiring more power to maintain a similar flux density than at lower frequencies. Soft metallic materials experience three main sources of core losses; hysteresis losses, eddy current losses and anomalous losses [17]. The total core loss P_{total} can be expressed by equation 2.3.

$$P_{\text{total}} = P_h + P_e + P_a \quad (2.3)$$

where P_h is the hysteresis loss, P_e is the eddy current loss, and P_a is the anomalous loss component.

2.1.7 Hysteresis Losses

Hysteresis losses occur due to energy expended during the rotation of magnetic domains. In an alternating applied field the domains rotate at the frequency of the applied current, hence hysteresis loss is directly proportional to the applied frequency. Hysteresis losses can be expressed by equation 2.4 [26]:

$$P_h = f \int \boldsymbol{H}\ d\boldsymbol{B} \quad (2.4)$$

where P_h is the hysteresis loss, f is frequency, $\boldsymbol{H}$ is magnetic field strength and $\boldsymbol{B}$ is magnetic induction. The hysteresis loss component is equivalent to the area inside the ***B-H*** hysteresis loop. Hysteresis losses are dominant at low frequency, hence for low frequency applications the coercive force must be minimised. In iron powders three main factors influence coercivity; impurities, grain boundaries and dislocations, as depicted in Figure 6.

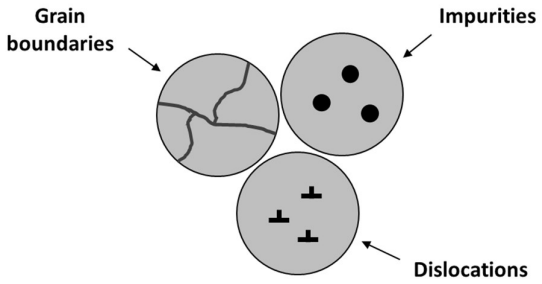

Figure 6: Schematic of hysteresis loss control factors, adapted from [27].

These three factors give rise to pinning sites which hinder domain movement, increasing the coercive force. Hysteresis losses can therefore be reduced by using larger particle sizes, higher purity iron powder and through post-compaction heat treatment to remove residual stresses.

2.1.8 Eddy Current Loss

Eddy currents are current loops induced in conductors by a changing magnetic field. Eddy currents flow in closed loops perpendicular to the direction of the applied magnetic field. This creates a magnetic field which opposes change to the original applied field. In the case of an alternating electric field, the currents flowing through the conductor dissipate energy as heat. Eddy current loss can be expressed by equation 2.5 [26]:

$$P_e = (CB^2 f^2 d^2)/\rho \qquad (2.5)$$

where P_e is the eddy current loss, C the proportionality constant, $\boldsymbol{B}$ the magnetic induction, f the frequency, d the thickness of the material, and ρ is the resistivity of the material. In the case of SMC materials, the thickness of the material is hard to define due to the irregular particle shape and size. Therefore, eddy losses are determined by the loss separation method, discussed in Section 2.1.10.

It can be noted from equation 2.5 that eddy currents are proportional to the square of the frequency, hence are dominant at high frequency. Large eddy currents lead to failure due to excessive heating of the material. Eddy currents in powder-based components can be classified in two ways, intra-particle or inter-particle as illustrated in Figure 7. The former relates to eddy currents flowing within single powder particles, whilst the latter related to currents flowing throughout the cross section of the component.

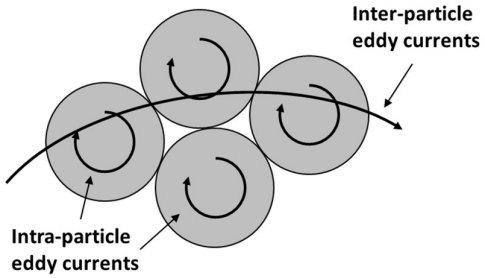

Figure 7: Schematic of eddy current loss control factors, adapted from [27].

Conversely to hysteresis losses, impurities, internal defects and smaller grain sizes all act to reduce eddy current losses by introducing resistive barriers between particles. In practise, this results in a larger proportion of inter-particle eddy currents and fewer intra-particle eddy currents. Therefore, a trade-off is required between minimising hysteresis and eddy current losses depending on the frequency of the desired application. For low frequency applications hysteresis losses must be minimised, whilst for high frequency applications eddy current losses must be minimised.

2.1.9 Anomalous Losses

Anomalous losses are by definition whatever remains after hysteresis and eddy current losses have been taken into account and were first proposed by Bertotti et al. [28]. These losses result in additional broadening of the hysteresis loop as frequency is increased, beyond that expected by eddy current losses. Anomalous losses arise from additional eddy current losses caused by domain wall movement, sample inhomogeneity and non-uniform magnetisation. Anomalous losses can be reduced by using a structure with many parallel domain walls in order to decrease the distance the walls must move during the magnetisation process [17].

2.1.10 Separation of Loss Contributions

Separating the contributions of hysteresis, eddy current and anomalous losses allows for better understanding of the core losses. The total core loss P_{total} can be expressed as the sum of each component as per equation 2.3 [7].

Anomalous losses are only significant at very low induction levels and very high frequencies thus are negligible for power applications [7]. For soft magnetic composites aimed at low to medium frequency, hysteresis and eddy current losses are dominant [29]. Therefore, in the scope of this thesis anomalous losses can be ignored.

The hysteresis and eddy current loss contributions are given in equations 2.4 and 2.5 respectively, with hysteresis a function of frequency and eddy current a function of frequency squared. Therefore, the expression for total core loss can be rewritten as a function of the hysteresis loss coefficient and eddy current loss coefficient as per equation 2.6 [30]:

$$P_{\mathrm{total}} = P_{\mathrm{h}} + P_{\mathrm{e}} = K_{\mathrm{h}} f + K_{\mathrm{e}} f^2 \qquad (2.6)$$

Where K_h is the hysteresis loss coefficient, K_e is the eddy current coefficient, and f is the frequency. Figure 8 shows the individual power loss contributions of hysteresis and eddy current losses. At low frequencies ($f \leq 50$) hysteresis losses are dominant, thus under the assumption that eddy current losses are negligible at this frequency, the individual coefficients can be calculated from the total core loss [31]. These coefficients can be used to determine the changing contributions of the hysteresis and eddy current losses as frequency is increased.

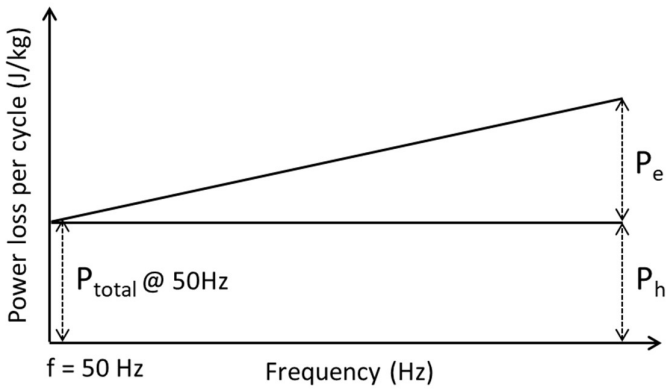

Figure 8: Hysteresis and eddy current power loss contributions

2.2 Powder Metallurgy

Powder metallurgy is the study of the processing of metal powders, including the production, characterisation, compaction and post-processing of these powders into useful engineering components. R.M. German defines a powder as a finely divided solid, with maximum dimension less than 1000 microns (1 mm) [32]. The majority of metal particles used in powder metallurgy are in the size range of 5 to 200 microns [33]. Traditionally, power metallurgy has been concerned with purely metal powders, but these are becoming increasingly combined with other materials such as ceramics or polymers.

2.2.1 History

The origins of powder metallurgy date back thousands of years. The Egyptians heated iron ore to produce iron powder for making tools back in 3000 BC. One example still standing today is the Delhi column in India, fabricated from 6.5 tons of reduced iron powder dating back to 300 AD [32]. Sintering of metals was then largely forgotten during the succeeding centuries, until various methods of platinum production were recorded in Europe at the end of the 18th Century [34]. Powder metaullurgy was used in the 1800's during the industrial revolution as a means to overcome inadequate temperature capabilities required by other processes. In the 1940's, several less common materials were produced from powders, and with it powder metallurgy experienced a shift from being selected for being a low cost method, to one increasingly selected for high quality and homogeneity of properties. Today powder metallurgy is being increasingly utilised in research applications to produce materials with unique properties.

2.2.2 Advantages

The main advantages of using powder metallurgy over conventional metal forming processes are:

- High material utilisation, avoiding or reducing scrap metal

- Complex geometries can be produced to near final shape and size
- Utilises automated processes with low capital costs
- Lower energy consumption and short overall production time due to fewer machining operations
- Allows for components with unique properties and microstructure which cannot be fabricated otherwise (porous metals, oxide dispersion strengthened alloys and cemented carbides).
- Allows for materials which are otherwise difficult to process due to being a relatively low temperature processing method, therefore avoiding microstructural damage caused by elevated temperatures (reactive and refractory metals or amorphous metals).

Powder metallurgy is most competitive in the mass production of complex parts. At high volume, the cost per component is considerably lower than traditional methods such as machining [32].

2.2.3 Processing Steps

There are four main steps to the powder metallurgy process; powder fabrication, mixing, compaction and sintering. Secondary operations such as sizing, machining or alternative heat treatments may be applied after sintering to improve performance and mechanical tolerances. These steps shall be described in turn in the following sections. A schematic of the powder metallurgy manufacturing process is given in Figure 9.

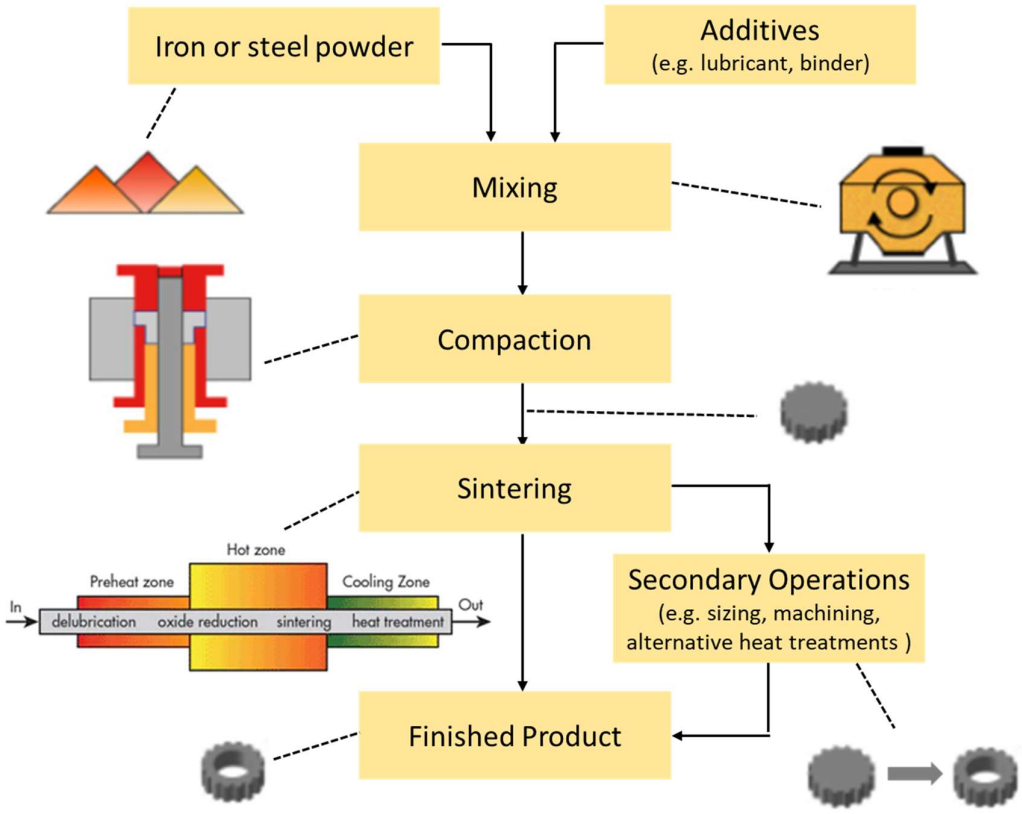

Figure 9: Schematic overview of PM manufacturing process, adapted from [35].

2.2.4 Powder Fabrication

The powder fabrication process influences the size, shape, microstructure, chemistry and cost of the powder. There are three main categories of powder fabrication techniques [33]:

- Mechanical, including: machining, milling and mechanical alloying.
- Chemical, including: electrolytic deposition, decomposition of solid by gas, thermal decomposition, precipitation from liquid or gas and solid-solid reactive synthesis.
- Physical, including atomisation techniques.

The theory behind all methods of powder fabrication is based on the delivery of energy to the material to create new surface area. Due to the relatively large net surface area of the final powder, the energy cost is high. Consider the reduction of 1 m^3 of metal into 1 micron diameter spherical particles. This would yield nearly $2x10^{18}$ particles with a net surface area of approximately $6x10^6$ m^2 [32]. Consequently, powder production processes must be economic in order to remain competitive.

This thesis is primarily concerned with the production of iron powder, which for economic reasons is most-commonly produced by either a solid state reduction process (also known as the sponge iron process) or a water atomisation process [36].

The sponge iron process is essentially a solid state oxide reduction reaction. Finely divided high purity iron ore (Fe_3O_4) and a reduction mix comprising coke and limestone are heated to around 1200°C [37]. When the coke is heated, carbon monoxide is formed which reacts with the iron ore reducing it to metallic iron, whilst limestone binds the sulphur contained in the coke. The iron particles sinter together to form porous iron sponge. The produced powder is then cleaned, crushed and milled into crude powder and subsequently annealed at 800-1000°C in hydrogen to reduce carbon and oxygen contents to very low levels. Finally, the powder is milled and sieved to produce irregularly shaped particles each containing internal pores, hence the term “sponge” powder.

The water atomisation process uses scrap iron and sponge iron from the reduction process [37]. The iron is melted in a furnace and released through a nozzle to create a stream of molten metal. This stream is separated into small droplets by a high-pressure liquid or gas spray, and subsequently frozen rapidly before the droplets come into contact with each other or a solid surface. The two main types, namely water and gas atomisation refer to the type of spray used. The resultant particles are hard and covered by surface oxides, due to the rapid cooling rates and rich levels of oxygen present. Therefore, the powder is annealed to soften the material and reduce the amount of surface oxides. The powder is then milled and sieved to create the final press ready product. Water atomised powder particles are smaller, cleaner, non-porous and have a greater range of particle sizes, which allows for better compaction behaviour. Water atomised powders have an irregular particle shape whilst gas-atomised powders typically have spherical or pear shape particles [38].

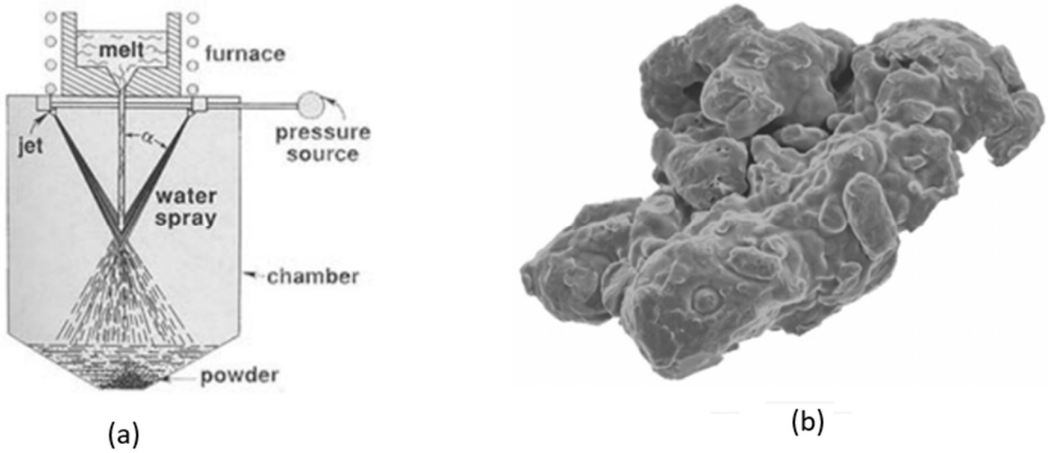

Figure 10: (a) Water-atomisation process [32]; (b) Powder produced by water-atomisation [36]

2.2.5 Mixing

Mixing of the metal powders and additivites prior to compaction allows for uniform distribution of the constituents and subsequently results in 3D magnetic and thermal isotropy in the final component.

Dependent on the application, the base powder may be mixed with alloying particles e.g. copper or chromium. An organic or metallo-organic lubricant is added to the powder mix, or alternatively applied directly to the die wall, in order to minimise friction effects. This includes friction between contacting particles to achieve higher pressed densities, and friction between particles and the die wall to allow for lower ejection pressures. An optional binder material may also be added to glue lubricants or other additives to the iron particles and increase green strength (strength after pressing) [32]. Both lubricants and binders are burned out of the compacts during sintering. In industry, large scale mixers allow for capacities of several tons, however in most research laboratories this procedure is scaled down to batches of a few hundred grams [39]. Typical laboratory apparatus includes ball mills, double cone mixers, shear mixers and acoustic mixers.

2.2.6 Compaction

Powder compaction is the process of compacting metal powder in a die through the application of high pressures. The aim of the compaction process is to produce a shaped component with sufficient strength for subsequent handling and heat-treatment. Typical compaction pressures are in the range of 600 - 1000 MPa [7] [31]. Smaller grain sizes and harder materials are less compressible and hence require compaction pressures in the upper end of this range. The die is comprised of a rigid die cavity filled with powder, which is compacted between two or more axially moving upper and lower punches. The die cavity will be shaped as to require little to no additional shaping after compaction. The compaction process involves three densification mechanisms; particle redistribution, elastic deformation and plastic deformation as illustrated in Figure 11.

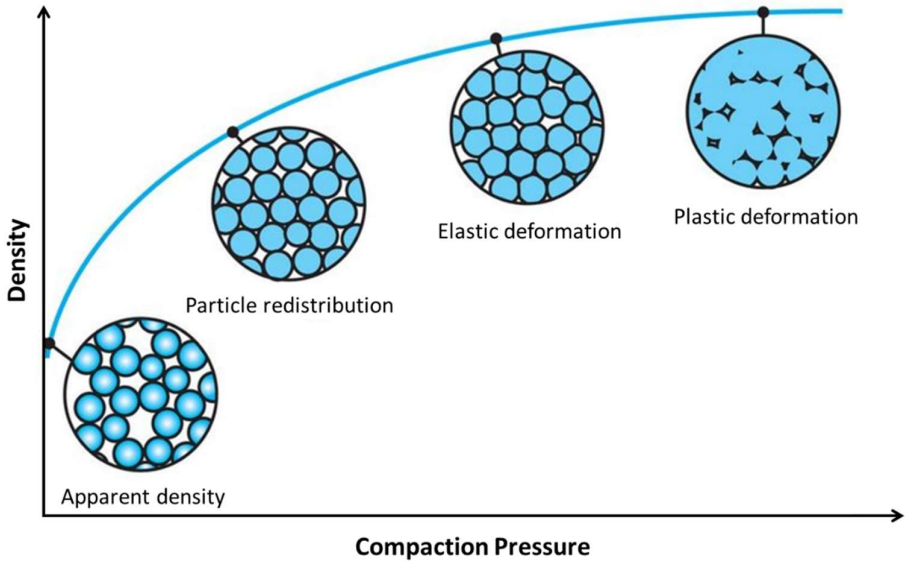

Figure 11: Schematic of compaction process, adapted from [40]

Particle redistribution serves to reduce air gaps during pressing, aided by the addition of pre-mixed lubricant allowing particles to move over one another. Subsequent elastic and eventual plastic deformation of the particles minimises porosity and leads to the development of inter-particle bonds. The resulting strength of an as-compacted sample is referred to as the green strength. The compaction process can be performed either at room temperature or slightly elevated die and/or powder temperatures to aid densification. In heated powder mixes the yield strength of the powder drops, which reduces the resistance to plastic deformation and increases compressibility. This positive influence of temperature on the resistance to plastic deformation holds true for all ferrous materials with ferritic structures [41].

Alternatively, components can be compacted using isostatic pressing. The metal powder is placed in a flexible mould and high pressure gas or fluid is applied to the mould. Isostatic pressing is mainly limited by the increased processing time and lower compaction pressures.

2.2.7 Sintering

Sintering is the process of particles bonding at temperatures below their melting point due to atomic diffusion across particle boundaries. Sintering is performed to consolidate the as-pressed component (green compact) into the final component with the required composition and properties. Any lubricant or binder additives used in the compaction process are burned off during the sintering process. According to Sauerwald [42], who first proposed the sintering theory in 1922, sintering comprises two steps: adhesion and recrystallisation. Adhesion is the result of atomic attraction during heating. Recrystallisation begins at approximately half of the absolute melting temperature of the material and results in a shrinkage and microstructural changes due to grain growth and phase transformation [43]. In compacted metal powders, cohesion takes place at the points of particle contact via the formation of necks, which subsequently transform into grain boundaries. Grain boundaries grow over time, and with infinite time the particles would diffuse into one, as depicted in Figure 12 A-D.

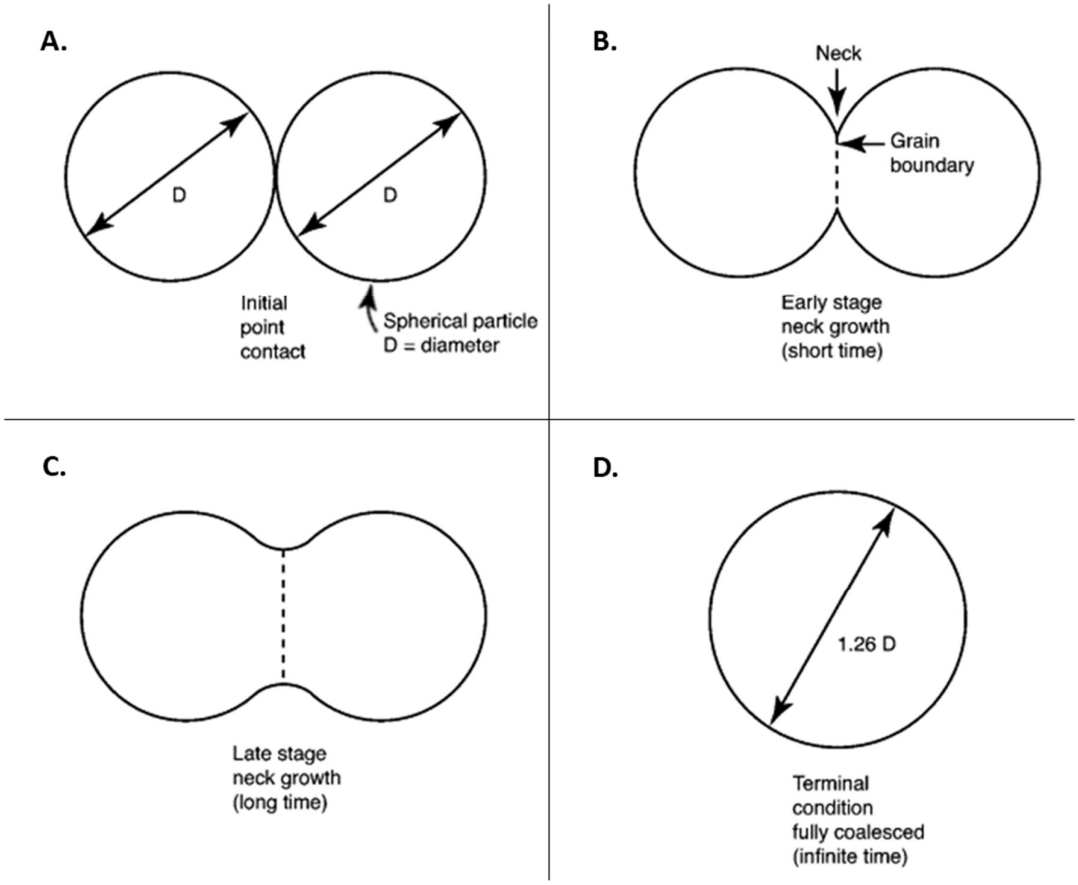

Figure 12: Stages of sintering, adapted from [44]

Sinter necks are driven by the elimination of surface energy, which is achieved by reducing the total surface area through atomic diffusion into the neck region. Surface oxides on the powder particles negatively affect the formation of sinter necks, so sintering atmospheres are controlled to prevent oxidisation and assist in the reduction of residual oxides from the powder production process. Sintering atmospheres include hydrogen or endogas (a gas rich in carbon monoxide and hydrogen) for oxide reduction, and nitrogen or dissociated ammonia for oxidation prevention. The rate of the sintering process is sensitive to temperature, with higher temperatures increasing the reaction rate. A typical industrial sintering furnace has three distinct zones; a pre-heat zone, hot zone and cooling zone. Parts are heated in the pre-heat zone at a set rate to allow for de-lubrication. Components are then fed into the hot-zone, where they are held at the required sintering temperature for sufficient time to achieve adequate particle bonding. Components are then passed into the cooling zone which controls the cooling rate to determine the final microstructure of the sample. A typical sintering time-temperature profile is illustrated in Figure 13.

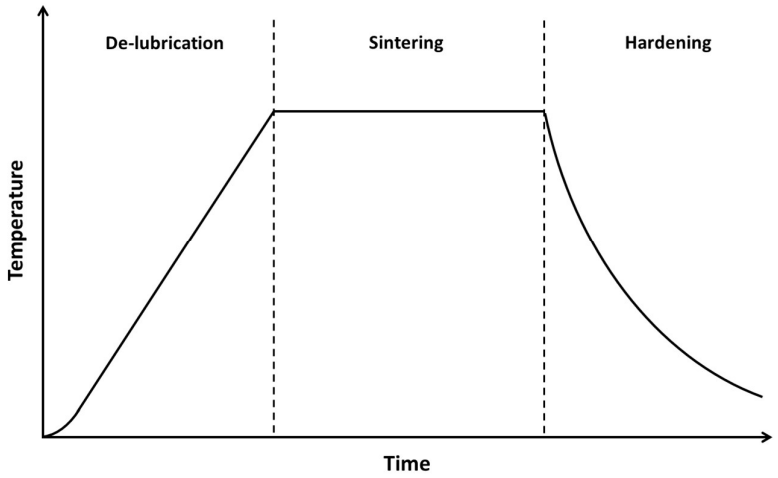

Figure 13: Typical sintering temperature profile over time, adapted from [36]

The production of iron and steel parts most commonly uses continuous furnaces due to their high throughput. These furnaces have wire mesh conveyor belts to transport the components through the furnace. Mesh belt furnaces can be used at temperatures up to 1150°C, with this upper limit being set by the heat resistance of the belt material [32]. Higher temperatures can be achieved with specialist furnaces, which have the advantage of more easily reducing oxides and forming more efficient sinter necks due to faster diffusion. As the degree of sintering is increased the materials properties tend to improve. Common properties of interest include mechanical strength, hardness, fatigue life, toughness, ductility, electrical conductivity, thermal conductivity, corrosion resistance, and particularly for iron powder, magnetic saturation. However, sintering time and temperature are both limited by the costs involved with designing and running the furnace hence a suitable compromise must be made.

2.3 Soft Magnetic Composites

2.3.1 Introduction

Soft magnetic composite (SMC) materials are an innovation from the powder metallurgy industry dating back over 100 years. Early SMCs include iron-resin composites for soft magnetic applications which were limited by their poor properties, extensive processing needs and lack of technological applications. These limitations were overcome with the advent of new raw materials and shaping technologies in the latter 20th century. Today, SMCs are being designed with the aim of replacing traditional steel laminations used in electrical motors [45] [46] [47] [48]. The manufacture of SMC components utilises traditional powder metallurgy production processes with a few modifications. The main differences are the need to apply the coating prior to compaction and that subsequent heat-treatment is at a reduced temperature to preserve this coating layer. The heat treatment temperature is determined by the coating material, but as it is lower than sintering temperatures the heat-treatment is referred to as curing or annealing.

Key performance data were collected for commercially available SMCs and laminated steels to provide a comparison with existing soft magnetic materials. Magnetic, electrical and mechanical properties are given in Table 1 and core loss data is given in Table 2.

Soft Magnetic Materials	Density (g/cm^3)	Induction @ 10 kA/m (T)	Max Perm.	Coercivity DC (A/m)	Resistivity (mΩcm)	TRS/Yield (MPa)
Somaloy 5P 700 HR **[49]**	7.50	1.57	600	120	70	60
Ancorlam **[14]**	7.45	1.6	417	302	8	81
EN 10106 M235-35A Laminated Steel **[16]**	7.60	1.76	610	35	0.059	460
EN 10106 M400-50A Laminated Steel **[16]**	7.70	1.79	1070	50	0.042	305

Table 1: Magnetic and mechanical properties of existing soft magnetic materials

Soft Magnetic Materials	Core Loss @ 1 T (W/kg)				
	50 Hz	100 Hz	400 Hz	1000 Hz	2500 Hz
Somaloy 5P 700 HR **[49]**	3.2	6.6	30	92	241 (@2kHz)
Ancorlam **[14] [50]**	6	13	59	170	< 700
EN 10106 M235-35A Laminated Steel **[16]**	0.92	2.31	16.9	71.5	349
EN 10106 M400-50A Laminated Steel **[16]**	1.46	3.73	32.2	152	800

Table 2: Core loss properties of existing soft magnetic materials

Commercial SMCs have a resistivity more than two orders of magnitude greater than that of laminated steels. Induction at 10 kA/m is slightly higher in laminated steels, however this is in part due to the increased density of the laminated steels in comparison to commercial SMCs. Furthermore, magnetic flux density decreases with depth from the surface of the laminated core due to the skin effect of the iron core material [9]. Therefore, for components with dimensions more than a few millimetres, laminated steels cannot operate at maximum flux density. Meanwhile, SMCs do not possess this limitation, exhibiting 3D isotropic magnetic properties throughout the entire volume of the material. Coercivity is higher in SMCs than in laminated steels, and consequently SMCs are currently only competitive at frequencies above 1000 Hz. To be able to compete at the target frequency range between 50 – 1000 Hz decreased coercivity is required. Therefore a new coating system is sought which can survive the necessary temperatures required for full stress relief of the compacted powder. Increased curing temperatures will also give the potential for greater strength and permeability, which are inferior in SMC materials in comparison to their laminated steel competitors.

It is important to note that particle size distrubtion has a large effect on the magnetic and mechanical properties of SMC materials [51] [52]. Whilst it appears from the data in Tables 1 and 2 that Ancorlam has a worse coating to Somaloy 5P 700 HR, Ancorlam has a smaller particle size than Somaloy which accounts for the inferior magnetic properties [14] [49]. Smaller particle sizes result in more grain boundaries, reduced densities and lower magnetic volume, which negatively impact magnetic properties as discussed previously in Section 2.1.5. Thus we cannot directly compare these two SMCs when assessing the quality of their coating systems.

2.3.2 Core Powder

The core powder of a soft magnetic composite material refers to the base material upon which the coating is applied. Core powder materials can be very broadly classified as either ferromagnetic and ferrimagnetic. The performance of soft magnetic materials is frequency dependent, so consideration must be given to the frequency range of the target application. Ferromagnetic materials are ideal at low frequencies (<2 kHz) due to their excellent magnetic saturation, but possess poor resistivity. Conversely, ferrimagnetic materials are ideal at high frequency (up to and in excess of 80 MHz) due to their high resistivity, but have reduced magnetic saturation due to the higher oxygen content [7]. Common ferrimagnetic materials include ferrites such as manganese-zinc ferrite and nickel-zinc ferrite. As this research project aims to create a SMC material suitable for use at low frequencies, the saturation magnetisation of ferrites is too low to be competitive as a core material at this frequency range. However, their excellent resistivity makes them a possible candidate for the coating material which will be discussed in Section 2.3.4.

Most core powder materials used in SMCs are ferromagnetic, the most common being pure iron and various iron alloys. Pure iron is the most prototypical soft magnetic material with high saturation magnetisation and very low production costs [7]. Interstitial impurities are added to iron for various reasons, for example the addition of carbon or hydrogen increases strength, whilst the addition of nitrogen or oxygen increases resistivity. However, the inclusion of small amounts of these interstitial impurities even as low as 0.1% drastically reduces magnetic properties. Conversely, the introduction of substitutional impurities including silicon, vanadium, copper and tin has a much smaller effect on the magnetisation, even in proportions up to 1%, and therefore can be added to improve resistivity and mechanical strength [53].

Various alloys of iron exist with better properties than pure iron. The addition of cobalt achieves the highest saturation magnetisation at room temperature of all known materials at 2.43 T for a 35%Co-65%Fe alloy [54]. A considerable increase in mechanical properties can be achieved with a small addition of vanadium or chrome to an iron-cobalt alloy, for example 49%Fe-49%Co-2%V, known as permundur [55]. A high maximum flux density allows for reduced size and weight of electrical cores, and therefore electrical machines with high power densities. However, iron-cobalt alloys are extremely expensive and hence are only economically viable in the aviation, aerospace and motorsport industries [56]. Iron-silicon alloys are widely used material in electrical machines with silicon contents of up to 6.5 wt%. The addition of silicon increases mechanical hardness and electrical resistivity at a cost of reduced magnetic saturation and permeability [53] [57]. Iron-nickel alloys have the highest magnetic permeability of all iron alloys due to the low magnetic coercivity. Iron-nickel alloys lie between iron-silicon and iron-cobalt in terms of cost, but are behind in terms of saturation magnetisation [58].

Recent research has demonstrated the potential of nanocrystalline and amorphous materials for use as core powders in SMCs [59] [60]. Nanocrystalline materials refer to single or multi-phase polycrystalline grains less than 100 nm in size [61]. The small grain size gives rise to a large number of grain boundaries resulting in very high electrical resistivity. However, increased magnetic pinning at these domain boundaries increases coercivity and reduces magnetic saturation [62] [63]. Nanocrystalline materials can be broadly categorised into three main alloys. Fe-Si-B-Nb-Cu alloys first developed by Yoshizawa et al. are known as a pioneer material of nanocrystalline soft magnetic materials and exist under the trade name of FINEMET® [63]. Fe-M-B-Cu alloys (M=Zr, Nb, Hf) developed by Kojima et al. are known under the trade name of NANOPERM® [64]. (Fe,Co)-M-B-Cu alloys (M=Nb, Hf, Zr) developed by Iwanabe et al. are designed for applications with higher induction but smaller permeability requirements and are known as under the trade name of HITPERM® [65].

Amorphous materials, often referred to as metallic glasses, possess very low core losses due to their thin foil structure [66]. They are produced by a cost effective melt spinning procedure, where the molten alloy is cooled rapidly, fixing the iron molecules in place and producing an amorphous structure [56]. This amorphous structure gives extremely high resistivity and after appropriate annealing to relieve stresses, high permeability and low coercivity can also be achieved [55]. However, magnetic flux density is typically lower than iron alloys and hence amorphous materials are more suited towards higher frequency applications where low core losses are required. Amorphous soft magnetic materials can be broadly classified as either cobalt or iron based, with the former having greater permeability and the latter possessing greater magnetic saturation.

Magnetic and electrical properties of typical core powder materials are provided in Table 3. A graphical representation of maximum permeability against saturation magnetisation was produced from the data and is presented in Figure 14.

Material	Typical Composition (wt%)	Saturation Magn. (T)	Max Perm.	Coercivity (A/m)	Resistivity (μΩm)
Iron **[67]**	Fe_{100}	2.16	3,000 – 50,000	10 – 100	0.1
Iron-Silicon **[62] [67] [68] [69]**	$Fe_{93.5-97}Si_{3-6.5}$	1.8 – 2.0	2,100 – 6,100	4 – 40	0.5 – 0.8
Iron-Nickel **[67] [69]**	$Fe_{50}Ni_{50}$	1.6	100,000	4	0.5 – 0.6
Iron-Cobalt (Permendur) **[67] [69]**	$Fe_{49}Co_{49}V_2$	2.35	2,000	30 – 100	0.4
Ferrites (Mn-Zn) **[70] [71]**	$(Mn, Zn)_1O_1 \cdot Fe_2O_3$	0.3 – 0.5	2,000 – 40,000	2 – 12	$1x10^5$ – $2x10^5$
Ferrites (Ni-Zn) **[70] [72] [73]**	$(Ni, Zn)_1O_1 \cdot Fe_2O_3$	0.2–0.4	300 – 3,000	15 – 65	$1x10^9$ – $2x10^9$
Amorphous (Fe-based) **[68] [74] [75] [76]**	$Fe_{76}Si_9B_{10}P_5$	1.5 – 1.8	4,000 – 12,000	1 - 5	1.2 – 1.4
Amorphous (Co-based) **[74] [75]**	$Co_{70.5}B_{15}Si_{10}Fe_{4.5}$	0.6 – 0.9	70,000 – 1,000,000	0.3 - 1	1.2 – 1.5
Nanocrystalline (FINEMET) **[63] [74] [75]**	$Fe_{73.5}Si_{13.5}B_9Nb_3Cu_1$	1.1 – 1.4	5,000 – 100,000	0.6 - 3	1.2
Nanocrystalline (NANOPERM) **[62] [74] [75] [77]**	$Fe_{84-91}M_7B_{2-9}Cu_{0-2}$	1.4 – 1.7	4,000 – 50,000	2 - 5	0.5 – 0.6
Nanocrystalline (HITPERM) **[75] [77] [78]**	$(Fe, Co)_{93-y}M_yB_6Cu_1$	1.5 – 1.9	1,000 – 10,000	20 – 200	–

Table 3: Properties of typical core powder materials

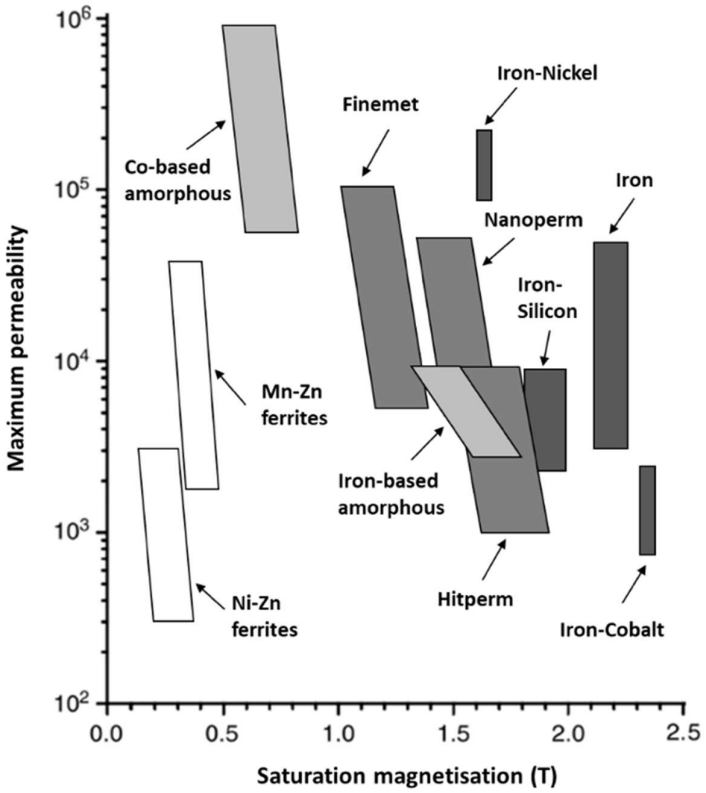

Figure 14: Maximum permeability and saturation magnetisation of typical core powder materials

Pure iron powder was selected for use in the experimental work of this thesis due to a combination of high magnetic saturation and low cost. Whilst there are alternative materials with lower core losses, this project aims to create a material which competes with laminations at low frequency (50 – 1000 Hz) and high maximum flux density is required to compete in this region. High resistivity offered by alternative core powders can be achieved with an effective coating system. Maintaining a consistent core powder allowed for direct comparisons between different coating systems.

2.3.3 Coating System

The primary purpose of the coating system is to reduce core losses by confining the eddy currents within each iron powder particle. In some cases, coatings may have a secondary purpose of increasing mechanical strength by acting as a "binder" material between the particles, fusing together during the annealing process [79]. Whilst the perfect coating does not exist due to conflicting properties, defining what constitutes one is useful for understanding their requirements. The ideal coating would possess high magnetic permeability, magnetic saturation, electrical resistivity, oxidation resistance and mechanical strength, whilst adhering well to the base material forming a thin uniform coating layer. The coated powder would be easily moulded and ejected from the die cavity without damage. The

coating system would also be thermally stable up to the annealing temperature of iron, which is in the region of 570-775°C [80]. This would allow for full stress relief of the compacted component, minimising coercivity and maximising magnetic permeability of the iron powder. Additionally, curing time can also control the stress-relief process of iron. The relief of residual stresses is a time-temperature related phenomenon, parametrically correlated by the Larson-Miller equation [81]:

$$\text{Thermal effect} = T\,(\log_{10} t + 20)\text{x}10^{-3} \qquad (2.7)$$

where *T* is Temperature in kelvin and *t* is time in hours. Therefore, a similar level of stress relief can be achieved by annealing at a lower temperature for a longer period. This is useful for SMCs as annealing temperature is limited by thermal resistance of the coating material. However, temperature rather than time is still the dominating factor [82]. Uozimi et al. found that the coercivity of iron based SMC components linearly decreases with increased annealing temperature from 300-600°C, but is near constant between 600-800°C [83]. This is in agreement with Oikonomou, who found that the majority of plastic strain stored in iron based SMCs was relaxed after curing at temperatures a7bove 600°C [84]. Thus, an ideal coating would be thermally stable to at least 600°C.

2.3.4 Coating Material

Coating materials can be classified as either organic or inorganic. The coating is designed to insulate the core powder, increasing resistivity of the bulk material and reducing core losses. However, the addition of a coating causes magnetic dilution, leading to a reduction in magnetic permeability and magnetic saturation. This trade-off can be mitigated through the use of a magnetic coating, but typical coating materials will nonetheless have a lower flux density than the core powder.

There are two main categories of organic coating material; thermoplastic and thermosetting polymers. Thermoplastic polymers do not form chemical bonds and soften upon heating. Whilst they are easily mouldable and compact well, it is difficult to form a thin uniform coating on the core powder as they are insoluble in most common solvents. Thermoset polymers on the other hand do form chemical bonds, providing good mechanical properties and resistance to both heat and chemicals. Common thermosetting polymers used as coating materials include such as epoxy resins, phenolic resins, acrylic powder, polyester powder and polyurethane powder [13] [85] [86] [87] [88].

Organic coatings allow for complete isolation of particles by infiltrating the ferrous powder structure and uniformly distributing insulation layers, creating an embedded matrix and resulting in high electrical resistivity. However they have poor thermal stability, for example epoxy resins break down at 300°C leaving large pores and metal-on-metal contact [8]. For an iron-resin composite using organic silicon epoxy resin coating, the optimal magnetic and mechanical properties occurred after curing at 200°C, above which the coating began to break down [86]. Organic coatings are non-magnetic, thus

their inclusion reduces the total available magnetic volume, decreasing permeability and magnetic saturation and increasing coercivity of the SMC. The deleterious effect of nonmagnetic regions are even more dominant than that of grain boundaries or dislocations, as these nonmagnetic regions act as internal demagnetising regions. Therefore it is of paramount importance to minimise the thickness of organic coating layers.

Inorganic coatings can be subdivided into several categories including phosphates, oxides and soft ferrites. Inorganic coatings allow for higher curing temperatures than organic coatings as they can typically withstand higher curing temperatures before degrading. Phosphates are one of the most common coating materials used for SMC materials [7] [30]. Phosphate coatings are typically produced by a conversion process, where the surface of the core powder is converted into a coating by a chemical or electro-chemical process. Phosphating treatments provide a coating of insoluble metal-phosphate crystals that adhere strongly to the base metal. Phosphate coatings have good thermal stability. For example iron phosphate coatings survive up to 500°C, above which the iron phosphate degrades into iron phosphide and iron oxides due to mutual diffusion of iron, phosphate and oxygen [89] [90]. Manganese phosphate has a higher melting temperature of 600°C, allowing slightly increased curing temperatures in comparison to traditional phosphate coatings which degrade at 450°C [91]. Applying a phosphate conversion coating to FeSiAl powder forms an aluminium phosphate coating as the aluminium dominates the iron in the reaction to form phosphate. Upon annealing between 600-700°C, aluminium phosphate partially decomposes into alumina (Al_2O_3) and phosphorous pentoxide (P_2O_5) which both possess high resistivity and density, decreasing overall core loss and enhancing magnetic properties [90].

Oxides are a useful coating material due to their high electrical resistivity and thermal stability. Aluminium oxide (alumina) can withstand very high curing temperatures up to 900°C without significant degradation, but requires extremely high compaction pressures (up to 3000 MPa) or additional lubricants which dilute magnetic volume [92] However, whilst the alumina coating remains intact, at high temperatures iron cations diffuse through the alumina coating and oxidise the iron particles, thus the alumina coating merely slows down the oxidation process [93]. Yaghtin et al. found overall core loss in iron based SMCs with alumina coating increases after annealing at 600°C in comparison to annealing at 400°C, despite no considerable degradation of the alumina insulation layer [94].

Silicon oxide (silica) coatings are another promising candidate coating material with much research interest in recent years [88] [95] [96] [97] [98]. Silica coatings are thermally stable up to 600°C allowing for considerable stress relief and low coercivity, combined with high electrical resistivity to give low overall core losses. Yang et al. reported on iron based SMCs with silica coating possessing a core loss

of 3.5 W/kg (@50 Hz, 1 T), considerably lower than that of commercially available phosphate coated SMCs [97]. Magnesium oxide is another oxide coating material with very good thermal stability, remaining fully intact after annealing at 600°C, retaining higher resistivity and outperforming the magnetic properties of a phosphate-coated control sample [29] [83].

Soft ferrites are a promising candidate material and have been the centre of increasing research work [99] [100] [101] [102] [103] [104] [105]. Soft ferrites have the distinct advantage of being ferrimagnetic, thus retaining some magnetic volume of the bulk material when used as a coating material. Furthermore, they have excellent resistivity and high thermal stability up to 900°C [100] [103] [104]. Lauda et al. developed a MnZn-ferrite coating on FeSi core powder which produced significantly reduced eddy currents after curing at 780°C [101]. Gheisari et al. and Peng et al. reported good magnetic properties after curing at 800 - 900°C for iron powder coated with NiZn-ferrite [100] [104]. However, Wu et al. found that MnZn-ferrite coated on iron powder decomposes to non-magnetic FeO and MnO after annealing above 400°C, reducing permeability and resistivity [105].

Further research is required in this area to fully understand the mechanisms behind the curing process. Whilst soft ferrites have great potential, there are various challenges to overcome before an effective coating system can be produced. Ferrites are brittle and do not deform easily which can lead to shearing during the compaction process if the ferrite is not well bonded to the core powder [106]. Ferrites also have poor compressibility leading to large porosities and low densities in the final compact [101]. Ferrites are often synthesised as nanoparticles which tend to agglomerate and hence it is difficult to form a uniform coating layer on the substrate material [107]. Phase transitions when heat treating ferrites are also important as they can both help and hinder the magnetic properties. For example, Fe_3O_4 partially converts into Υ-Fe_2O_3 with increased oxidation temperature from 150 °C and 250 °C, leading to an increase in effective permeability and lower overall core losses [107]. However, further heating to 570°C results in the reduction of Fe_3O_4 to FeO, reducing magnetic volume, increasing coercivity and reducing permeability [107] [108]. If these various challenges can be overcome, soft ferrites are indeed a very promising coating material.

Hybrid coatings have the potential to combine favourable properties from both organic and inorganic coating materials and are gaining increasing traction in the literature. As a recent example, in 2020 Evangelista et al. developed a hybrid zinc oxide and barium oxide coating, where the combination of the two materials had a synergistic effect, resulting in superior properties to that of either coating material used alone [109]. Other examples include Taghvaei et al. who developed a hybrid phosphate-polyepoxy coating, with the polyepoxy acting as a protective layer on top of the brittle phosphate, reducing cracking during compaction and increasing resistivity of the compacted samples [89]. Uozimi et al. developed an improved magnesium oxide coating with the addition of silicon resin and a glass

binder which increased resistivity at all annealing temperatures up to and including 800°C, leading to reduced core losses, below that of laminated steel and commercial SMCs with inorganic coatings [83].

2.3.5 Coating Processes

The design of an effective coating system requires the combination of a suitable coating material and application method. An effective coating method should form a thin, uniform layer that is strongly adhered to the surface of the core powder. Broadly speaking, coating processes can be classified as either dry mixing methods or wet chemistry techniques. Recently dry coating methods have been increasingly used to produce SMCs including ball milling [31] [92] [110] and acoustic mixing [39]. These methods rely on Van der Walls interactions and static forces between core powder and coating particles. Dry coating processes are very simple, and require minimal additions of lubricant or binder, reducing the levels of impurities in the final SMC. However, the core powder and coating are not chemically bonded which can give rise to difficulties upon maintaining a uniform coating layer after the compaction process.

Wet chemical methods such as immersion and spray-coating often give better adhesion to the surface of the core powder, but have uncontrollable phase transformations and layer thicknesses leading to agglomerates of the coating material. This makes it difficult to achieve a thin, uniform layer on the core material, reducing the surface coverage and effectiveness of the coating. More coating material is required to achieve the necessary surface coverage, which decreases the magnetic volume of the final composite. Recent research on coating ferromagnetic powder has focused on more novel coating methods such as surface oxidation [79] [107], microwave treatment [104], sol-gel method [94] [105] and the micro-emulsion method [111]. The final coating must be very thin - in the order of nanometres - so the coating procedure must reflect this. Whilst these methods can yield encouraging final results, they often involve time consuming and potentially hazardous chemical processes.

One particularly common coating procedure in the SMC industry is the phosphate conversion coating, used in commercially available powders [112]. Conversion coatings are coatings for metals where the part surface is converted into the coating with a chemical or electro-chemical process. Phosphating treatments provide a coating of insoluble metal-phosphate crystals that adhere strongly to the base metal. Generally, phosphating solutions are dilute phosphoric acid based solutions containing one or more alkali metal/heavy metal ions, which essentially contain free phosphoric acid and primary phosphates of the metal ions contained in the bath. The addition of an accelerator can be included to increase the efficiency of the coating process [113].

2.3.6 Compaction and Curing of SMCs

The compaction process of SMCs follows the same fundamental principles of traditional powder metallurgy with the additional challenge of preserving the coating material. Brittle coating materials will shear and break away from the base powder, creating metal-on-metal contact between core powder particles and undermining the purpose of the coating. Softer materials compact and deform more easily than harder materials, which in the case of most ferrous-based SMCs means the core powder deforms under the coating material. To mitigate these effects, warm compaction and lubricants can be used to improve packing behaviour.

Small amounts of cold working imparted during the compaction process induce dislocations and increase micro-strain, which in turn increase coercivity resulting in higher hysteresis losses. The curing process primarily serves to reduce these post-compaction stresses, whilst also releasing lubricants from the component and increasing mechanical strength [114]. In powders with fully encapsulating coatings, curing is also necessary to preserve the coating layer so that no metal-on-metal contact points are found, thus minimising eddy currents [7] [8]. SMCs cannot be sintered as the high temperatures degrade the coating material and form metallurgical bonds between core powder particles [115]. Therefore, soft magnetic composites are cured at a reduced temperature ideally at the annealing temperature of iron (between 570°C and 775°C) [32] [31] [80] [82]. Full recovery of the stresses does not take place until temperatures reach above 1000°C [116], however the majority of plastic strain is recovered and coercivity is minimised after annealing above 600°C [83] [84] . The optimal curing temperature is therefore chosen on a balance between maximising stress relief of the core powder (thus minimising coercivity) and minimising the deterioration of the electrically insulating coating (thus maintaining resistivity).

A secondary outcome of the curing process is the release of the lubricant material, which can influence the properties of the final component. Lubricant burn-off occurs in the region of 300°C, for example stearates escape between 250°C and 400°C in iron powder parts [117]. If a slow enough temperature ramp is used, full lubricant burn-off is possible depending on the type of lubricant used [118]. The maximum ramp rate is dependent on component size and density, but typically a ramp rate of <15 °C/minute is suitable for most lubricants. For best results with larger samples or high densities, the samples can be held at an intermediate lubricant burn-off temperature to allow for lubricant release before continuing to the ultimate curing temperature.

Another challenge in heat treating ferrous based SMCs is the oxidation process. The curing process creates oxides contacts between particles which greatly increase mechanical strength, a process known as thermal oxidation bonding. As the resistivity of the oxide contacts is significantly lower than

that of the lubricant or air gaps that filled the particle interstices in the green state, the overall resistivity of the sample reduces by around an order of magnitude [119]. The rate of the oxidation process is dependent on atmosphere and temperature. In an air atmosphere, oxygen is readily available for the oxidation reaction, thus significant inter-particle oxide bonds are formed, resulting in low resistivity and high mechanical strength. In an inert atmosphere, for example nitrogen, it may be assumed there would be no thermal oxidation bonding due to a lack of oxygen. However, the required oxygen partial pressure is low enough that the residual oxygen in the nitrogen gas even at purity levels of 4N (99.99% purity nitrogen) is sufficient to cause oxidation bonding. Furthermore, oxygen is produced during lubricant burn-off, so even in a truly inert atmosphere some oxidation bonding will still occur. Thus curing in nitrogen merely inhibits oxidation bonding, resulting in higher resistivity but lower mechanical strength than curing in air.

In a hydrogen atmosphere, one might predict higher resistivity as the reducing atmosphere prevents the formation of oxides on particle surfaces. However, resistivity is actually lower than after curing in air or nitrogen due to the oxide reduction allowing for the formation of metallic contacts with lower resistivity than oxide bonds [120]. As these metallic bonds are weaker than oxide bonds, curing in hydrogen at atmospheric pressure also results in lower mechanical strength than curing in air or nitrogen. To maximise mechanical strength steam treatment is used [121]. The steam reacts with the iron to form magnetite (Fe_3O_4). Steam treatment is only recommended for applications where superior mechanical performance is sought over magnetic performance as the resistivity of the material decreases significantly. Therefore, powders designed for magnetic performance are heat-treated in inert atmospheres such as nitrogen or argon to control oxide formation.

An innovative compaction and curing process known as “double press – double cure (2P2C)” was developed by Narasimhan et al. for use with SMC materials [122]. This process uses warm compaction in a heated die together with multiple compaction and heat treatment steps to achieve ultra-high densities whilst maintaining the integrity of the coating material. This process is effective in minimising core loss, but is not economically viable due to the expense and time of additional processing steps.

3 Experimental Methods

In this chapter the experimental methods employed for material development and characterisation are outlined. The experimental work can be broadly divided into two distinct sections:

1. Sample preparation and processing
2. Measurement and analysis techniques

Sample preparation and processing includes synthesis of coating materials, coating techniques, compaction and heat treatment and will be covered in Section 3.1. Measurement and analysis techniques cover the characterisation of magnetic, electrical, mechanical, physical and structural properties and will be covered in Section 3.2.

Pure iron was selected for use as the core powder material in all experimental work as justified in Section 2.3.2. Maintaining a single core powder material allowed for direct comparisons between the different coating systems that were developed.

3.1 Sample Preparation and Processing

3.1.1 Core Powder

Commercially available Ancorsteel 1000C, provided by GKN Hoeganaes Corporation (Cinnaminson, New Jersey) was used as the core powder for all experimental work into the development of new coating systems. Ancorsteel 1000C - herein referred to as "A1000C" - is a high purity iron powder for use in electromagnetic applications, possessing low oxygen and nitrogen levels. A1000C is produced by atomising molten steel into irregular, homogeneous particles which are then annealed to produce a uniform steel powder. Irregular particles were selected due to their high green strength achieved by mechanical interlocking. The elemental composition of standard A1000C is presented in Table 4 and the size distribution is presented in Table 5 [123].

Element	C	O	N	S	P	Si	Mn	Cr	Cu	Ni
wt%	<0.01	0.07	0.001	0.007	0.004	<0.01	0.07	0.02	0.03	0.04

Table 4: A1000C elemental composition [123]

Size (micrometres)	>250	150 - 250	45 - 150	<45
U.S Standard Mesh (wires per inch)	<60	60-100	100-325	>325
Percentage Weight (%)	Trace	17	70	13

Table 5: A1000C paticle size distribution [123]

3.1.2 Benchmark Materials

This research utilises Ancorlam as the benchmark material for measuring the performance of commercially available SMCs. Ancorlam is the current high-performance powder produced by GKN Hoeganaes Corporation for soft magnetic applications. Ancorlam consists of A1000C powder with a specialised coating system designed to minimise eddy current and hysteresis losses over a range of frequencies from 50 – 1000 Hz. The exact composition and coating process is proprietary information, but the resulting coating consists primarily of iron and zinc phosphates [124].

Somaloy 700HR 5P, a competitor product to Ancorlam was used for further comparison purposes as reported in Chapter 4. The Somaloy 5P series of magnetic powders are produced by Höganäs AB and utilise a similar phosphate based coating system to Ancorlam. Somaloy 700HR 5P is designed for high density applications and has a coarse average particle size of 250 µm [125].

3.1.3 Coating and Binder Materials

The coating materials selected for use in the experimental work included manganese ferrite, zinc oxide nanopowder, magnesium oxide nanopowder and aluminum oxide nanopowder**.** Manganese ferrite M035 was provided by Powdertech International, USA. Zinc oxide nanopowder, magnesium oxide nanopowder and aluminium oxde nanopowder were purchased from Sigma-Aldrich. Material properties for each of these coating materials are presented in Table 6.

	A1000C base iron powder	Manganese ferrite	Zinc oxide nanopowder	Magnesium oxide nanopowder	Aluminium oxide nanopowder
Molecular formula	Fe	$MnFe_2O_4$	ZnO	MgO	Al_2O_3
Average Particle Size (nm)	> 75,000	1000	< 100	< 50	< 50
Density (g/cm^3)	7.87	5.20	5.68	3.58	3.95
Melting temperature (°C)	> 1300	> 1300	1975	2852	2040
Resistivity (Ωm)	$1x10^{-8}$	$1x10^{6}$	-	$1x10^{12}$	$1x10^{12}$
Saturation Magnetisation (T)	2.2	0.5	0	0	0
Specific Surface Area (m^2/g)	-	4.9	10 - 25	50 – 80	> 40

Table 6: Properties of ferrite and metal oxide coating materials [123] [126] [127] [128] [129] [130].

A binder material was used in some experimental methods to aid the coating process. Sodium silicate, otherwise known as liquid glass, was used as a binder material within which other coating materials were dispersed. Two liquid glasses were selected for experimental trials. A base sodium silicate technical solution was purchased from VWR International, and a second sodium silicate R2447 was provided by Diatom, Brazil. The relevant material properties for the two liquid glasses used in the experimental work are given in Table 7.

	VWR Sodium silicate solution, technical	Diatom R2447 sodium silicate solution
Density (g/cc)	1.34	1.47 – 1.51
Silica content (wt%)	25.6 – 27.6	29.0 – 31.5
Sodium oxide content (wt%)	7.5 – 8.5	11.7 – 13.2
Total solids (wt%)	33.1 – 36.1	40.7 – 44.7
Silica / sodium oxide ratio	> 3	2.35 – 2.50
pH range	neutral	alkaline

Table 7: Key data for sodium silcates [131] [132]

Silane coupling agents are a second class of binder material and a potential coating material themselves. Silane coupling agents can be used as an intermediate binder between two materials, or as a surface treatment per se. All silanes used in the experimental work were purchased from Gelest Inc, Morrisville and are listed alongside some key details in Table 8.

Full Name	Description	Gelest Code	Organic Groups	Inorganic Groups
3-AminoPropylTri -EthoxySilane (APTES)	Amino Monopodal	SIA0610.0	1x amino	tri-ethoxy
(3-GlycidoxyPropyl) -TriMethoxySilane	Glycidoxy Monopodal	SIG5840.0	1x glycidoxy	tri-methoxy
1,2-Bis(TriEthoxy -Silyl)Ethane	Non-Fuctional Dipodal	SIB 1817.0	n/a	2x (tri-methoxy)
BIS(3-TriMethoxy -SilylPropyl)Amine	Mono-Amine Dipodal	SIB1833.0	1x amine	2x (tri-methoxy)
N,N'-Bis[3-(TriMethoxySilyl) -Propyl] EthyleneDiamine	Di-amine Dipodal	SIB1834.0	2x amine	2x (tri-methoxy)
Bis[3-(TriEthoxySilyl) -Propyl]DiSulphide, 90%	Di-sulphide Dipodal	SIB1824.6	2x sulphide	2x (tri-ethoxy)
Enhanced APTES	*Mix of silanes*	SIA0610.E1	amine-based	ethoxy-based
Activated APTES	*Mix of silanes*	SIA0610.A1	amine-based	ethoxy-based

Table 8: Key data for silane coupling agents [133] [134] [135] [136] [137] [138] [139] [140]

3.1.4 Coating and Mixing Processes

The experimental work in this thesis focuses on wet chemical coating processes as opposed to dry mixing methods in order to achieve better surface coverage. A1000C was used in the as-received state in standard composition. Detailed coating procedures are set out in the experimental procedure section of each relevant experimental chapter. Nanoparticle coating materials were deagglomerated where necessary by ultrasonic dispersion using a Shesto SHE-UT8031-EUK 3 litre ultrasonic bath rated to 100 W.

Coated powders were admixed with organic lubricants prior to compaction as a method of reducing inter-particle and particle-to-die-wall friction [79]. Conventional powder metallurgy lubricants include fatty acid based waxes such as ethylene bis-stearamide (EBS) or metallic stearates such as zinc stearate (ZnSt) [141]. The lubricant used in this research is Kenolube, a commercially available lubricant which is a specially designed blend of EBS and ZnSt. The standard amount of lubricant used for samples in this research was 0.4 wt% of the coated powder, as per recommendation of the powder manufacturer [14]. As with the use of a consistent core powder, maintaining a constant amount and type of lubricant addition minimises variables, ensuring an equal comparison between each coating system developed.

Lubricants are mixed into the powder using a Turbula® T2F shaker-mixer, pictured in Figure 15. The required contents are placed in a sample jar which is rotated at 30 rpm for 15 minutes. The powder is then stored in a sealed and dry environment ready for compaction.

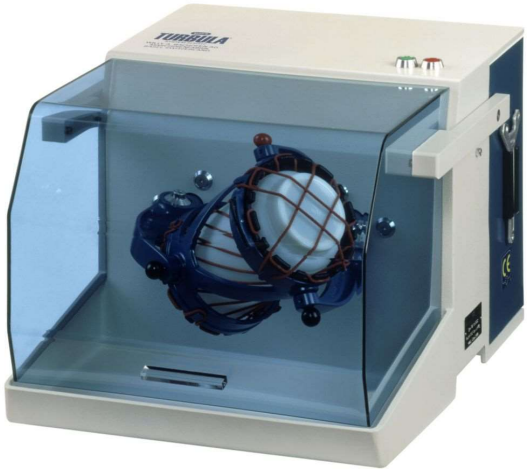

Figure 15: Turbula® T2F shaker-mixer [142]

3.1.5 Compaction Processes

Uniaxial die compaction was used for the majority of samples produced for this thesis. Ready-to-press powder mixes were compacted using a Sealey YK759F hydraulic press. Bar samples were pressed using a die cavity of nominal dimensions 30 mm x 12 mm and a target thickness of 6 mm. These dimensions were selected in accordance with ISO 3995 [143] and ISO 3325 [144] for the determination of transverse rupture strength and ASTM A712 [145] for the measurement of electrical resistivity. Toroidal samples were pressed using a die cavity of 36 mm outer diameter, 22 mm inner diameter and target thickness of 6 mm. These dimensions were selected in-line with Hoeganaes Corporation test data and in accordance with ASTM A927 for the measurement of AC magnetic properties [146]. This specific geometry allows for symmetrical winding of copper wire on the toroid sample with sufficient turns to produce an appropriate flow of applied current through the sample. Compaction pressure varied from 550 - 830 MPa based on the target density of the indiviudal sample. A pre-load of 20% of the final load was applied to give the sample its initial shape before the full load was applied.

An EPSI cold isostatic press (CIP) was used to compact samples without lubricant. Powder samples were compacted in custom made rubber dies up to the maximum rated pressure of 600 MPa. The dimensions of the rubber dies were calculated to produce bar samples of approximately 30 mm x 12 mm x 6 mm in order to perform TRS and resistivity testing in line with the samples produced by traditional uniaxial pressing.

3.1.6 Heat Treatment Processes

Samples were heat treated in a Lenton LTF 1200°C tube furnace as illustrated in Figure 16. The furnace atmosphere can be controlled by a flow of gas over the samples during the heat treatment process. Test specimens were cured in a range of conditions suited to the individual studies, including the variation of curing time, temperature and atmosphere. The standard heat treatment procedure involved curing at a temperature of 450°C for 1 hour with a flow of nitrogen gas with 4N purity (99.99%).

Samples were added to the centre of the quartz tube, prior to flooding the tube with nitrogen at 0.5 L/min for 15 minutes to fully replace the air (80 mm internal diameter, 1250 mm length = 6.28 litres). The ramp rate was set to 15°C / minute to allow for sufficient release of lubricants and binders with a constant flow rate of 0.1L/min of nitrogen gas. The mass, resistivity and density of each sample were measured before and after curing to measure differences during the heat treatment process. A Lenton horizontal split tube vacuum furnace rated to 1000°C and a minimum pressure of 0.1 Pa or $1x10^{-6}$ atm was used to investigate the effects of curing in an atmosphere with reduced oxygen.

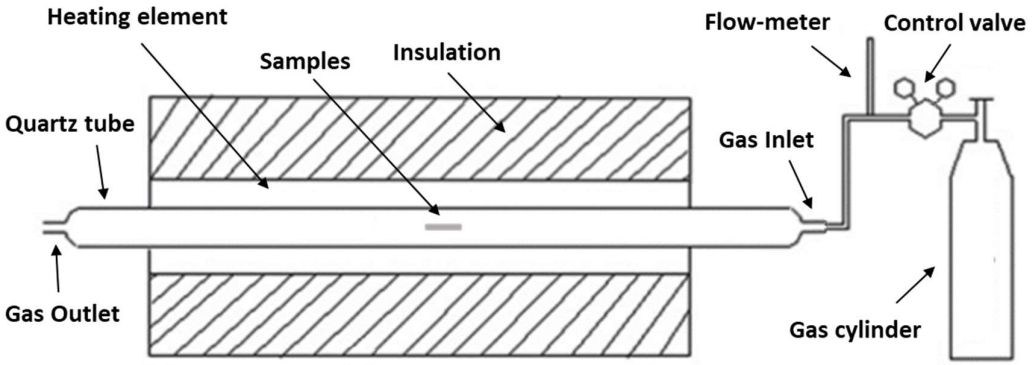

Figure 16: Schematic of tube furnace

3.2 Measurement and Analysis Techniques

Powder properties were analysed at each step of the production process, from loose iron powder, to compacts in the green state, through to final heat treated samples. Observation of the microstructure, morphology and chemical composition of the powder throughout the production process allowed for a greater understanding of the state of the coating and the mechanics of the heat treatment process. Samples were tested for their magnetic, electrical and mechanical properties to quantify their performance characteristics both in the green and cured states.

3.2.1 Microstructural Analysis and Chemical Composition

SEM & EDX

Scanning Electron Microscopy was used to analyse the microstructure of the core powder and coating material. A Scanning Electron Microscope (SEM) produces an image by scanning the surface of a sample with a focused beam of electrons fired from an electron gun. The SEM operates under a vacuum to ensure the fired electrons reach the sample and do not collide with gas molecules in the air. As the electrons interact with the atoms in the sample, electron and X-ray signals are emitted back into the detector.

The emission of secondary electrons is used to gather topographical information as they have low energies of less than 50 eV and consequently can only escape from the surface of the sample. Back scattered electrons are used to give information on the elemental composition as they have higher energies above 50 eV (but less than the incident beam voltage) and emerge from deeper in the sample. The penetration depth of the fired electrons depends on the atomic number of the materials under investigation and the acceleration voltage of the electron beam. Elements with a higher atomic number have smaller penetration depths and back scatter electrons more strongly, producing brighter regions on the electron image. The SEM produces a topographical image of the sample surface with regions of differing brightness to show contrast between different chemical compositions in the sample.

Energy dispersive X-ray spectroscopy (EDX) was used alongside the SEM to analyse the chemical composition of the core powder and coating materials. The EDX detects the X-rays emitted from the sample stimulated by the electron gun. The X-ray is converted to a voltage signal by the detector and sent to a pulse processor to measure the signals. These signals are then sent to an analyser for data display and analysis. The EDX works on the fundamental principle that each element has a unique atomic structure giving a unique set of peaks on the electromagnetic emissions spectrum. The EDX identifies the chemical elements present in the sample and their relative abundance to produce an elemental composition map.

A Zeiss EVO series Scanning Electron Microscope (SEM) equipped with an Oxford Instruments INCA x-act silicon drift detector was used for gathering images of the samples in this thesis. Compacted powder samples were mounted, polished and etched for examination under the SEM.

TGA

Thermogravimetric analysis (TGA) was used to identify a number of physical and chemical phenomena including phase transitions, absorption, desorption, thermal decomposition and solid-gas reactions. TGA allows the mass of a sample to be continually monitored as the temperature is varied over time. The TGA consists of a precision balance with a crucible holding the sample, located inside a furnace with programmable temperature control. A gas inlet control valve allows for a controlled atmosphere and flow rate into the analyser.

Thermogravimetric analysis (TGA) was performed using a Setaram Instrumentation LABSYS Evo STA. Both sections of compacted bar samples and loose powder samples were analysed in the TGA. The temperature profile and atmosphere used in the standard curing process in the tube furnace was simulated. As samples were heated, the de-lubrication and subsequent oxidation processes were identified at the respective temperatures, and their effect on the overall mass of the sample was able to be quantified.

3.2.2 Magnetic Testing

Toroid Measurements

Toroidal samples were used to characterise the AC magnetic performance of the powder compacts. The toroid samples were wrapped with a primary supply coil on top of a secondary pick up coil as depicted in Figure 17.

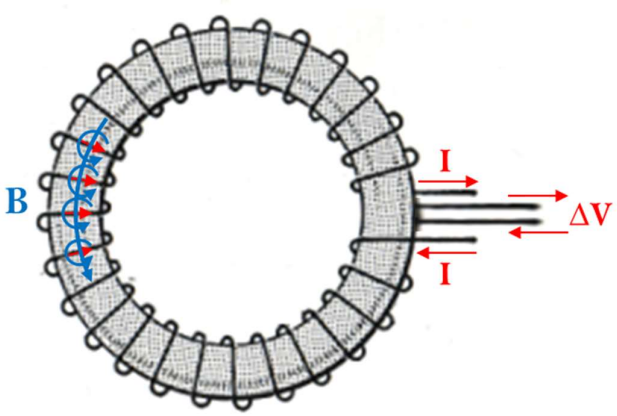

Figure 17: Schematic diagram of toroidal test specimen

A known positive current was applied to the sample through the primary coil. The flow of electric charge produces a magnetic response in the material known as the applied field, ***H***. This magnetic response results in a voltage difference observed across the secondary coil, which is measured by an oscilloscope and used to calculate the resultant field, ***B***. The full hysteresis loop can be obtained by

cycling the applied current up to the point of magnetic saturation, down to negative saturation and returning to zero. Toroid samples were wrapped with copper wire of diameter 0.56 mm with 100 turns on the primary coil and 40 turns on the secondary coil. Samples were measured in AC conditions at an induction level of 1 T with frequency ranging from 50 Hz to 1000 Hz in accordance with ASTM A927 [146].

In the absence of a vibrating sample magnetometer (VSM) or suitable DC power supply to measure DC magnetisation in accordance with ASTM A773, the permeability can be characterised by measuring the applied field, ***H*** required to produce an induction of 1 T at very low AC frequency. The greater the permeability, the smaller the required H-field to produce an induction of 1 T. By measuring the difference in required H-field between samples, the permeabilities of different samples can be compared to one another.

3.2.3 Electrical Testing

The four point probe method was used to measure the electrical resistivity of the powder compacts as depicted in Figure 18. A standard rig was constructed with current supplied by a TTI CPX400A power supply unit, and voltage measured using a Keithley 2110 digital multimeter. A constant current of 1 A was applied across each sample, and voltage probes were fixed into the lid at a distance of 1 cm apart. Measurements were taken for both the top and bottom faces of each sample and an average calculated. Samples were measured both in the green state and in the cured state. Resistivity, ρ is calculated using equation *3.1*:

$$\rho = V \cdot A \,/\, I \cdot l \qquad (3.1)$$

where *V* is voltage measured between the two voltage pins, *A* is the cross sectional area of the sample, *I* is the current applied through the sample and *l* is the length between the two voltage pins.

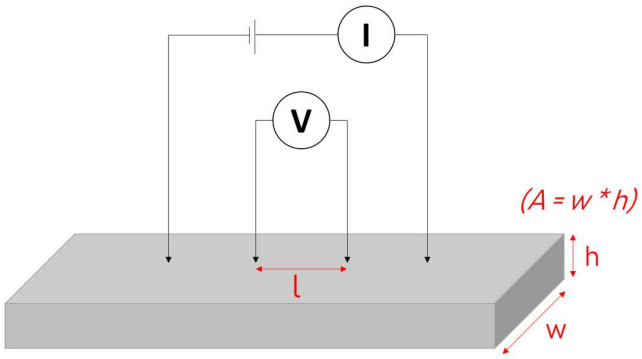

Figure 18: Schematic of four point probe method

3.2.4 Mechanical & Physical Testing

TRS

The three point bend test was used to measure the Transverse Rupture Strength (TRS) as illustrated in Figure 19. This is the standard method of assessing the strength of green compacts and sintered power metals. Bar samples were placed on 3 mm diameter supports at a span length of 25 mm in accordance with ISO 3995 [143] for the measurement of green strength and ISO 3325 [144] for the measurement of sintered materials. It is noted that the SMC materials were not sintered, but in the absence of an ISO standard for cured powder compacts the testing was carried out in best compliance with both standards. The load was applied to the centre of the sample by an Instron 5500R series tensometer. A 10 kN load cell was used to measure the maximum force exerted on the sample before rupture. TRS was then calculated from the maximum force exerted using equation *3*.2:

$$TRS = \frac{3FL}{2bd^2} \qquad (3.2)$$

where; *F* is the maximum force at the failure point, *L* is the span length, *b* is the sample width and *d* is the sample depth or height

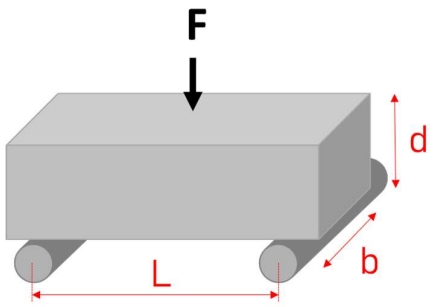

Figure 19: Schematic of three point bend test

Density Measurements

Density was calculated by measuring the sample dimensions using a micrometer and weighing on electronic scales. The density was simply calculated from the weight in grams divided by the volume in cubic centimeters. Measurements were taken both before and after heat treatment to measure changes in density as a result of the curing process.

4 Understanding Strengthening Mechanisms in SMCs

4.1 Introduction

In this chapter the heat treatment process of current SMCs is investigated in order to gain a thorough understanding the strengthening mechanisms involved. There exists a lack of clarify in the literature regarding what occurs during the curing process and how this differs from sintering, where the particles bind together by atomic diffusion. Due to the coating material, curing of SMCs has to occur below the sintering temperature and consequently involves a different mechanism.

It is reported in the literature that the magnetic properties of SMCs utilising various inorganic coating materials including phosphate, oxides and ferrites deteriorate if cured above 450 - 500°C [90] [105] [119] [120] [147] [148]. This rather narrow temperature range above which magnetic properties diminish is the same for many inorganic coatings studied, despite the thermal stability of the materials suggesting some may survive to higher temperatures.

For example, alumina has a very high melting point and as a coating material is thermally stable to over 900°C [92]. However, whilst the coating remains intact, at these high temperatures iron cations diffuse through the alumina layer and oxidise the iron particles, thus the coating merely slows down the degradation process [93]. Yaghtin et al. showed that overall core loss in an iron based SMC with alumina coating is greater after annealing at 600°C in comparison to annealing at 400°C, despite no considerable degradation of the alumina insulation layer [94]. Yi et al. found that NiZn-ferrite coated iron powder exhibited optimal magnetic performance after curing at 450°C, with properties degrading after curing at temperatures above this, despite the thermal stability of NiZn-ferrite exceeding these temperatures [148]. Wu et al. found that the magnetic properties of MnZn-ferrite coated iron powder degrade after curing above 400°C due to oxidation of the iron around 450°C [105]. Ouda et al. recently published a paper on the accelerated degradation of iron phosphate due to the presence of metallic iron by ferrothermal reduction, providing another plausible explanation for the relatively low thermal stability of phosphate coatings [149]. Finally, Oikonomou et al. showed that iron phosphate degrades at a temperature of 550°C due to diffusion of iron through the coating layer whilst curing in an inert atmosphere [150].

It is clear from the above literature examples that the magnetic properties of SMCs with inorganic coating materials all degrade in a relatively narrow temperature range. This degradation is due to various heat treatment mechanisms, including the diffusion of iron through the coating to form an oxide layer and ferrothermal reduction.

The formation of an oxide layer on the surface of the iron powder creates oxide contacts between particles which increase mechanical strength, in a process known as thermal oxidation bonding. As the resistivity of the oxide contacts is significantly lower than that of the lubricant or air gaps that filled the particle interstices in the green state, the overall resistivity of the sample reduces by around an order of magnitude [119]. The phenomenon of thermal oxidation bonding has been observed and reported in the literature by Gelinas et al. and Bidulsky et al. [151] [152] and is discussed in greater detail in Section 2.3.6.

In this chapter, the heat treatment mechanisms of SMCs and their practical implications are investigated. The experimental work focuses on Ancorlam, the current high-performance powder produced by Hoeganaes for soft magnetic applications.

4.2 Drop in Strength of Ancorlam at High Density

This section of experimental work investigates the drop in mechanical strength of Ancorlam powder at high density (refer Figure 20). Three possible hypotheses are discussed in this chapter; coating pull-off, over-pressing, and ineffective thermal oxidation bonding.

In SMCs utilising a binder material, the coating contributes to the strength of the bulk material, as is the case with liquid glass based coatings [Chapter 5]. At very high compaction pressures, the coating can shear and become detached from the core powder, adversely affecting the strength of the bulk composite material. To test whether this is the case for Ancorlam, the mechanical strength of coated iron powder (Ancorlam) and uncoated iron powder (A1000C) was measured over a range of densities from 6.0 – 7.4 g/cm^3. If the strength drops off at high density in the coated powder, but not in the uncoated powder, this suggests that the drop off in strength may be attributed to coating pull-off.

The hypothesis of over-pressing assumes that the extreme compaction pressures up to 830 MPa required to achieve the highest densities induce cracks into the samples which are detrimental to mechanical strength. To investigate whether this is true, the strength of compacted Ancorlam samples in the green state were compared to those after curing over a range of densities. If the drop in strength at high density is due to micro-cracking, then the strength should fall off in the green (non-heat treated) samples in the same manner as that of the cured samples.

The hypothesis of insufficient thermal oxidation bonding assumes that the lack in strength at high density is due to ineffective curing. The thermal oxidation bonding process relies on the formation of oxides on the surface of the iron powder which act as a binder between the individual particles. The magnitude of thermal oxidation bonding can be estimated by measuring the change in mass during the curing process. The gain in mass due to oxidation, Δm_o can be calculated using equation 4.1 [119]:

$$\Delta m_o = \Delta m_t + (m_l - m_r) \quad (4.1)$$

Where Δm_t is the total change in mass of the sample during curing, m_l is the mass of lubricant added to the sample for compaction, and m_r is the residual mass of lubricant after curing.

The mass of a given sample may increase or decrease during curing based on the amount of lubricant present and the curing parameters including time, temperature and atmosphere. From equation 4.1, it is clear that the overall change in mass of the sample is the difference between the mass gained by oxidation and the mass of lubricant which burns off during heat treatment. If the oxidation process is inhibited, there will be a smaller gain or larger loss of total mass during curing. Furthermore, the formation of conductive oxide bonds between particles reduces the resistivity of the material, so a lack of oxidation will also result in a higher retention of resistivity.

4.2.1 Methodology and Procedures

As-received Ancorsteel 1000C (A1000C) and Ancorlam powders from GKN Hoeganaes Corporation were used for the experimental work described in this chapter. Somaloy 700HR 5P powder from Höganäs AB was also used for comparison purposes. The properties of these materials are given in Section 3.1.1.

Ancorlam consists of A1000C powder with a coating system designed to minimise eddy current and hysteresis losses over a range of frequencies. The exact composition and coating process is proprietary information, but the resulting coating consists primarily of iron and zinc phosphates [124]. The Somaloy 5P series of magnetic powders produced Höganäs AB are a direct competitor to Ancorlam. Somaloy 700HR 5P utilises a similar phosphate based coating system to Ancorlam, but exhibits a coarser average particle size of 250 microns [125].

A lubricant addition of 0.4 wt% Kenolube was premixed into the A1000C, Ancorlam and Somaloy powders as standard as recommended by the powder manufactuers [14] [49]. Due to a long delay in the production of an appropriate die set, “dogbone” specimens were pressed in place of rectangular bar samples. “Dogbone” specimens with a span of greater than 30 mm and square cross section of width 6 mm and height ~6 mm were uniaxially cold compacted in the pressure range of 550 – 830 MPa to a range of target densities in 0.2 g/cm³ increments from 6.0 - 7.4 g/cm³. The change in width from 12 mm to 6 mm is accounted for in the calculation of tramsverse rupture strength (TRS) using equation 3.3. This was later verified experimentally to have no effect on calculated TRS upon arrival of the appropriate rectangular die set capable of producing samples of 12 mm width.

After heat treatment, cured density was measured for all samples. Resistivity was measured using the four point probe method and TRS was measured using the three point bend test as detailed in Section

3.2. Fracture surfaces of the broken samples were polished and etched to permit examination of the microstructure in the SEM.

4.2.2 Results

4.2.2.1 Drop in Strength at High Density

The first experimental step was to quantify the drop in strength of the Ancorlam samples and the density above which this fall occurs. Five samples of Ancorlam powder were pressed for each target density between 6.0 - 7.4 g/cm³ and cured for 1 hour at 450°C in a nitrogen atmosphere. Figure 20 presents the TRS values of these Ancorlam samples after curing.

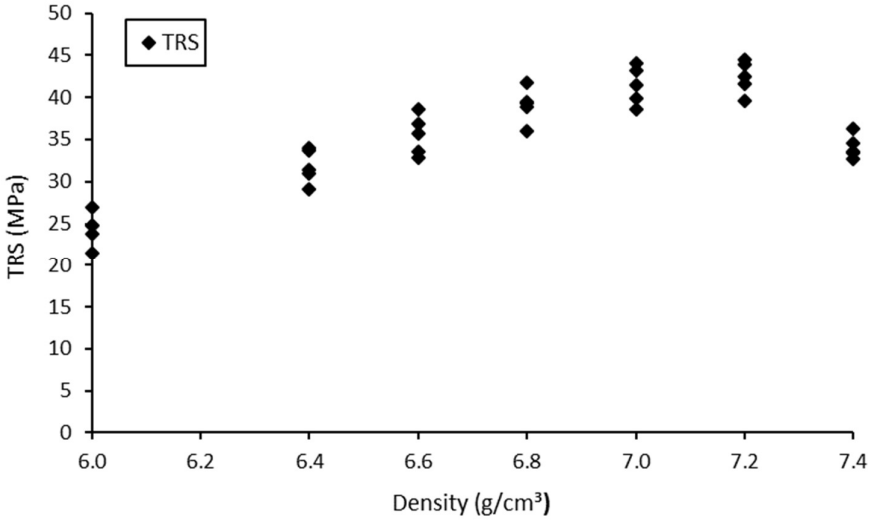

Figure 20: TRS against density for Ancorlam samples cured at 450°C

Figure 20 shows that as density increases from 6.0 g/cm^3 to 7.0 g/cm^3, the mechanical strength of Ancorlam increases linearly. As density increases further from 7.0 g/cm^3 to 7.2 g/cm^3, the strength plateaus. At the maximum density of 7.4 g/cm^3, strength decreases contrary to the hypothesis. This is an issue because magnetic properties improve with increasing density up to and above 7.4 g/cm^3 [14]. This sub-section details the investigation into why strength drops off at high density, with the aim of resolving this issue to be able to exploit both optimal magnetic and mechanical properties.

The initial hypothesis that cured strength should increase linearly with density up to 7.4 g/cm^3 was verified using Somaloy 700HR 5P powder produced by Höganäs AB. The Somaloy powder is a competitor product to Ancorlam, also designed for magnetic performance and utilises a similar phosphate-based coating system. Figure 21 presents the TRS values of both Ancorlam and Somaloy samples pressed to a range of densities from 6.0 - 7.4 g/cm^3 and subsequently cured in a nitrogen atmosphere for 1 hour at 450°C. Both powders were pre-mixed with 0.4 wt% Kenolube prior to compaction.

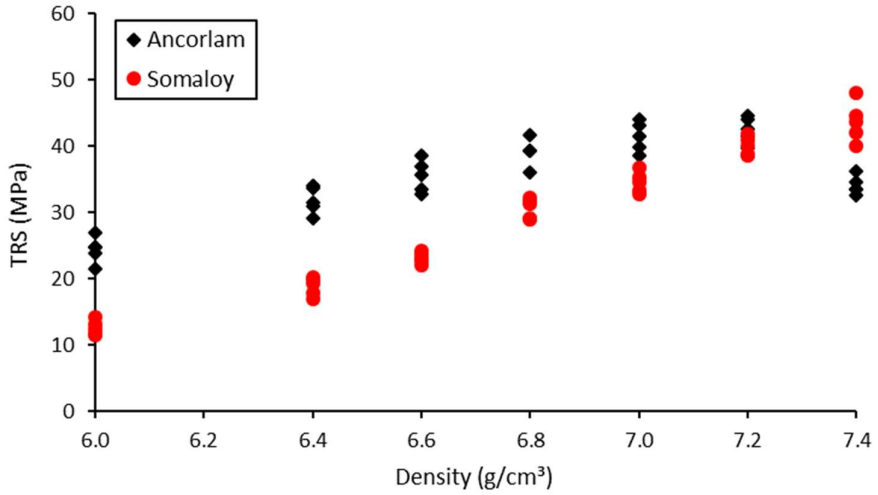

Figure 21: TRS against density for Ancorlam and Somaloy samples cured at 450°C

Figure 21 shows that the intial hypothesis was indeed correct, with the strength of Somaloy improving as density inreases from 6.0 - 7.4 g/cm^3. The strength of Somaloy is lower than that of Ancorlam at all densities measured from 6.0 - 7.2 g/cm^3, with the exception of 7.4 g/cm^3, the density at which magnetic properties are optimal. If the drop in strength of Ancorlam at high density can be resolved, there is potential for superior mechanical performance over Somaloy.

Furthermore, Somaloy shows a larger spread of strength between indidual samples at 7.4 g/cm^3. It is desirable in electric machines for materials to exhibit consistent properties, and therefore the narrower spread of strength data in the Ancorlam powder at 7.4 g/cm^3 is superior.

Figure 22 and Figure 23 show images of unpolished fracture surfaces over a range of densities for cured Ancorlam and Somaloy samples respectively.

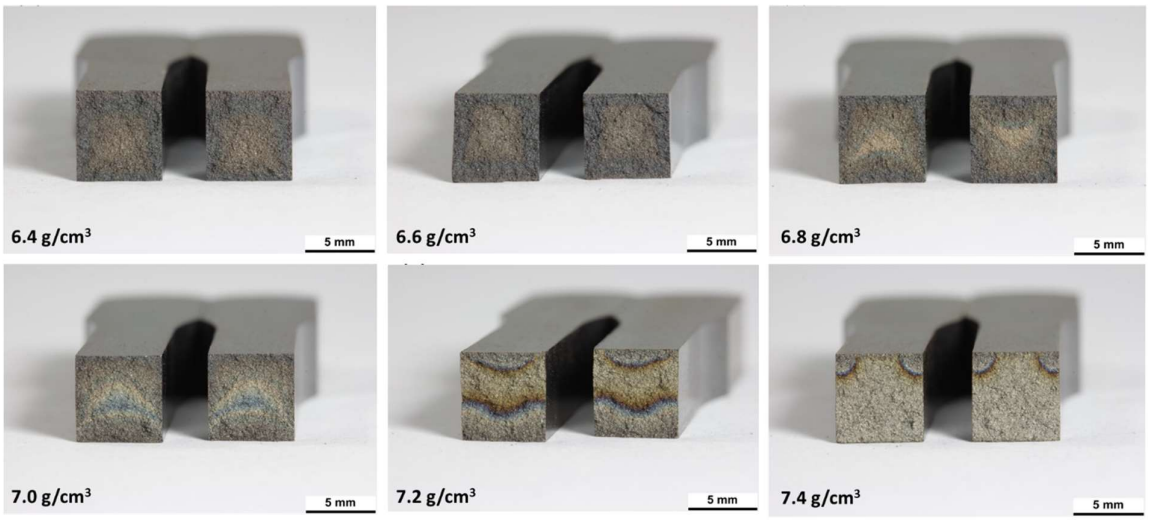

Figure 22: Images of fracture surfaces of cured Ancorlam samples

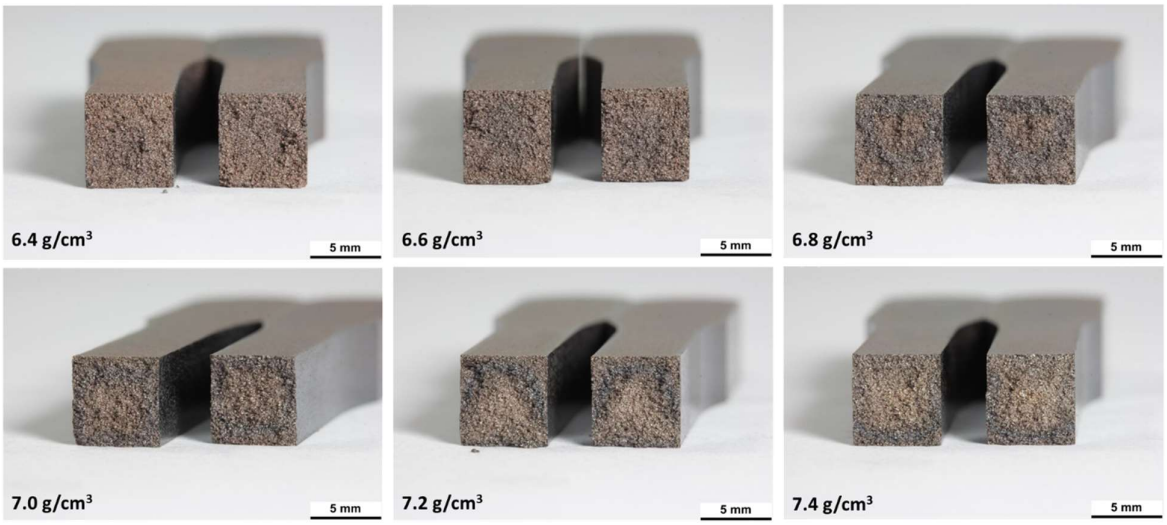

Figure 23: Images of fracture surfaces of cured Somaloy samples

Figure 22 shows at relatively low densities between 6.4 – 7.0 g/cm³, there is a visual difference in the effects of the heat treatment dependent on depth from the exterior edge of the Ancorlam samples. The fracture surfaces are darker at the edges and lighter in the centre, illustrating that the exterior region experiences more oxidation than the interior region. This is in agreement with Lefebvre et al., who observed bright and clean surfaces in regions with no oxidation, slightly darker areas in regions with some oxidation, and dark blue areas in regions with extensive oxidation [120].

At higher densities there is an evident degree of discolourisation on the fracture surfaces of the Ancorlam samples, indicating incomplete lubricant combustion. At a density of 7.2 g/cm^3, these darker lines encompass a lighter interior region where there appears to be less oxidation. The reduced porosity appears to be inhibiting the passage of oxygen into and lubricant combustion products out of the interior region of the sample. At the highest density of 7.4 g/cm^3, these darker lines shift to the corners of the sample, expanding the lighter region to encompass most of the cross-section, indicating low levels of oxidation. The reduced porosity results in closure of the pore network, preventing the passage of oxygen into the interior of the sample for oxidation. These observations corresponds well with the measured drop in strength at high density [Figure 20], reinforcing the conclusion that reduced porosity inhibits the thermal oxidation bonding process.

Figure 23 shows that there is a visual difference in the colour of the interior and exterior regions of the Somaloy samples. As density increases, the contrast between the interior and exterior regions increases, but not sufficiently enough to significantly inhibit the strength of the high density Somaloy samples [Figure 20]. It is noted that there is no discolourisation observed on the fracture surfaces at any density, indiciating complete lubricant burn off. The combination of more extensive oxidation

throughout the cross-section and effective lubricant burn out ensures increasing strength of the Somaloy samples up to the highest density measured.

In order to gain a perspective on the heat treatment mechanisms of Ancorlam powder at a microscopic level, samples were examined under the SEM. Figure 24 shows the SEM image of a polished fracture surface of Ancorlam powder compacted to a density of 7.4 g/cm in the green state prior to curing.

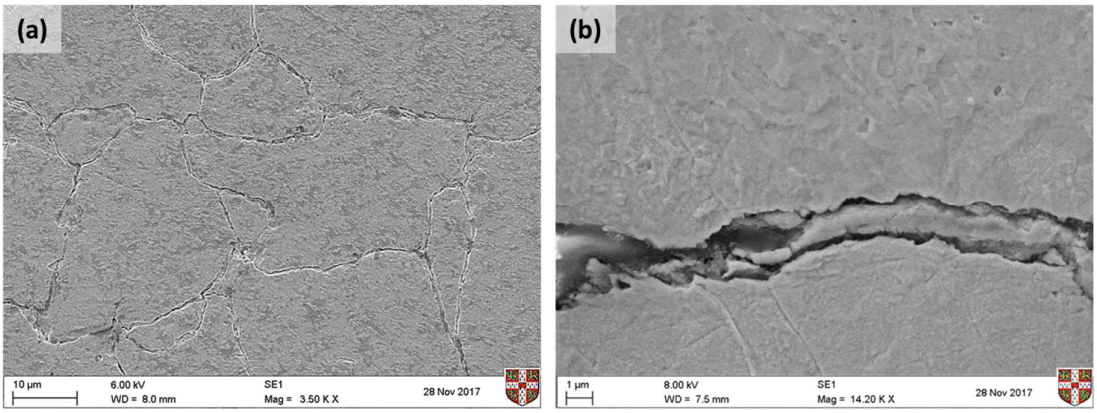

Figure 24: SEM Images of polished fracture surface of Ancorlam compacted to 7.4 g/cm³ in the green state (a) view of multiple iron particles; (b) zoomed in view of coating

Figure 24 shows that the individual iron particles are closely packed and therefore there is little space for oxygen to travel through the pores of the sample. The zoomed-in view shows that the thickness of the coating is approximately 1 micron. There is limited space for oxygen to travel along the particle boundaries at this high density of 7.4 g/cm^3. These observations indicate that thermal oxidation bonding would indeed be inhibited at these high densities.

Figure 25 shows SEM images of an unpolished fracture surface of an Ancorlam sample compacted to a density of 7.4 g/cm³ and cured to the standard parameters.

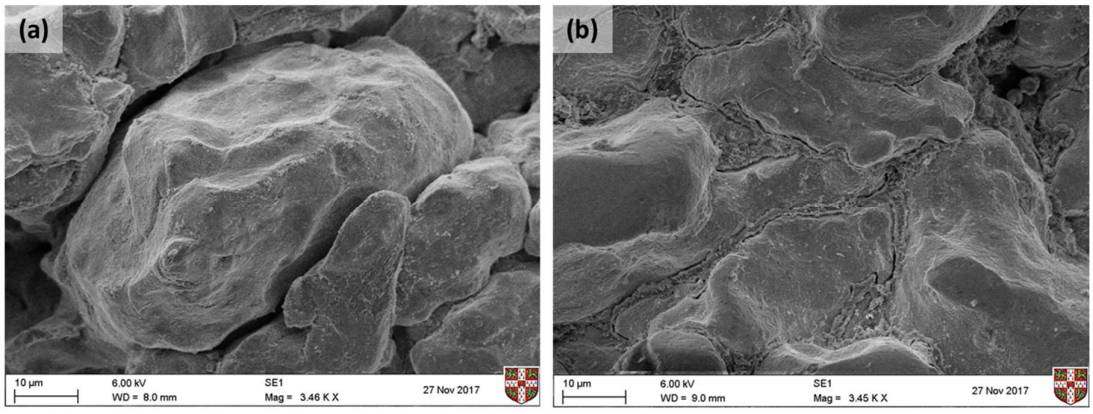

Figure 25: SEM images of unpolished fracture surface of cured Ancorlam compacted to 7.4 g/cm³ (a) near exterior edge of fracture surface; (b) near centre of fracture surface

Figure 25a was captured near the exterior edge of the fracture surface and shows clear evidence of plastic deformation of the individual particles to achieve particle interlocking under the extreme compaction pressures. It is clear that neighbouring outer particles have pulled away from each illustrating intra-particle failure as opposed to inter-particle failure. This indicates that the strength of the sample is governed by the ability of the oxidation layer to hold the particles together.

Figure 25b was taken near the centre of the failure surface and shows a region where the lubricant has been pushed into a large void space in the sample. The lubricant appears to have been unable to burn-off during the curing process due to the lack of porosity in the sample. This shows that at these high densities, porosity is sufficiently low to prevent the passage of oxygen into and out of the sample. Conseqesently, the thermal oxidation bonding process is inhibited in the centre of the sample, limiting strength at high density.

Figure 26 presents SEM images of polished fractures surfaces of Ancorlam samples compacted to 6.8 g/cm³ both in the green state and cured to standard parameters.

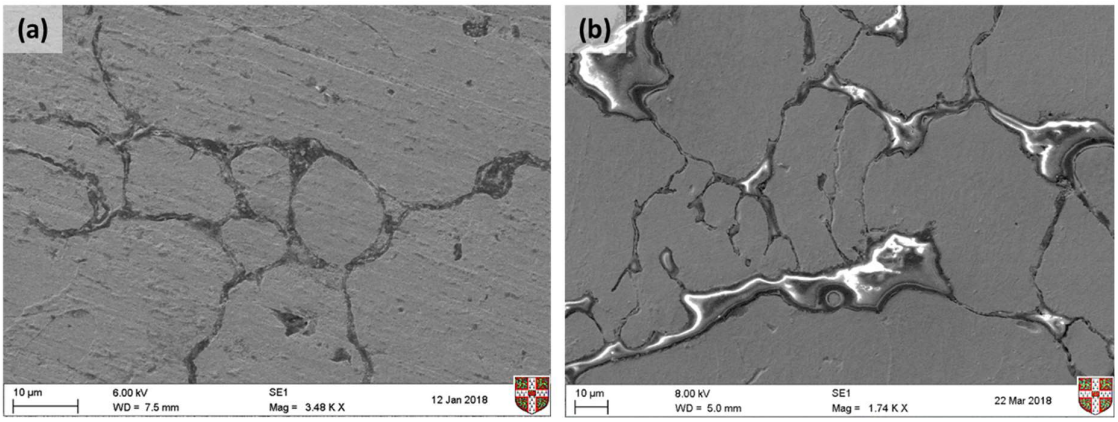

Figure 26: SEM images of polished fracture surface of Ancorlam compacted to 6.8 g/cm³ (a) in the green state; (b) in the cured state

Figure 26a shows a thin coating layer and relatively large void spaces present around the iron particles in the green state. At this reduced density, there is clearly increased porosity and void spaces between iron particles than observed in the sample compacted to a density of 7.4 g/cm^3 [Figure 24]. This increased porosity allows for the passage of oxygen into the interior of the sample. Figure 26b shows clear regions between the iron particles of a more conductive material, showing as bright areas on the SEM image. As the lubricant is not conductive and these regions are not present on the green sample, it follows that these brighter areas are oxide bonds formed during the curing process. It is evident from these SEM images that the relatively large void space present at a density of 6.8 g/cm^3 allows for considerable thermal oxidation bonding.

4.2.2.2 Particle size

These following sub-sections investigate various hypotheses into why the strength falls off at high density in Ancorlam powder, in order to further understand the issue. Somaloy does not experience the same drop in strength at high density as Ancorlam, so the first step involved consideration of the main differences between the two powders. The key difference highlighted was that Somaloy has a coarser particle size as detailed in Section 3.1.1. The smaller particle size of Ancorlam results in smaller voids and more grain boundaries between the particles after compaction.

It is hypothesised that at very high densities, there is insufficient void space in the sample for oxygen to reach the particle interface, therefore inhibiting the thermal oxidation bonding process. To test whether this is true, a batch of Ancorlam with coarser particle size was produced and the strength measured over a range of densities. Standard Ancorlam powder was passed through a sieve of US mesh size #140 (105 microns) and the finer particles were removed. The coarser particles were compacted with 0.4 wt% Kenolube to target densities between 6.0 - 7.4 g/cm^3 prior to curing at 450°C for 1 hour in a nitrogen atmosphere. Figure 27 presents a comparison of the strength of the coarse Ancorlam samples and the standard Ancorlam samples over a range of densities.

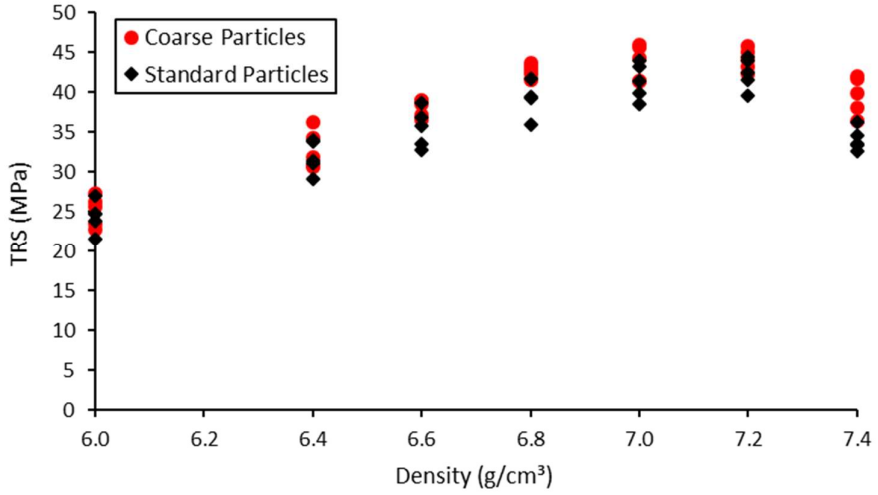

Figure 27: TRS against density for Ancorlam with standard and coarse particle sizes

Figure 27 shows that the strength of the coarse particle mix follows a similar trend to that of the standard particle mix, dropping off at high density and therefore not solving the issue. It is noted that the magnitude in the drop of strength is marginally lower in the coarse particle mix than for standard Ancorlam, possibly due to a slightly increased capacity for thermal oxidation bonding at 7.4 g/cm^3, but this is within normal error margins.

Figure 28 shows the images of unpolished fracture surfaces of cured Ancorlam samples with coarser particle size over a range of densities between 6.4 - 7.4 g/cm^3.

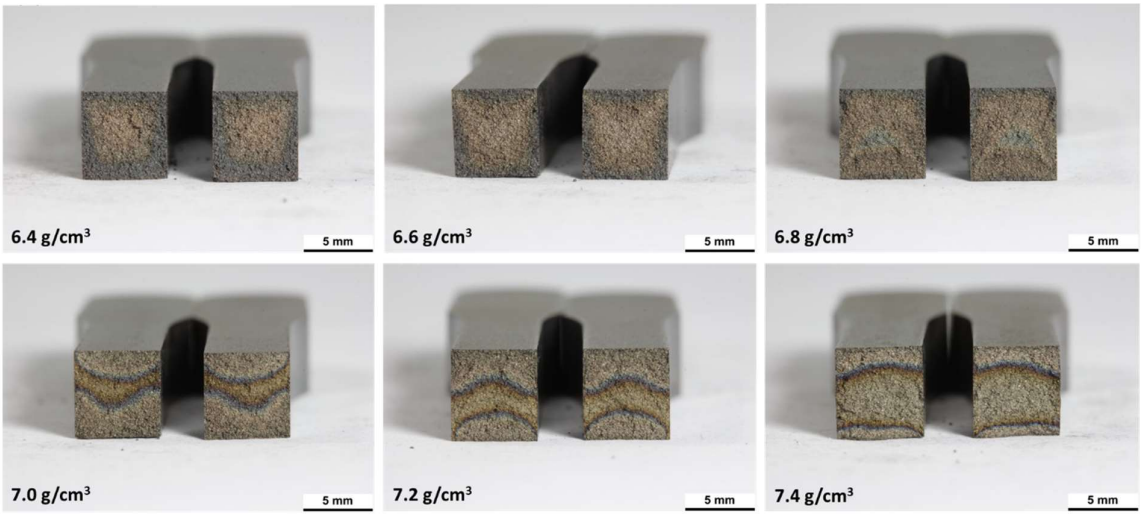

Figure 28: Images of fracture surfaces of cured Ancorlam with coarse particle size

Figure 28 shows the fracture surfaces of the coarse Ancorlam samples are similar to those of the standard Ancorlam samples. There is evident discolourisation across the fracture surfaces at high density where lubricant decomposition products remain in the sample. These lines appear in the higher density samples corresponding to the plateau and eventual drop in mechanical strength. The samples at the highest density of 7.4 g/cm^3 are slightly darker in colour than for the standard Ancorlam powder, indicating a marginal increase in oxidation, in agreement with the improved strength data [Figure 27]. Therefore, from the strength data and images of the fracture surfaces, it is concluded that the use of coarser particles to more closely match the size distribution of Somaloy powder lessened but did not reslove the unexpected drop in strength at high density.

4.2.2.3 Coating Pull-Off

A second hypothesis suggests the Ancorlam coating is not as well adhered to the base iron powder as Somaloy, and the coating is becoming detached during the compaction process. As Ancorlam consists of A1000C powder with a phosphate coating system, this hypothesis was tested by comparing the strength of A1000C samples to that of the Ancorlam samples. If the strength of the uncoated powder samples does not drop off at high density, then it is evident that the addition of the coating is responsible for this drop in strength of Ancorlam.

A set of A1000C powder samples were compacted to target densities between 6.0 - 7.4 g/cm^3 and subject to the same processing procedures as the set of standard Ancorlam samples. Figure 29 presents a comparison of the mechanical strength of A1000C and Ancorlam compacts after curing both for 1 hour at 450°C in a nitrogen atmosphere.

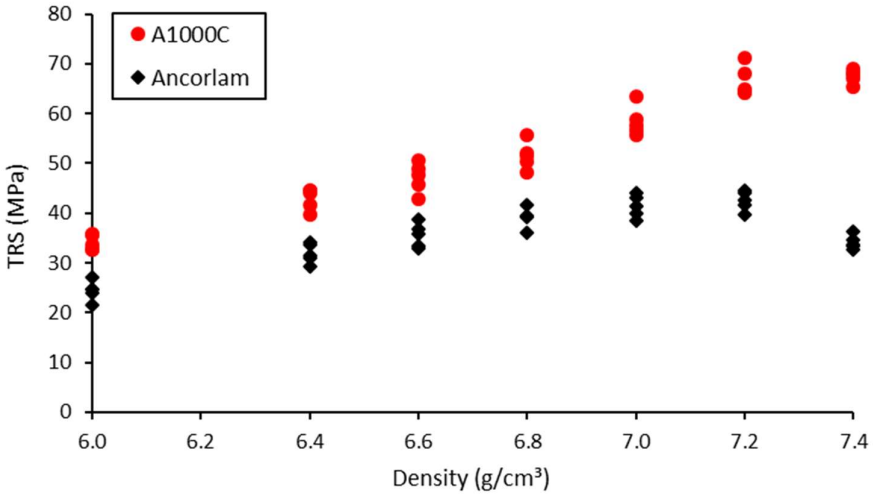

Figure 29: Strength comparison of Ancorlam and A1000C cured at 450°C

Figure 29 shows that the strength of the A1000C powder is greater than that of the Ancorlam powder at all densities measured, due to the pure iron powder being more readily able to form surface oxides. This result is in agreement with the Rebeyrat et al. who found that uncoated iron powder experiences greater mass gain due to oxidation than phosphated iron powder [153]. The phosphate coating acts as a diffusion barrier for the iron particles, slowing down the rate of oxidation. The strength of the uncoated A1000C powder increases as density increases from 6.0 to 7.2 g/cm³. However, strength decreases slightly as density increases from 7.2 to 7.4 g/cm³, showing that the A1000C powder experiences a similar drop in strength at high density as observed in the Ancorlam powder. It is evident from this that the addition of the coating is at minimum not solely responsible for this drop in strength in the Ancorlam powder. Therefore, whilst coating pull-off may be a factor, there are other contributing factors at play.

4.2.2.4 Over-Pressing

A third hypothesis suggests that the strength of Ancorlam powder falls off at high density due to overpressing, specifically by inducing micro-cracks into the sample. To test this, a set of Ancorlam samples were compacted to various target densities between 6.0 - 7.4 g/cm^3 and left in the green state. Should micro cracking be the cause of reduced strength at high density, then this effect will also be present in the green samples. If the drop off only occurs after curing, then it is clear the reason for the drop in strength is due to a difference in the heat treatment behaviour. Figure 30 shows the strength values of Ancorlam samples left in the green state compared to those after curing at 450°C for 1 hour in a nitrogen atmosphere.

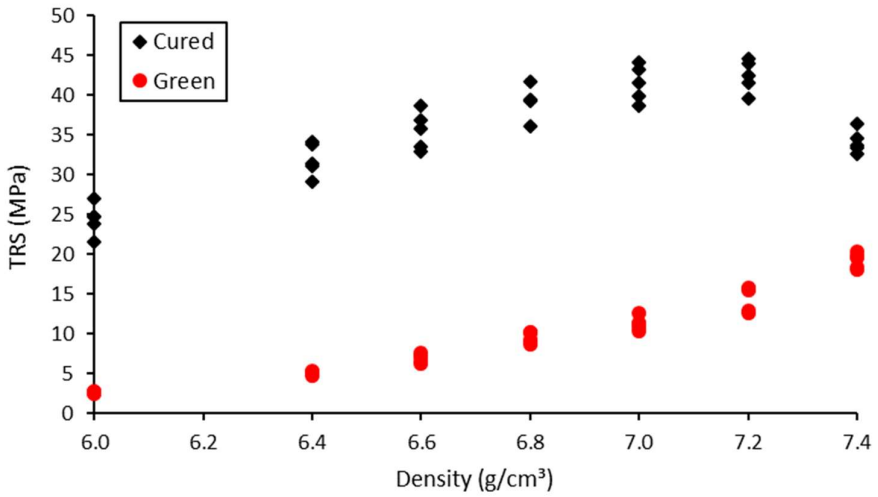

Figure 30: Strength comparison of Ancorlam powder in the green and cured states

Figure 30 shows that strength of the Ancorlam samples in the green state improves as density increases from 6.0 g/cm³ - 7.4 g/cm³, without falling off at high density. This shows that the reason for the drop in strength at high density is a result of an ineffective heat treatment process in samples with a density greater than 7.0 g/cm³. Therefore, it is concluded that the drop in strength of Ancorlam at high density is not caused by over-pressing, but rather that this issue arises during the curing process.

4.2.2.5 Inhibited Thermal Oxidation Bonding

This sub-section investigates possible reasons behind the ineffective heat treatment process at high density. It is hypothesised that the low porosity inhibits the passage of oxygen into and lubricant decomposition products out of the interior regions of the sample. In order to confirm this, the change in mass and resistivity was measured across a range of densities. The target densities were chosen such that they contained the inflexion point around which the strength is maximum in both A1000C and Ancorlam.

Figure 31 shows the change in mass and resistivity of A1000C and Ancorlam samples pressed to a range of densities in the green state and after curing to the standard parameters. All samples contain 0.4 wt% Kenolube as standard.

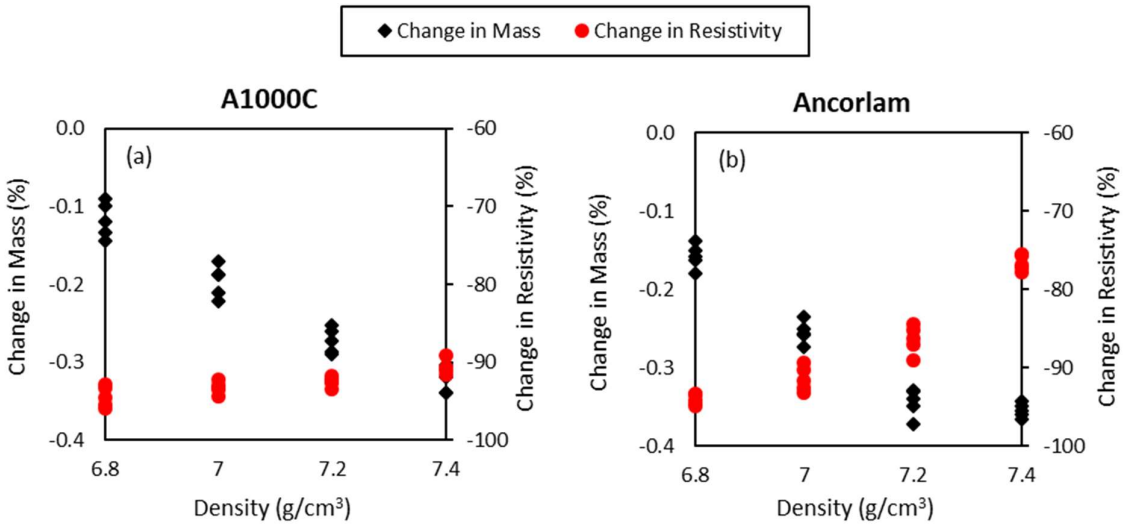

Figure 31: Change in mass and resistivity during curing for (a) pure iron powder; (b) Ancorlam

Figure 31 shows that the overall change in mass during curing for both A1000C and Ancorlam powders is dependent on density. The samples contain 0.4 wt% lubricant, hence in the case of full lubricant burn-off the mass should decrease by 0.4%. However, in most cases residual lubricant decomposition products remain in the sample and the formation of oxides due to thermal oxidation bonding will provide an increase in mass. It is reported in the literature that for lubricants containing zinc stearate, such as Kenolube, the zinc-containing part is not entirely removed at curing temperatures below 600°C [154] [155]. Therefore, it is difficult to predict whether a given sample will experience an overall gain or loss in mass during curing at 450°C [119].

As density increases from 6.8 g/cm³ to 7.4 g/cm^3, both powders show a greater loss in mass during the curing process. This increase in mass loss is due to the decreased porosity limiting the thermal oxidation bonding process, hence there is less weight gain due to oxidation to offset the weight loss by lubricant burn off.

The explanation of inhibited thermal oxidation bonding for the reduced weight gain at high density is reinforced by the corresponding drop in mechanical strength at a density of 7.4 g/cm³ [Figure 20]. At very high densities the internal porosity is limited. As the oxide scale builds up during the curing process, the limited porosity leads to closure of the exterior pores and less penetration of oxygen into the interior pores. This ultimately leads to less extensive oxidation throughout the cross section of the sample and inhibited strength [79]. This difference in the magntiude of oxidation between the interior and exterior areas of the sample was observed in the lighter and darker regions in the cross sectional views of the Ancorlam samples [Figure 22].

There is a smaller loss in mass at all densities for the A1000C samples compared to the Ancorlam samples due to the increased levels of thermal oxidation bonding, as further evidenced by the improved strength of A1000C [Figure 29]. This result is in agreement with Rebeyrat et al., who found that the addition of a phosphate coating inhibits the oxidation process [153]. The loss in mass plateus above a density of 7.2 g/cm^3, despite reduced levels of thermal oxidation bonding suggested by the drop in strength. This plateau in the mass loss is due to the lack of porosity preventing full lubricant burn off, hence the sample retains more mass during the curing process.

Figure 31 shows that as density is increased, there is greater retention of resistivity in both A1000C and Ancorlam powders. This is due to the inhibited formation of conductive oxide bonds and a greater amount of residual lubricant products remaining in the sample. The A1000C powder does not retain resistivity as well as Ancorlam due to greater levels of oxide bonding. This finding agrees with the smaller mass loss and drop in strength at high density of A1000C compared to Ancorlam [Figure 29].

Due to the combination of greater loss in mass and retention of resistivity in Ancorlam samples at very high density, it is concluded that the thermal oxidation bonding process is indeed inhibited, resulting in reduced mechanical strength.

4.3 Minimising Thermal Oxidation Bonding

The drop in strength of Ancorlam at high density was previously found to be, at least in part, due to the inhibited thermal oxidation bonding process. In this section, the extent of thermal oxidation bonding is quantified to further understand this heat treatment mechanism.

4.3.1 Methodology and Procedures

In order quantify the mass gain due to thermal oxidation bonding, the opposing effect of mass loss due to lubricant burn off was removed. Traditional compaction using a punch and die set cannot be performed without the use of a lubricant as this would damage the tool set. Therefore, samples were compacted without lubricant using a cold isostatic press (CIP) to a target density of 6.8 g/cm^3 (as limited by the maximum operational pressure).

Thermo-gravitational analysis (TGA) was used to measure the change in mass during the curing process, as described in Section 3.2.1. Samples of A1000C powder, Ancorlam powder, and an empty crucible acting as a control sample were heat treated for 1 hour at 450°C in a nitrogen atmosphere. A constant ramp rate and cooling rate of 10°C/min was used, to keep the total heat treatment time consistent between samples. Due to the sensitive nature of the balance, a constant gas flow rate of 0.1 l/min was used, as the flow of gas could affect the measurement of sample mass as explained in section 3.2.1. The control sample was used to calculate the effect of the gas flow on the crucible such

that this value can be subtracted to find the actual gain in mass attributed to thermal oxidation bonding.

To ensure the results of the TGA carried over to the standard curing process, a second batch of A1000C and Ancorlam samples were pressed without lubricant in the CIP and subsequently cured for 1 hour at 450°C in a nitrogen atmosphere in the tube furnace. The change in mass was measured and compared to the results of the TGA analysis.

4.3.2 Results

TGA was performed for Ancorlam, A1000C and an empty control sample. Testing of the robustness of the cured samples by hand showed that both Ancorlam and A1000C possesed greater strength than in the green state. As the curing temperature of 450°C is far below the sintering temperature of iron, it is evident from this that some degree of thermal oxidation bonding had occurred during the heat treatment process. A plot of sample mass and temperature profile against time is given in Figure 32.

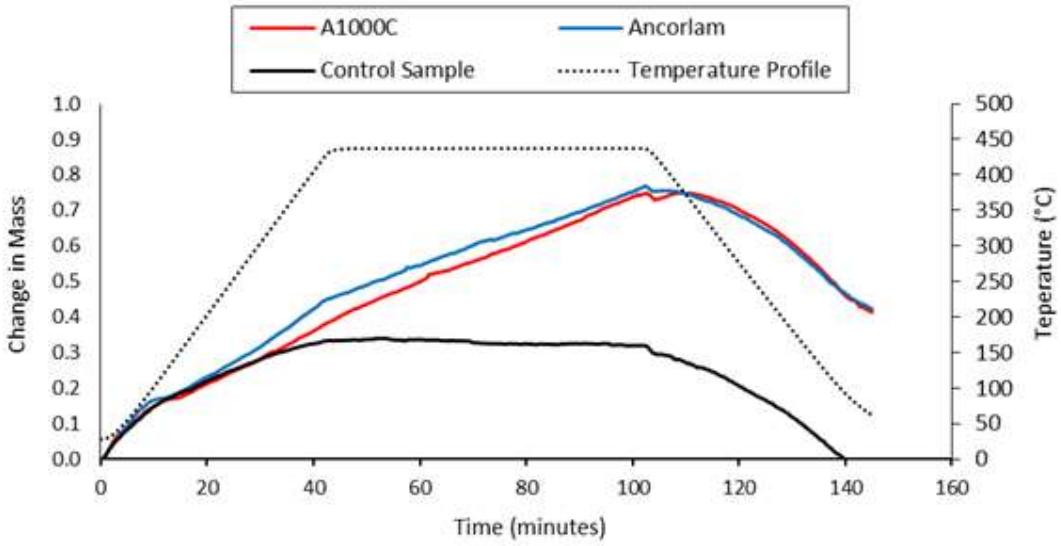

Figure 32: TGA change in mass during curing

Figure 32 shows that the TGA registered a gain in mass for all samples when heated from ambient temperature to 450°C over the first 45 minutes. The apparent gain in mass of the control sample is due to the effects of the changing density of the atmosphere inside the furnace as it is heated. As the temperature of a gas increases, its volume increases and density decreases [156]. In solids, such as the empty ceramic crucible used in the control sample, the increase in volume is negligible, as is the decrease in density. Therefore, the relative mass of the empty crucible increases relative to the gaseous atmosphere, registering an apparent increase in mass whilst the furnace temperature is elevated.

The increase in mass of the Ancorlam powder deviates from that of the control sample at approximately 200°C, whilst the mass of the A1000C powder deviates at approximately 300°C. This deviation from the control sample indicates the onset of actual weight gain or oxidation of the powder samples. The level of actual mass gain of the powders relative to the control sample can be more easily observed in Figure 33 which shows the normalised mass of the two powders during the curing process.

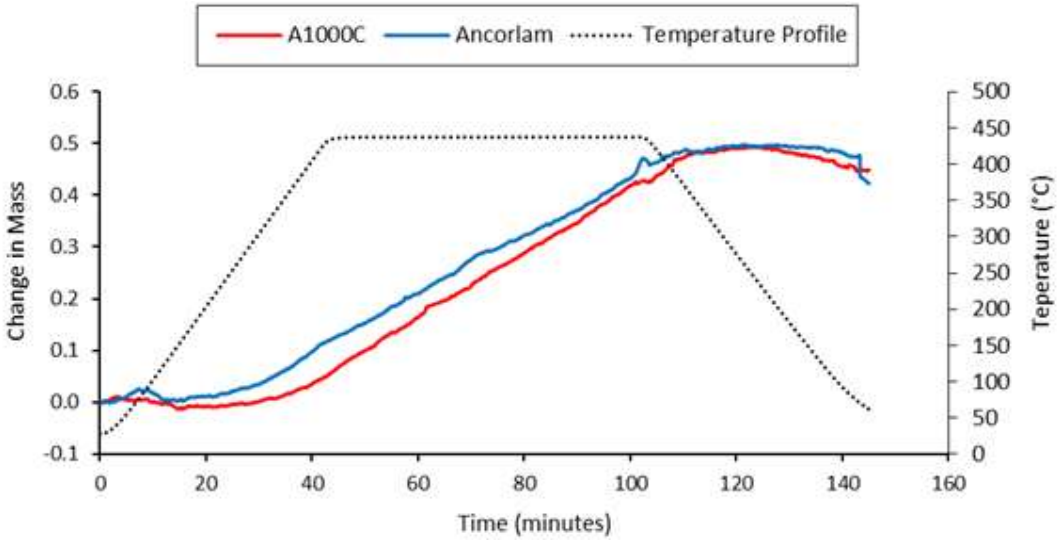

Figure 33: TGA normalised change in mass during curing

Figure 38 shows that the Ancorlam powder begins to oxidise at a lower temperature than the A1000C powder. It is clear that both samples begin to oxidise and therefore gain mass before the furnace reaches the full temperature. The weight of both powders continues to increase whilst the temperature is held at 450°C for an hour, up until the temperature falls below 250°C. This suggests that both powders have not reached saturation oxidation during this heat treatment cycle. Further testing for a longer duration is required to confirm whether this is true.

The results of the TGA are compared to those of the two powders compacted to the same parameters and heat treated in the tube furnace to the standard curing cycle. Table 9 presents a comparison of the total gain in mass of each powder in the TGA and the tube furnace.

Heat Treatment	Powder	Density (g/cm^3)	Initial Mass (g)	Final Mass (g)	Change in Mass (g)	Change in Mass (%)
TGA	A1000C	6.80	0.1702	0.1706	0.0004	**0.24**
TGA	Ancorlam	6.83	0.2503	0.2507	0.0004	**0.16**
Tube Furnace	A1000C	6.81	29.67	29.74	0.07	**0.24**
Tube Furnace	Ancorlam	6.84	33.04	33.10	0.06	**0.18**

Table 9: Comparison of TGA and standard curing process for Ancorlam and A1000C samples

The A1000C sample gained a total of 0.243% mass during the TGA analysis, and 0.237% during curing in the tube furnace, showing a good match between the two analyses. The Ancorlam sample gained a total of 0.169% mass during the TGA analysis, and 0.183% during the standard curing process, again showing a good match. In both types of analysis, the A1000C powder experienced a greater percentage increase in mass than the Ancorlam powder, demonstrating greater levels of thermal oxidation bonding. These findings agree with earlier conclusions that A1000C powder is found to be stronger than the Ancorlam powder due to this increased level of oxidation bonding [Figure 29]. This is due to the coating material inhibiting the formation of oxides on the surface of the iron powder [153].

Furthermore, these results also agree with the conclusion that A1000C powder experiences less overall weight loss than Ancorlam in samples compacted using lubricant, due to greater levels of oxidation (assuming equal lubricant burn-off) [Figure 31]. It is also noted that due to an overall loss in mass during heat treatment in samples with lubricant, the mass loss due to lubricant burn off outweighs the mass gain due to oxidation, in agreement with the findings of Lefebrve et al. [119].

4.4 Control of Thermal Oxidation Bonding

4.4.1 Metholodology and Procedures

The extent of thermal oxidation bonding influences the mechanical and electrical properties of Ancorlam samples in the cured state. As the extent of oxidation increases, mechanical strength increases at a cost to the resistivity [Section 4.2]. Therefore, being able to predict or control the level of thermal oxidation bonding would be useful for producing components with a balance of mechanical and magnetic properties to suit the desired application.

In this section, the lower limits of oxidation were explored by removing various oxygen sources, with the aim of decreasing the rate of oxidation towards zero. Five main sources of oxygen were identified in the Ancorlam samples; surface oxides on the iron powder, oxygen impurities in the iron powder, oxygen in the phosphate (PO_4) coating, oxygen in the lubricant and oxygen available in the furnace atmosphere.

4.4.2 Results

4.4.2.1 Removal of Coating

The oxygen present in the phosphate coating of Ancorlam can be eliminated by using uncoated iron powder (A1000C). A comparison between the oxidation levels of coated and uncoated iron powder samples cured in a standard furnace was made in Section 4.2. Uncoated iron powder was found to have greater levels of thermal oxidation bonding and therefore greater strength than Ancorlam at all

densities measured. This result shows that rather than providing a potential a source of oxygen, the coating material actually inhibits the thermal oxidation process by acting as a barrier for the diffusion of oxygen to the particle boundaries.

4.4.2.2 Removal of Lubricant

The lubricant used during compaction provides an oxygen source in the internal pores of the sample. In order to remove this oxygen source and measure the influence on the level of thermal oxidation bonding, samples without lubricant were produced.

A set of five uncoated iron powder (A1000C) samples were compacted in the CIP with no lubricant to a target density of 6.8 g/cm^3. Compaction to greater densities towards 7.4 g/cm^3 was not possible due to the CIP being limited to a pressure of 600 MPa. These samples were compared to previously produced samples compacted in a uniaxial punch and die set with 0.4 wt% Kenolube to the same target density [Section 4.3]. Table 10 presents a comparison of the key properties for each set of samples. Each value quoted was calculated as an average of the five samples in the given set.

Press	Lubricant	Density (g/cm^3)	Change in Mass (%)	Resistivity (mΩcm)	Strength (MPa)
Uniaxial	0.4 wt% Kenolube	6.78	-0.12	0.313	50.60
CIP	None	6.80	0.22	0.251	47.50

Table 10: Effect of curing with and without lubricant on properties of A1000C

Table 10 shows similar levels of strength and resistivity between the batches of samples both with and without lubricant. The average gain in mass due to oxidation of the A1000C samples without lubricant was 0.22 wt% after curing. This demonstrates good repeatability, agreeing well with an earlier batch of samples processed to the same conditions, which measured a 0.237 wt% mass gain due to oxidation [Table 9]. The average change in mass during curing of samples containing lubricant was a loss of 0.12 wt%. Assuming full lubricant burn out, the adjusted mass gain due to oxidation in these samples would be 0.28 wt% for a 0.40 wt% lubricant addition.

The adjusted mass gain due to oxidation was 0.06 wt% greater in the samples containing lubricant than those without (0.28 wt% versus 0.22 wt%). This difference may be attributed to incomplete lubricant burn out, resulting in 0.06 wt% of lubricant, or 15% of total lubricant remaining in the sample after curing. Renowden and Pourtalet found that around 94% of EBS lubricant and 80% of zinc stearate lubricant is removed after curing at 550°C in a nitrogen atmosphere [118]. As Kenolube is a mixture of EBS and zinc stearate, it is plausible to conclude that the extra mass gain equivalent to 15% of the lubricant addition is indeed due to incomplete lubricant burn off. Furthermore, this explanation is

backed up by the larger resistivity value of the samples with lubricant, as the insulating properties of the residual lubricant increase resistivity. Therefore, when also considering sample variation and experimental error, it is not evident that the oxygen present in the lubricant made a signficant contribution to the extent of thermal oxidation bonding.

From the above results, it can be concluded that the lubricant is at least not the main source of oxygen for the thermal oxidation bonding process at a density of 6.8 g/cm^3. At these low densities, there is sufficient porosity in the sample for atmospheric gases to travel into and out of the sample. However, further analysis is required into samples pressed to a density of 7.4 g/cm^3 where the pore network is closed. At this density, there may be more lubricant trapped in the pores and less atmospheric oxygen reaching the interior of the sample. Consequently, oxygen in the lubricant will be a proportionally more significant source of oxygen.

4.4.2.3 Removal of Atmospheric Oxygen

The furnace atmosphere is another potential source of oxygen into the samples, as the tube furnace used for curing is not completely air tight and the flow of nitrogen gas may contain a very small amount of oxygen. The nitrogen gas used has a purity of 4N (99.99%) and therefore still contains a trace amount of impurities, including oxygen. Lefebvre et al. found that curing SMC materials in a reducing atmosphere of hydrogen resulted in lower levels of oxidation than curing in nitrogen or air at ambient pressure [120]. In order to further reduce the residual oxygen in the furnace atmosphere, samples were cured in a sealed vacuum furnace. Three different gases were passed through the vacuum furnace during curing to flush out any air; standard nitrogen, argon and 5% hydrogen in argon. Argon was selected due to being inert, and hydrogen selected due to being a reducing gas, with the intent of reducing oxides already formed on the iron powder.

Twenty A1000C powder samples were pressed without lubricant in the CIP in order to eliminate two potential sources of oxygen in the coating and the lubricant. Samples were compacted to a target density of 6.8 g/cm^3 in order to ensure sufficient porosity for the atmospheric gases to be able to disperse into and out of the interior pores of the samples, and therefore measure the effects of varying the atmosphere. Five of these samples were left in the green state to measure resistivity and strength prior to curing, as a benchmark for zero thermal oxidation bonding. All other samples were cured in the vacuum furnace at 450°C for one hour with a flow of various different gases. Five samples were cured with a flow of nitrogen, a further five with a flow of argon gas and the final five samples were cured with a flow of 5% hydrogen in argon.

Table 11 presents the key properties of all sets of samples. Each value quoted was calculated as an average of the five samples in the given set.

Heat Treatment	Gas	Density (g/cm^3)	Change in Mass (%)	Resistivity (mΩcm)	Strength (MPa)
None	n/a	6.78	n/a	36.900	10.38
Tube Furnace	Nitrogen	6.80	0.22	0.251	47.50
Vacuum Furnace	Nitrogen	6.81	0.55	0.165	57.92
Vacuum Furnace	Argon	6.82	0.59	0.156	58.41
Vacuum Furnace	5% Hydrogen	6.83	0.64	0.122	68.62

Table 11: Effect of curing in different atmospheres in a vacuum on properties of A1000C

Table 11 shows that curing in the vacuum furnace with a flow of nitrogen produces a greater increase in mass, decreased resistivity and increased strength versus curing in the standard tube furnace. All of these results indicate a greater extent of thermal oxidation bonding. Curing in a vacuum with a flow of inert gases such as nitrogen or argon produces a similar change in mass, resisitivity and strength to one another. However, curing in a vacuum furnace with a flow of 5% hydrogen in argon acting as a reducing gas produces an even greater increase in strength and mass, and even lower resistivity.

Contrary to the initial hypothesis, the use of a vacuum to reduce the levels of atmospheric oxygen actually increases the extent of the thermal oxidation bonding process. Furthermore, curing in a vacuum furnace with a flow of reducing gas does not inhibit the oxidation bonding process, but increases it further. Evidently, the oxygen partial pressure inside the furnace remains sufficient for the iron to be able to oxidise.

The required oxygen partial pressure for oxidation of iron to occur was estimated using a Richard-Ellingham diagram. The Richard-Ellingham Diagram is a graphical respresentation of the standard Gibbs free energy changes for chemical reactions to be possible. It can be used to determine the necessary furnace conditions for prevention of unwanted oxidation of metals or the reduction of metal oxides. The required oxygen partial pressure for the oxidation of metal at a given temperature can be determined from the diagram. At the curing temperature of 450°C, the required oxygen partial pressure for the oxidation of iron into magnetite (Fe_3O_4) is $1x10^{-42}$ [157].

The vacuum pump is rated to a minimum pressure of 0.1 Pa or $1x10^{-6}$ atm (atmospheres). The purity level of the gases used was 4N or 99.99 vol%, giving 0.01 vol% impurities or $1x10^{-4}$ atm. Combined, the partial pressure of impurities is $1x10^{-10}$ atm. Therefore, the vacuum pump is simply not strong enough to achieve a sufficiently low oxygen partial pressure to prevent oxidation ($< 1x10^{-42}$), even with the use of an inert or reducing atmosphere of high purity.

R. J. Hussey and M. Cohen studied the rate of oxidation of iron in the temperature range 450 - 550°C for the pressure ranges of $1x10^{-9}$ - $1x10^{-7}$ atm and $1x10^{-6}$ - 1 atm [158] [159]. In the pressure range of $1x10^{-9}$ - $1x10^{-7}$ atm and at a temperature of 450°C, oxidation rate and total oxide thickness increase with decreasing oxygen partial pressure. This is in agreement with the results of Table 11, offering an explanation for why the levels of oxidation increased after reducing the available oxygen in the furnace atmosphere.

Furthermore, Boggs et al. found that at temperatures between 220°C and 450°C and pressures in the range of $1x10^{-5}$ - 0.1 atm, the extent and rate of oxidation in the first three hours also increased as oxygen partial pressure was decreased [160]. This again corresponds well to the results of Table 11, as the samples pass through this temperature region for up to three hours as the vacuum furnace is heated at 10°C/min up to 450°C. This initial period of rapid oxidation led to the formation of magnetite (Fe_3O_4), as predicted by the Richard-Ellingham diagram at this temperature [157]. It should be noted however that whilst the initial rate of oxidation in the first three hours increases with decreasing oxygen partial pressure, the long term rate of oxidation decreases. After very long curing times of 96 hours, the total oxide thickness is larger in samples exposed to higher oxygen partial pressures in the pressure range of $1x10^{-5}$ - 1 atm [159]. This is also in agreement with Caplan et al., who found that oxidation rate is initially high in cold worked iron at all pressures in the range of $1x10^{-3}$ - 1 atm, but slows as oxide layer thickens, particularly at the lower end of the oxygen pressure range [161].

The vacuum furnace provides a method of increasing strength at the cost of decreasing resistivity for curing durations up to at least three hours. However, the samples measured contained no lubricant and were at a particularly low density due to the limitations of the CIP. Therefore, this improvement in strength may not transfer to high density samples where the pore networks are more closed and the furnace atmosphere is unable to penetrate into the interior regions of the sample. The use of the vacuum furnace as a method of increasing strength was investigated further in Section 4.5 for higher density samples including lubricant and coated iron powder, to mirror typical production conditions.

This section investigated three potential sources of oxygen, removing each in turn to gauge their influence on the overall levels of thermal oxidation bonding in the sample. The removal of the lubricant had neglible effect on reducing the extent of thermal oxidation bonding. The removal of the oxygen containing phosphate coating actually increased the levels of oxidation as pure iron powder is able to more readily form surface oxides than coated iron powder [153]. Reducing the levels of oxygen in the furnace through the use of a vacuum and various inert or reducing atmospheres also increased the levels of thermal oxidation bonding at the temperature regimes investigated. It is therefore concluded that for standard Ancorlam samples compacted with lubricant to relatively low densities of

6.8 g/cm^3, the oxides already present on the surface of the iron powder and the oxygen in the furnace atmosphere are the main sources of oxygen.

4.5 Optimising Thermal Oxidation Bonding

In order to further understand the oxidation bonding process in Ancorlam powder, a number of different variables including curing time, temperature and atmosphere were altered and their effects measured. Beyond a greater understanding of the heat treatment mechanisms, this section aims to achieve high strength components whilst still retaining sufficient resistivity. It is hypothesised that increasing curing time and temperature will lead to a greater extent of thermal oxidation bonding in Ancorlam samples, as is the case for pure iron [159]. Furthermore, curing in a vacuum has previously been shown to increase the strength of lower density uncoated iron powder samples [Section 4.4]. This section shall extend this work and investigate whether this increased strength carries over into higher density coated iron powder samples.

4.5.1 Methodology and Procedures

Ancorlam powder was premixed with 0.4 wt% Kenolube and compacted into bar samples. Twenty-five samples were compacted to each target density; 6.8 g/cm³, 7.0 g/cm³, 7.2 g/cm³ and 7.4 g/cm³.

To investigate the effects of increasing curing temperature, the first five samples of each density were cured at 600°C for one hour in a nitrogen atmosphere, instead of the standard 450°C. This temperature was selected as it is slightly beyond the temperature at which the phosphate coating degrades [31]. If strength is greater despite the degradation of the coating, this provides further proof that the thermal oxidation process and not the coating material is responsible for the increase in strength of Ancorlam during curing.

The next five samples of each density were cured for 24 hours at 450°C in a nitrogen atmosphere, rather than the standard one hour, in order to measure the effects of increasing curing time. This duration is selected as an upper bound of what is economically viable for producing SMC components as advised by the powder manufacurers, due to the large energy costs of running a furnace at that temperature for that duration of time. It was hypothesised that at low densities, the longer duration would lead to an increased thickness of oxide layer and hence increased strength of the Ancorlam samples. It was however not easy to predict whether the increased curing duration would allow for further oxidation and increased strength of very high density samples, or if the pores would become closed off preventing any further oxidation.

The remaining fifteen samples of each density were cured in a vacuum furnace for one hour at 450°C using various atmospheres. Five samples of each density were cured using a flow of nitrogen gas, five

in argon gas and the last five in 5% hydrogen in argon. These atmospheres were chosen as per section 4.4 in order to test whether the increase in strength observed in low density, pure iron powder samples compacted without lubricant would translate to Ancorlam samples compacted with lubricant to very high densities.

4.5.2 Results

4.5.2.1 Curing Temperature

Figure 34a presents a comparsion of the strength of Ancorlam samples over a range of densities from 6.8 - 7.4 g/cm^3 after curing at 450°C and 600°C, both for one hour in a nitrogen atmosphere. Figure 34b shows the change in mass and resisitivity of the batch of Ancorlam samples cured at 600°C compared to in the green state prior to curing.

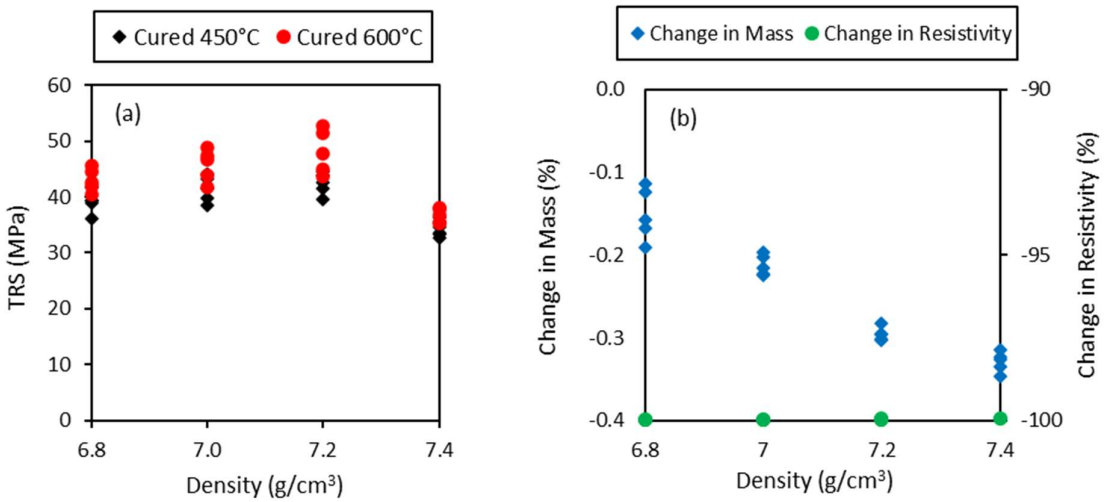

Figure 34: (a) Effect of curing temperature on strength of Ancorlam; (b) Change in mass and resistivity of Ancorlam after curing at 600°c

Figure 34a shows that increasing the curing temperature from 450°C to 600°C results in a gain in strength at all densities measured, although the increase at the highest density of 7.4 g/cm^3 is not statistically signficant. Figure 34b shows that resistivity is completely diminished during curing, with almost 100% loss in resisitivity versus the green state. Comparing the mass loss of Ancorlam samples cured at 600°C to those cured at 450°C [Figure 31b], it is observed that mass loss is reduced slightly after curing at 600°C due to increased levels of thermal oxidation bonding. From the above results, it is concluded that increasing curing temperature from 450°C to 600°C results in a greater level of thermal oxidation bonding, and hence greater strength of Ancorlam samples.

This result is in agreement with Rebeyrat et al. who concluded that increasing curing temperature from 350 - 700°C results in increased levels of oxidation of loose (uncompacted) phosphated iron

powder cured in artificial air [153]. Rebeyrat et al. found there were two different oxidation phenomenon in phosphated iron powders dependent on the curing temperature and duration. At 350°C, oxidation is initially controlled by the outward diffusion of iron through the phosphate layer, whilst at curing temperatures ≥ 450°C the oxidation mechanism switches to one controlled by the diffusion of iron in the oxide, as is the case in uncoated iron powder and bulk iron. These two oxidation mechanisms would occur during heating of the furnace and holding at the ultimate curing temperature, with the latter being more prominent in samples cured at 600°C.

It is clear from the loss of resistivity that the phosphate based coating was diminished after curing at 600°C. Given the combination of an increase in strength and deterioration of the coating, it is concluded that the coating is not responsible for the strength of Ancorlam. Whilst strength increased after curing at 600°C rather than 450°C. the complete degradation of the coating and resistivity shows that this is not a viable method of increasing strength for magnetic applications.

4.5.2.2 Curing Time

Figure 35a presents a comparsion of the strength of Ancorlam samples over a range of densities after curing for 1 hour and 24 hours, both at 450°C in a nitrogen atmosphere. Figure 40b shows the change in mass and resisitivity of the batch of Ancorlam samples cured for 24h compared to in the green state prior to curing.

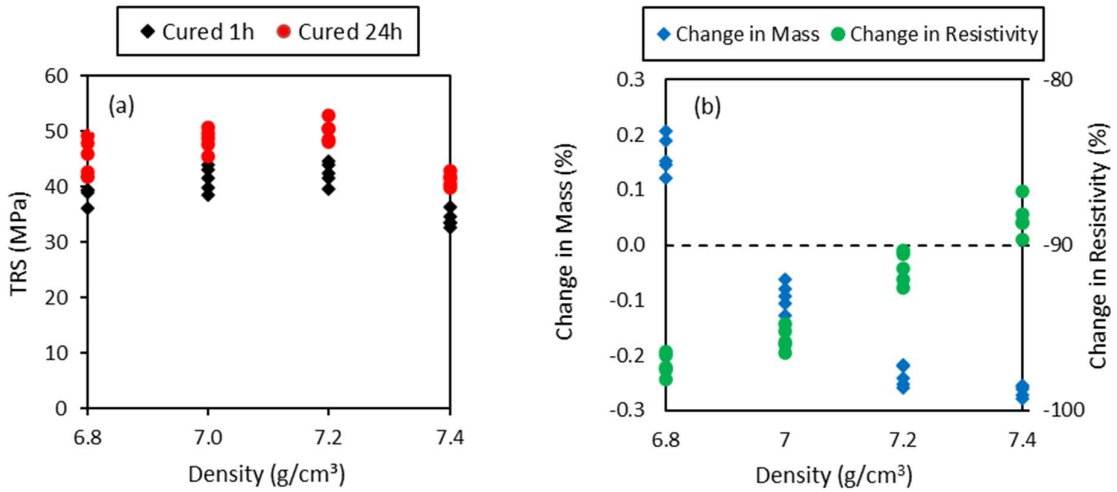

Figure 35: (a) Effect of curing duration on strength of Ancorlam; (b) Change in mass and resistivity of Ancorlam after curing for 24 hours

Figure 35a shows that extending the duration of curing from 1 hour to 24 hours increases the bending strength of Ancorlam samples at all densities measured, indicating that these samples had not reached saturation oxidation after 1 hour. Comparing Figure 31b and Figure 35b shows that there is a smaller loss in mass and a greater loss in resistivity for the Ancorlam samples cured for 24 hours rather than

1 hour. These results are explained by increased levels of thermal oxidation bonding leading to increased strength, decreased resisitivity and decreased loss In mass. At a density of 6.8 g/cm^3, the increased levels of thermal oxidation bonding lead to a gain in mass outweighing the loss in mass due to lubricant burn off, resulting in an overall net gain during the curing process.

These results agree with the earlier findings during thermogravimetric analysis, where it was found that the Ancorlam powder had not reached saturation oxidation during curing at 450°C for 1 hour [Figure 33]. Further testing for a longer duration has indeed confirmed that mass and hence strength continue to increase as curing duration is lengthened. It is reported in the literature that excessive oxidation can lead to a thick oxide scale which actually decreases strength [79]. However, this appears to not be the case for these Ancorlam samples, at least for curing durations up to 24 hours.

The results are in agreement with R. J. Hussey and M. Cohen who found that the weight gain and oxide thickness of iron treated at 450°C increased rapidly in the first hour before the rate of oxidation, and therefore strength gain, levelled off [159]. However, the oxidation process did not reach a maximum until almost 96 hours, showing whilst not economically practical, curing for even longer could yield further strength increases in Ancorlam powder.

4.5.2.3 Curing in Vacuum with Nitrogen

Figure 36a presents a comparsion of the strength of Ancorlam samples over a range of densities after curing at standard pressure and in a vacuum, both at 450°C for 1 hour with a flow of nitrogen gas. Figure 41b shows the change in mass and resisitivity of the batch of Ancorlam samples cured in the vacuum furnace compared to in the green state prior to curing.

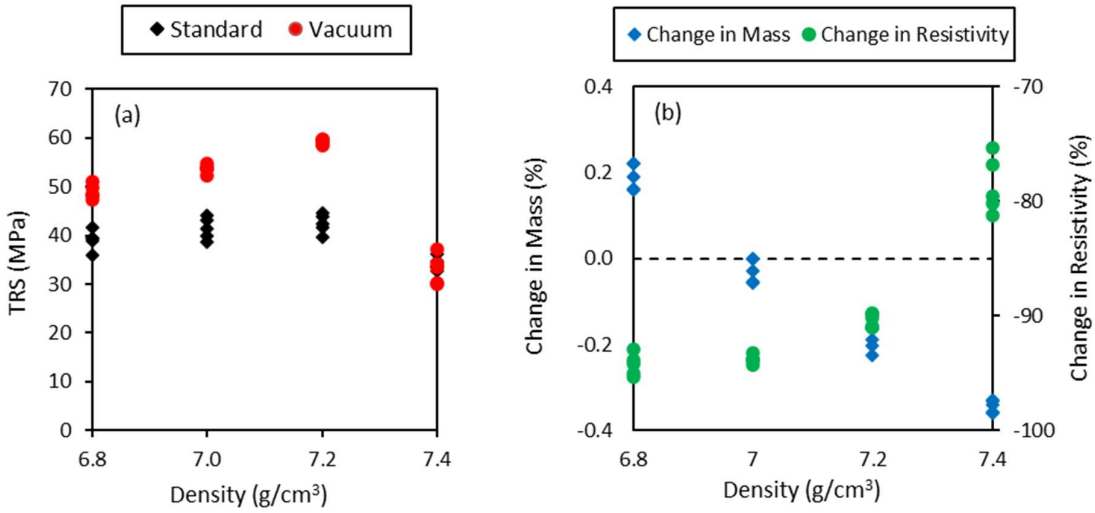

Figure 36: (a) Effect of curing in vacuum on strength of Ancorlam; (b) Change in mass and resistivity of Ancorlam after curing in vacuum furnace

Figure 36a shows that for densities in the range 6.8 – 7.2 g/cm^3, the strength of Ancorlam is greater after curing in the vacuum furnace than at standard atmospheric pressure. At the highest densitiy of 7.4 g/cm^3, the strength is similar after curing in a vacuum to at standard pressure. These results show that the beneficial effects on strength of curing in a vacuum observed in Section 4.4 carry over to coated iron powder compacted using lubricant up to a density of 7.2 g/cm^3. The gain in strength is however curtailed at the highest density of 7.4 g/cm^3 due to the closed pore network inhibiting the passage of gases in and out of the internal pores.

Figure 36b shows that there is an overall gain in mass at a density of 6.8 g/cm^3 as the mass gain by oxidation outweighs the mass loss due to lubricant burn out. There is a smaller loss in mass and a greater loss in resistivity in the samples cured in a vacuum in comparison to those cured at standard pressure in the range of densities between 7.0 – 7.2 g/cm^3 [Figure 31b]. At the highest density of 7.4 g/cm^3, the mass and resistivity losses are similar after curing in either a vacuum or standard furnace. These findings again provide a direct correlation between increased strength, decreased mass loss (or increased mass gain due to oxidation) and increased loss of resistivity all due to greater levels of thermal oxidation bonding.

Therefore, curing in a vacuum furnace increases the extent of oxidation bonding in comparison to curing at atmospheric pressure for Ancorlam samples up to a density of 7.2 g/cm^3. As shown in Section 4.4, the reduced oxygen partial pressure increases the rate of oxidation bonding at curing temperatures of 450°C. The addition of two sources of oxygen in the coating material and lubricant did not sufficiently increase the oxygen partial pressure to negate the increased oxidation rate.

4.5.2.4 Curing in Vacuum with Hydrogen

Curing in a vacuum with a flow of reducing gas such as 5% hydrogen in argon was shown to produce superior strength in A1000C samples pressed to low density without lubricant [Table 11]. This sub-section investigates whether this holds true for Ancorlam samples pressed to high density with lubricant, in order to reflect typical production conditions.

Ancorlam powder was pre-mixed with 0.4 wt% Kenolube and compacted into samples at four target densities in the range of 6.8 – 7.4 g/cm^3. Five samples of each target density were cured in a vacuum furnace at 450°C for 1 hour with a flow of 5% hydrogen in argon gas, and compared to those cured in a standard furnace for equal time and temperature (as detailed in Section 4.2). Figure 37a shows the comparative strength of Ancorlam powder compacts cured in a vacuum with 5% hydrogen and in a standard tube furnace at atmospheric pressure. Figure 37b shows the change in mass and resistivity of Ancorlam powder compacts cured in the vacuum furnace with a flow of 5% hydrogen over a range of densities.

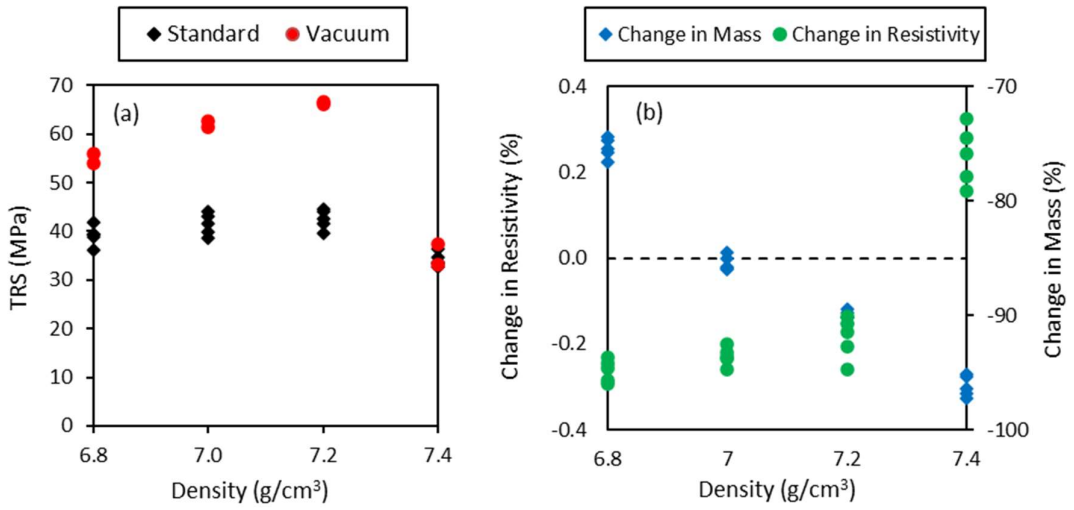

Figure 37: (a) Effect of curing in vacuum with flow of hydrogen on strength of Ancorlam; (b) Change in mass and resistivity of Ancorlam after curing in vacuum furnace with flow of hydrogen

Figure 37a shows that curing in a vacuum with a flow of hydrogen gas to provide a reducing atmosphere significantly increases strength compared to curing in a standard tube furnace, up to a density of 7.2 g/cm^3. Through comparison with Figure 36a, it is also clear that in this density range, curing in a vacuum with reducing atmosphere provides superior strength to curing in a vacuum with an inert atmosphere. This is due to the reduced oxygen partial pressure further increasing the oxidation rate in this temperature and pressure range. Strength is equal between the all furnace atmospheres at a density of 7.4 g/cm^3 as the closed pore network prevents the beneficial atmospheric conditions from reaching the core of the samples within the 1 hour curing duration. Figure 37b backs up these results, with a gain in mass at low density due to high levels of oxidation bonding, before curtailing at high density. This is further reflected in the resistivity, with a greater retention of resistivity at a density of 7.4 g/cm^3 due to reduced oxidation and residual lubricant being trapped in the pores of the samples.

These results show that curing in a vacuum with a flow of reducing hydrogen gas rather than inert nitrogen gas yields further increased strength in samples up to a density of 7.2 g/cm^3. The strength still remains inhibited at the highest density of 7.4 g/cm^3 due to the limited porosity preventing atmospheric gases from reaching the interior regions of the samples. This agrees with the conclusions of Section 4.2 stating that strength drops off at high density in Ancorlam samples due to inhibited thermal oxidation bonding. Therefore, this drop in strength at high density is a fundamental material problem and cannot be solved by changing the heat treatment parameters. In order to address this issue, a coarser particle size is recommended to allow for a more open pore network at the same density, as is utilised in Somaloy 700HR 5P powder [49].

4.6 Conclusion

In this chapter the strengthening mechanisms of current SMCs were investigated, focusing on commercially available Ancorlam powder produced by Hoeganaes corporation. It is reported in the literature that in some SMCs the coating material acts as a binder between particles to increase mechanical strength [79]. Alternatively, Pelletier et al. used resin impregnation to increase mechanical strength of SMC materials [162]. However, in this chapter it is concluded that the primary strengthening mechanism of Ancorlam powder (and other SMCs utilising phosphate coatings) is the formation of an oxide scale between the individual particles, known as thermal oxidation bonding. Coated iron powder was found to have a lower strength than uncoated iron powder at all densities measured [Figure 29]. Therefore, rather than acting as a binder material, the addition of the coating material was found to actually reduce strength by inhibiting the thermal oxidation bonding process.

The strength of cured Ancorlam powder was found to decrease at high density, contrary to the initial hypothesis. This is problematic as magnetic properties such as permeability and saturation magnetisation improve with increasing density [7] [19] and therefore a compromise between mechanical and magnetic properties must be made. In contrast to Ancorlam, the strength of Somaloy 700HR 5P increased with density up to the maximum density measured of 7.4 g/cm^3, in agreement with the initial hypothesis. This was concluded to be due to the coarser particle size of Somaloy resulting in larger pores in the compacted samples. In Ancorlam samples compacted to very high density, the build up of oxide scale blocks the smaller pores and prevents the passage of oxygen into the interior region of the sample, limiting the oxidation bonding process.

In order to mimic the coarser particle size of Somaloy, a batch of Ancorlam powder was produced with the finer particles removed. This method of increasing the average particle size lessened the drop off in strength at high density but did not fully resolve the issue [Figure 27]. The maximum particle size of the A1000C base powder used to make Ancorlam is 250 μm, equal to the average particle size of Somaloy, which utilises particles up to 425 μm [123] [49]. Therefore, it is not possible to create a mix of Ancorlam powder with the same average particle size as Somaloy using the standard Ancorlam composition. Whilst not possible to prove experimentally with standard Ancorlam powder, it is hypothesised that the use of sufficiently large particles would indeed prevent the drop in strength at 7.4 g/cm^3.

In order to further understand the thermal oxidation bonding process, the mass gain due to oxidation was quantified using TGA analysis. Uncoated iron powder (A1000C) was found to experience a greater increase in mass than coated iron powder (Ancorlam) at equivalent density. This demonstrates a

greater extent of thermal oxidation bonding, or rather confirms that the addition of the phosphate coating inhibits the oxidation process.

The thermal oxidation bonding process comes at a cost of reducing the resistivity due to the formation of conductive layers between the iron particles. Combined with the decomposition of the lubricant, the resistivity decreases by an order of magnitude from the green to the cured state. Consequently, there is a large drop in resistivity for a relatively small gain in mechanical strength. The possiblility of controlling the thermal oxidation bonding process was investigated by reducing the available oxygen, with the aim of achieving a balance of strength and resistivity to suit the application. Five sources of oxygen were idenfied; oxygen in the atmosphere, oxygen in the lubricant, oxygen in the coating, oxygen impurities in the iron powder and surface oxides on the iron powder. The first three of these sources were removed in turn but not even their combined absence resulted in any significant reduction in the levels of thermal oxidation bonding. The oxygen partial pressure of the vacuum with reducing atmosphere was still many orders of magnitude too high to prevent oxidation of the iron powder.

Contrary to the initial hypothesis, curing in a vacuum to reduce the available oxygen in the furnace atmosphere did not inhibit the strength of Ancorlam powder, but rather increase it. At the temperature and pressure range of the curing process, decreasing the oxygen partial pressure actually increases the oxidation rate [158] [159]. In addition, the vacuum furnace also assists the flow of gases into and out of the pores of the sample, aiding the thermal oxidation bonding process further.

Methods of further increasing the rate of oxidation through the use of a vacuum furnace and alternate atmospheres were investigated alongside the effects of increasing curing time and temperature. The rate of oxidation and corresponding strength was found to increase by curing in a vacuum for samples with a density up to 7.2 g/cm^3. However, this increase in oxidation rate and strength did not translate to the highest density measured of 7.4 g/cm^3. It was again concluded that at this density, the pore network becomes closed due to the build up of oxide scale, and therefore oxygen is unable to travel into the core of the sample and contribute towards the bonding process.

Curing in a vacuum with a flow of hydrogen acting as a reducing gas rather than nitrogen resulted in even greater levels of oxidation and strength gain for Ancorlam samples with a density up to 7.2 g/cm^3. The reducing gas decreases the oxygen partial pressure, further increasing the oxidation rate at the curing temperature and pressure. However, as was the case with curing in a vacuum with a flow of nitrogen, this increase in oxidation rate and strength did not translate to the highest density measured of 7.4 g/cm^3. This further confirms that the pore network becomes closed at a density of 7.4 g/cm^3, as

this positive increase in strength due to an alternative atmoosphere only occurs in samples with sufficient porosity.

Increasing curing time from 1 hour to 24 hours yielded an increase in the strength of Ancorlam powder at all densities. This demonstrates that the oxidation process is not complete after curing for one hour and therefore full strength is not yet achieved. Increasing curing temperature from 450°C to 600°C also yielded a slight increase in strength at all densities measured, demonstrating that the rate of oxidation of Ancorlam powder increases with temperature.

The thermal oxidation bonding process that is responsible for providing mechanical strength in Ancorlam powder is detrimental to magnetic properties. The formation of oxide contacts between the particles reduces the resistivity of the cured sample. Furthermore, the oxidation process is inhibited at a density of 7.4 g/cm^3 ; the density at which magnetic properties are also optimal. Therefore an alternative strengthening mechanism is sought. Many SMCs utilise a coating system which acts as a "binder" material between the particles, fusing together during the annealing process [79]. For example, Gelinas et al. developed an iron-resin composite material in which the resin is activated during the heat treatment process and provides mechanical strength [152].

Chapter 5 shall focus on the development of a new coating system with binding properties to be applied onto the A1000C base iron powder. Novel SMC materials utilising this coating system shall be produced with the aim of possessing improved mechanical and magnetic properties over commercially available Ancorlam powder.

5 Glass-Based Hybrid Coatings

5.1 Introduction

In this chapter, the use of soluble silicates as a binder to adhere coating materials onto the iron powder is investigated. Soluble silicates possess the additional benefit of being resistive themselves and thus act as a potential coating material on their own.

The use of soluble silicates as part of a hybrid coating system is a relatively new concept and therefore has limited coverage in the literature. In 2019, Tontini et al. published a paper describing the use of soluble silicates to coat alumina nanoparticles onto the surface of iron powder [147]. However, this paper achieved relatively low compacted densities (6.9 - 7.1 g/cm^3) and thus poor permeability and did not consider mechanical properties. Furthermore, magnetic properties were only measured at 10 and 60 Hz, at which eddy current losses are negligible [Section 2.1.10]. Samples can be heat treated at higher temperatures to fully stress relieve the base iron powder, improving coercivity at a cost of resistivity. At low frequency, core loss will be small due to decreased hysteresis losses, even if the coating fully degrades. Therefore, in order to assess the performance of a coating material, core loss should be measured at frequencies up to and including 1000 Hz. At higher frequency, eddy current losses are significant, and thus the ability of the coating system to contain eddy currents within individual iron particles can be assessed.

This chapter builds upon the concept of dispersing a coating material within the liquid glass, by selecting appropriate combinations of coating materials and particle size ranges, and analysing magnetic performance over the 50 – 1000 Hz frequency range. Furthermore, this chapter also provides an analysis of the mechanical properties of this new class of SMC materials. Both magnetic and mechanical properties are compared to those of commercially available SMCs.

Soluble silicates, also known as “liquid glass” or “water glass” are comprised of alkali metal oxides and silica in varying proportions. They do not follow a distinct stoichiometric chemistry and hence cannot be assigned a specific chemical formula or molecular weight. The general formula for soluble silicates is given in Equation 4.1 [163].

$$M_2O \cdot n\,SiO_2 \qquad (4.1)$$

Where *M* is an alkali metal oxide such as sodium, potassium or lithium, and *n* is the molar ratio defining the number of moles of silica per mole of alkali metal oxide.

An important factor in the practical use of soluble silicates is the weight ratio, *WR* of alkali metal oxides to silica. The weight ratio, *WR* is given by Equation 4.2.

$$WR = n * M_{\mathrm{SD}} / \ M_{\mathrm{MO}} \quad (4.2)$$

Where *n* is the molar ratio, M_{SD} is the molar mass of silicon dioxide, and M_{MO} is the molar mass of the alkali metal oxide.

For the example of sodium silicates, the molar mass of silicon dioxide is 60.08 g/mol and the molar mass of sodium oxide is 61.98 g/mol, hence the weight ratio is given by Equation 4.3.

$$WR_{\mathrm{Sodium\ Silicates}} = n * 60.08 \ / \ 61.98 \quad (4.3)$$

The weight ratio determines the characteristics and properties of the soluble silicate. Alkali metal silicates are alkaline substances with pH values typically in the range 10 - 13 [164]. As the weight ratio, *WR* is increased the alkalinity decreases, making the silicates less hazardous but also less soluble [165]. The viscocity of a silicate is a function of the molar ratio, the concentration of solids, and temperature. Viscosity increases with increasing molar ratio and concentration of solids, whilst it decreases with increasing temperature [166] [167]. Therefore, as molar ratio, *n* is increased, the silicate becomes both less soluble and more viscous. Consequently, this has a negative affect on the ability of the silicate to form a thin, uniform coating on a substrate material via wet chemical methods.

Silicates have good emulsifying and suspending properties, hence are useful for dispersing fine particles [164]. In addition, silicates are used for surface modification and metal-binding, making them ideal candidates for coating the surface of the iron powder. The reaction between soluble silicates and polyvalent metals such as iron results in amorphous silica being formed, which is highly resistive. Furthermore, sodium silicate is easy to handle, non-toxic, inflammable and enviornmentally friendly [168]. This research shall focus on sodium silicates as they are significantly more economically viable than lithium and potassium silicates.

5.2 Ferrite-Glass Coatings

Soft ferrite materials were selected for investigation as a coating material to be dispersed within the liquid glass due to their high resistivity and thermal stablilty [Section 2.3.4]. They also have the distinct advantage of being ferrimagnetic, thus retaining a greater magnetic volume in the bulk SMC material. There are two classes of soft ferrites which have received increasing research interest as a coating material, namely manganese-zinc ferrites and nickel-zinc ferrites [100] [104] [101] [105]. MnZn-ferrites have higher permeability and saturation magnetisation whilst NiZn-ferrites possess higher resistivity [70] [71] [72] [73]. As this research focuses on SMCs for use at low to medium frequencies in the range of 50 - 1000 Hz, high permeability and saturation magnetisation are prioritised, hence this chapter focuses on the use of manganese based ferrites.

Several processing methods have been employed in the literature to produce ferrites including co-precipitation [169] [170], sol-gel auto combustion [101] [105] [171] and solid state diffusion [100] [172]. Whilst it is important to understand ferrite production methods, the novel aspect of this research will focus mainly on the challenges of coating these materials onto iron powder. As previously discussed in Section 2.3.4, ferrites are often synthesised as nanoparticles which tend to agglomerate and hence it is difficult to form a thin, uniform coating on the core powder [107]. Furthermore, ferrites are brittle and do not compact well, hence the coating can shear during compaction if not well bonded to the core powder [106]. Both of these factors contribute to the relatively high porosity and low density of final SMC compacts, resulting in reduced permeability and saturation magnetisation.

Methods for coating soft ferrites onto core powder include dry mixing methods such as ball milling [31] and acoustic mixing [39] and wet chemical methods such as dispersion in solvent [100] or dispersion in binder [103]. Recently, more novel methods such as microwave annealing [104] and spark plasma sintering [102] have been used to coat ferrites onto ferromagnetic core powder. These novel methods require expensive specialist equipment and are therefore not suitable for large industrial scale production, so this research will focus on dry mixing and wet chemical methods.

Dry coating processes are very simple, inexpensive and require minimal additions of lubricant thus reducing impurities in the final compact. However, these methods rely on Van der Walls interactions and static forces hence the ferrite is not chemically bonded to the core powder, giving issues during compaction and resulting in low density of final compacts. Wet chemical methods typically give better adhesion to the surface of the core powder, but suffer from large agglomerates of the ferrite particles. This makes it difficult to achieve a thin, uniform layer on the core powder, reducing the surface coverage and requiring a greater amount of ferrite material to produce an effective coating. Therefore, a key challenge with ferrite coated SMCs is to improve the relatively low densities of the final compacts through better dispersion of ferrite nanoparticles or improved bonding to the core powder.

5.2.1 Methodology and Procedure

As-received Ancorsteel 1000C powder from GKN Hoeganaes Corporation was used as the core powder as justified in Section 3.1.1. Manganese ferrite nanopowder from Powertech International with an average particle size of 1 µm was used as the coating material, with sodium silicate solutions from VWR International and Diatom both tested as the coating agent. Key data for all coating materials is given in Section 3.1.3.

The sodium silicate solution was diluted in distilled water and stirred continuously for ten minutes. Ferrite powder was added to the solution and dispersed for a further ten minutes using ultrasonic

treatment. The A1000C iron powder was added stepwise into the previously prepared solution whilst stirring continuously. The mixture was dried for three hours at 90℃ on a hot plate and the dry powder was washed three times in deionised water to remove impurities. A lubricant addition of 0.4 wt% Kenolube was mixed into the coated powder prior to uniaxial cold compaction at a pressure of 800 MPa. Toroidal samples with outer diameter 36 mm, inner diameter 22 mm and height 6 mm and bar samples with length 30 mm, width 12 mm and height 6 mm were produced. These samples were heat treated at 400 - 550℃ for one hour in a nitrogen atmosphere to reduce the internal stresses caused by compaction.

After heat treatment, cured density was measured for all samples. Toroidal samples were wrapped with 100 windings on the primary coil and 40 windings on the secondary coil in order to measure AC hysteresis loops at B = 1 T at a frequency range of 50 – 1000 Hz as detailed in Section 3.2.2. Bar samples were used to measure resistivity using the four point probe method before measuring TRS via the three point bend test. Fracture surfaces of the broken samples were polished and etched for examination of the microstructure under SEM with EDX capability to understand coating thickness and uniformity.

5.2.2 Results

Initial ferrite-glass coating trials were conducted using manganese ferrite powder from Powertech International and sodium silicate technical solution from VWR. The properties of these two coating materials are given in Section 3.1.3. The liquid glass has silicon dioxide to sodium oxide ratio greater than 3, which is considered relatively high. This initial glass shall be referred to as “glass A”. The consituents amounts of ferrite and glass for initial trials were selected to be 0.5 wt% ferrite and 0.4 wt% glass.

These initial amounts were calculated from the specific surface coverage of the respective materials. The manganese ferrite has a specific surface area of 4.9 m^2/g. The specific surface area of the A1000C iron powder is estimated from measurements by F. Sanchez et al. using a very similar irregularly shaped iron powder produced by the same water atomisation process [173]. Theoretical predictions indicate a specific surface areas of 0.0042 - 0.0234 m^2/g, whilst experimental measurements indicate a specific surface area of 0.055 - 0.287 m^2/g. Whilst these measurements give a very large range of possible values, for a 200g batch of iron powder, the total surface area is predicted as 0.84 - 4.68 m^2 and 10 - 60 m^2 for theoretical predictions and experiemental measurements respectively. Therefore, a total coating surface area in the region of 5 - 10 m^2 was chosen as a middle-ground estimate for initial trials. From this, a coating amount of 1g ferrite was selected, or 4.9 m^2 surface area, taking into account the liquid glass would add to the total surface area of the coating. For a 200g iron powder

batch, this gives 0.5 wt% ferrite for use in initial trials. The amount of glass to be used was taken as 0.4 wt%, to be equal to the standard amount of lubricant used in preparation of SMC samples. The liquid glass operates in a similar manner to the lubricant in that it aims to achieve good surface coverage between all of the iron particles, and thus the same amount was used as a starting point for initial trials.

In order to determine the state of the coating on the iron particles, the microstructure was examined. Figure 38 presents SEM and EDX images of a polished fracture surface of the ferrite-glass coated samples.

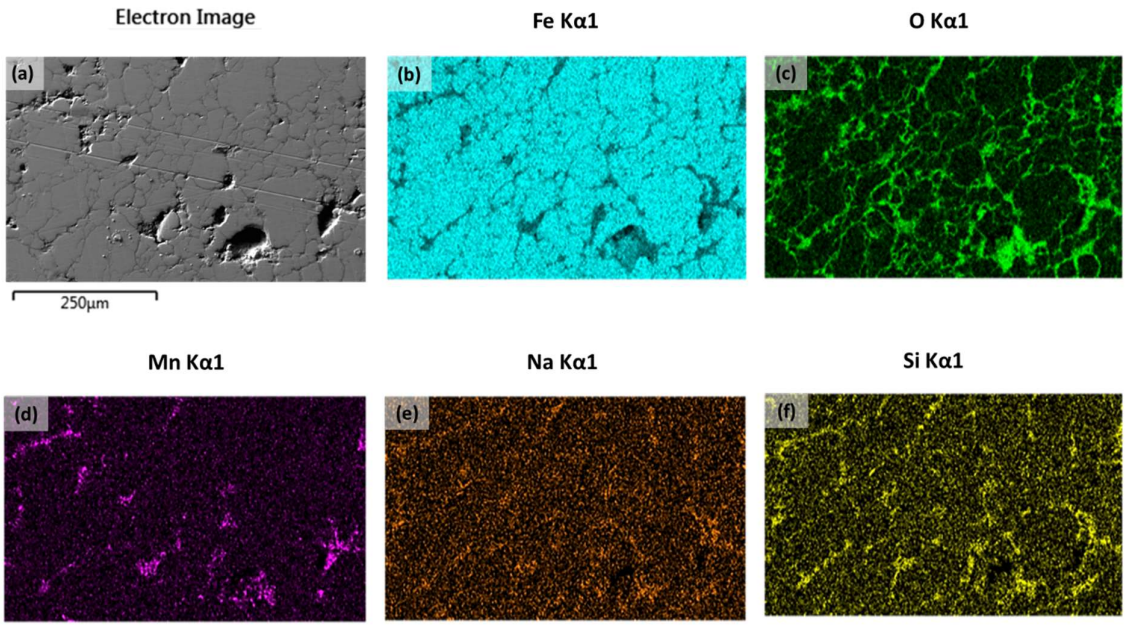

Figure 38: SEM and EDX images of polished fracture surface of ferrite-glass coated samples

Figure 38 illustrates a distribution of the elements manganese, oxygen, sodium and silicon in the pores between the iron particles. The presence of these elements shows that a coating containing sodium silicate (SiO_2 – Na_2O) and manganese-ferrite coating formed successfully on the surface of the individual iron particles. The greater concentration of silicon over sodium is expected due to the liquid glass possessing a silicon oxide to sodium oxide ratio greater than 3. There is also a larger concentration of oxygen than the other coatings materials due to oxides formed during the thermal oxidation bonding process.

Having determined that the iron particles were successfully coated with a ferrite-glass layer, magnetic characterisation was performed in order to measure magnetic properties. Figure 39 presents comparative AC hysteresis loops for an induction of 1 T over a frequency range of 50 to 1000 Hz for uncoated A1000C iron powder and the ferrite-glass coated iron powder. Both samples were mixed

with 0.4 wt% Kenolube before being compacted under a pressure of 800 MPa and subsequently heat treated for one hour at 450°C in a nitrogen atmosphere. The corresponding values of core loss for each sample are presented in Table 12 alongside other key magnetic and mechanical properties.

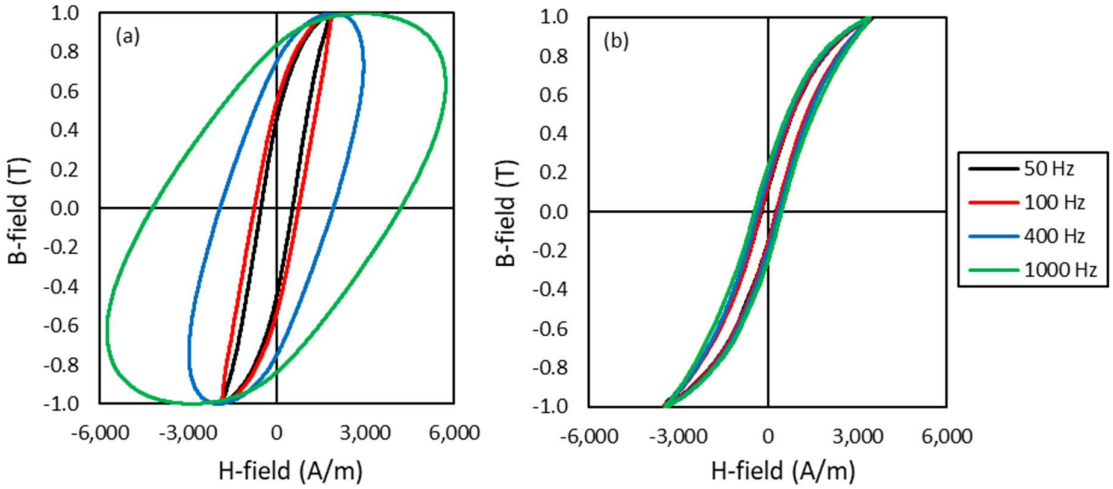

Figure 39: AC hysteresis loops for (a) uncoated iron powder; (b) 0.5 wt% ferrite, 0.4 wt% glass A coated iron powder

Composition	Density (g/cm^3)	TRS (MPa)	Resistivity (mΩcm)	H @ 1 T (A/m)	Core Loss @ 1 T (W/kg)		
					50 Hz	400 Hz	1 kHz
A1000C Control	7.40	55.11	0.19	1803	11.9	347.9	1875.9
A1000C + 0.5% ferrite + 0.4% glass A	7.29	49.61	8.68	3487	6.3	68.1	223.7
Difference (%)	-	-9.98%	4468.42%	93.40%	-47.06%	-80.43%	-88.08%

Table 12: Key properties of uncoated and ferrite-glass coated samples

Figure 39a illustrates the increase in coercivity of the uncoated iron sample by the broadening of the hysteresis loop as frequency is increased from 50 Hz to 1000 Hz. At frequencies of 400 Hz and above, the hysteresis loop for the pure iron sample becomes elliptical in shape, due to the lack of insulation between particles resulting in large eddy current contributions. Eddy current losses are proportional to the square of frequency, whilst hysteresis losses are linearly proportional to frequency, hence eddy current losses become dominant at higher frequencies [Section 2.1.8]. On the contrary, Figure 43b shows considerably less broadening of the hysteresis loop with increasing frequency, illustrating the ferrite-glass coating is providing an effective insulation layer between the iron particles. This insulating layer contains the eddy currents within the individual iron particles, and thus at high frequencies eddy current losses remain relatively low in comparison to the uncoated iron sample.

Table 12 shows numerically why the addition of a ferrite-glass coating onto the iron powder prevents the broadening of the hysteresis loop. The ferrite-glass coating increases resistivity by more than an order of magnitude over the uncoated iron powder sample, greatly reducing core loss at higher frequencies. The required H-field to reach an induction of 1 T, characterised as "H @ 1 T", is greater in the ferrite-glass coated sample than the uncoated iron sample. This metric can be used as an indication of the permeability of the samples, with the smaller applied field indicating better permeability as discussed in Section 3.2.2. This difference in permeability can also be observed by the gradient of the hysteresis curve, which is noteably steeper at 50 Hz for the uncoated iron than the ferrite-glass coated sample. This difference in permability Is due to the addition of a non-magnetic coating, which reduces the magnetic volume of the sample. This result is as expected and is a feature of all soft magnetic composite materials, hence we must minimise the amount of coating material whilst ensuring sufficient resistivity is retained.

Transverse rupture strength is slightly lower in the ferrite-glass coated sample than the uncoated iron control sample. This is because the addition of the coating material inhibits the thermal oxidation bonding process between iron particles [Figure 29]. However, the glass acts as a binder material and therefore helps to curtail this reduction in strength. With both magnetic and mechanical properties influenced in different directions by the amount of coating material, it is important to optimise the amount of each constituent material to find the best compromise between each of these properties.

The results from the initial trials of the ferrite-glass coating show potential. However, higher permeability and lower core loss are required to compete with the best commercially available SMCs introduced in Section 2.3.1. In order to address this an alternative liquid glass, commercially available Diatom R2447, was selected for secondary trials. This second glass shall be referred to as "glass B". Glass B has a lower weight ratio and thus lower viscosity and higher solubility than glass A. It was hypothesised that these attributes will improve the ability of the glass to form an evenly distributed coating layer over each of the iron particles. This would in effect improve the surface coverage for a given amount of coating material, or reduce the required amount of coating material for a given surface coverage, leading to better compaction behavior and ultimately increased density and permeability. Furthermore, glass B has a higher concentration of solids and therefore greater resistivity than glass A, helping to improve core loss at higher frequencies.

Figure 40 displays AC hysteresis loops for ferrite-glass samples using glass A and glass B in order to provide a comparison between the two types of liquid glass. Both samples contain 0.5 wt% ferrite and 0.4 wt% glass. Table 13 shows the corresponding magnetic and mechanical properties of the samples.

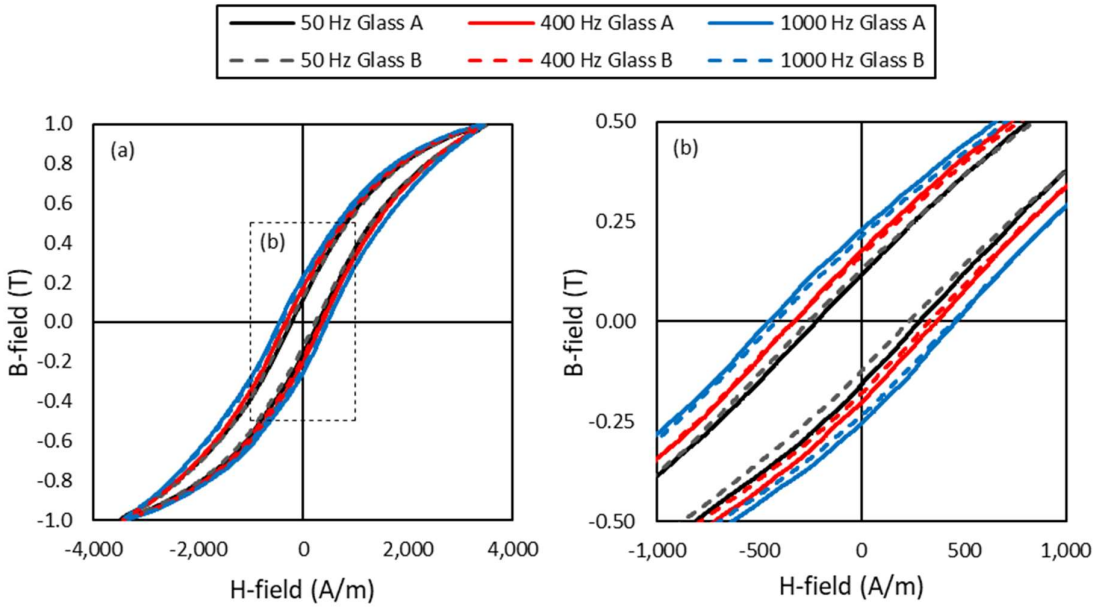

Figure 40: (a) AC hysteresis loop comparison of glass A and glass B in ferrite-glass coated samples; (b) zoomed in view

Composition	Density (g/cm^3)	TRS (MPa)	Resistivity (mΩcm)	H @ 1 T (A/m)	Core Loss @ 1 T (W/kg)		
					50 Hz	400 Hz	1 kHz
A1000C + 0.5% ferrite + 0.4% glass A	7.28	49.61	5.51	3487	6.3	68.1	223.7
A1000C + 0.5% ferrite + 0.4% glass B	7.31	64.04	6.02	3445	5.8	62.1	208.0
Difference (%)	-	**29.09%**	**9.26%**	**-1.20%**	**-7.94%**	**-8.81%**	**-7.02%**

Table 13: Comparison of glass A and glass B in ferrite-glass coated samples

Figure 40 shows that the sample using glass B has a marginally thinner hysteresis loop than that using glass A. The dashed lines of the glass B sample are closer together than the solid lines of the glass A sample, indicating lower coercivity. This is further reflected in Table 13, where the glass B sample has reduced core loss at 50 Hz, due to lower coercivity limiting hysteresis losses, which are dominant at this frequency. Table 13 shows that the glass B sample has greater density and permeability (due to having a lower required H-field for an induction of 1 T) than the glass A sample, indicating that glass B does indeed provide better surface coverage than glass A. The improvement in density results in less void space, and hence lower coercivity and hysteresis losses. Coupled with an improvement in resistivity contributing to reduced eddy current losses, the use of glass B over glass A results in lower overall core losses at all frequencies. Furthermore, the glass B sample shows improved strength over the glass A sample, owing partly to the increased density, but also to the

improved surface coverage, resulting in a more evenly distributed layer of glass binder over each of the iron particles.

Glass B demonstrates an improvement over glass A in all properties measured. However, this improvement is relatively small and therefore optimisation of other processing parameters was carried out. The heat treatment temperature was varied for a batch of 0.5 wt% ferrite, 0.4 wt% glass B samples to find the temperature at which core loss is minimised. As curing temperature is increased, there is more complete annealing of the base iron powder, reducing coercivity and hysteresis losses. However, increased temperature degrades the ferrite-glass coating thus reducing resistivity and increasing eddy current losses.

Figure 41 contains AC hysteresis loops at a frequency of 1000 Hz for toroidal samples of ferrite-glass coated iron powder cured at 400 - 500°C. The mechanical and electrical properties measured from rectangular bar samples of the same ferrite-glass coated powder produced in parallel and subject to the same heat treatment conditions are given in Table 14.

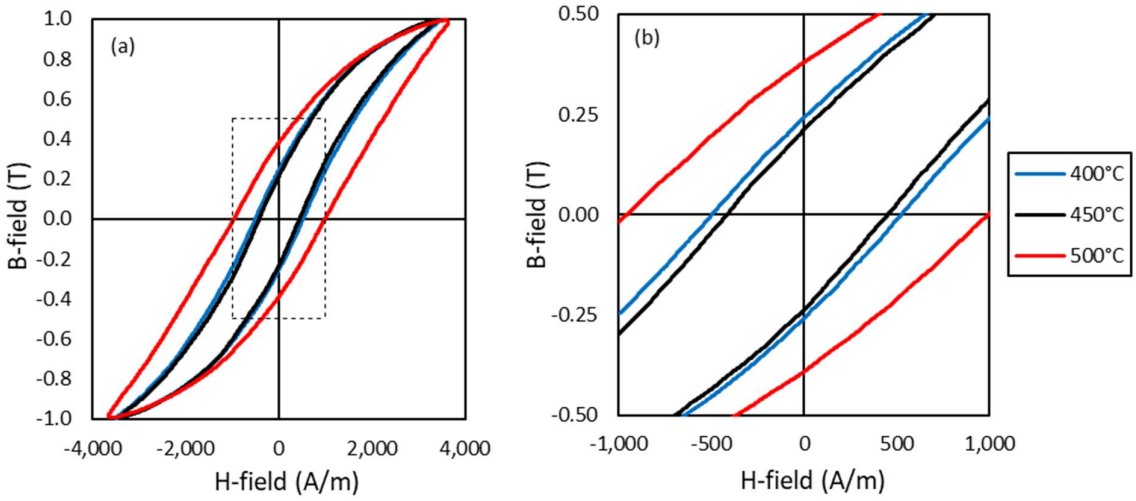

Figure 41: (a) AC hysteresis loop comparison for ferrite-glass coated samples cured at different temperatures; (b) zoomed in view

Curing Temperature (°C)	Density (g/cm^3)	TRS (MPa)	Resistivity (mΩcm)
400	7.32	59.62	7.52
450	7.31	64.04	6.02
500	7.30	68.81	1.81

Table 14: Effects of curing temperature on properties of ferrite-glass coated samples

Figure 41 shows that as curing temperature is increased from 400°C to 450°C, the hysteresis loop narrows slightly, illustrating an improvement in coercivity as further stress relief of the iron is achieved. Table 14 shows that an improvement in strength also occurs as curing temperature is increased from 400°C to 450°C, as a result of further thermal oxidation bonding. However, this comes at a cost to resistivity due to the increased formation of less resistive oxide layers between the iron particles [Section 2.3.6]. However, the improvements in coercivity outweigh the deleterious effects of the reduced resistivity, resulting in an overall reduction in core loss. However, at a curing temperature of 500°C the ferrite-glass coating breaks down, resulting in iron-on-iron contact and significantly reduced resisitivity, leading to increased eddy current losses. The permeability is also reduced, as evidenced by the reduced gradient of the hysteresis loop at 500°C in comparison to 450°C. This combination of increased eddy current losses and decreased permeability both result in significantly increased core losses, particularly at high frequency. This is illustrated in Figure 41 by significant broadening of the hysteresis loop. These results are in agreement with Wu et al. who found that the manganese-ferrite based coating decomposed after increasing curing temperature from 400°C to 500°C [105]. A curing temperature of 450°C is selected for further investigation of ferrite-glass coated iron powder samples as this is the temperature at which core losses are minimised.

In order to find the optimal composition of the ferrite-glass coating, the amount of each constituent material was varied to find which combination had the minimum core loss at 1000 Hz. The amount of ferrite addition was varied from 0.2 wt% to 0.6 wt% in 0.1 wt% increments, whilst keeping the amount of liquid glass constant at 0.4 wt%. The amount of glass was then varied from 0.3 wt% to 0.5 wt% also in 0.1 wt% increments whilst keeping the amount of ferrite constant at 0.5 wt%. Figure 42 and Figure 43 show resistivity, H @ 1 T, core loss at 1000 Hz, and TRS against wt% ferrite and wt% glass additions respectively.

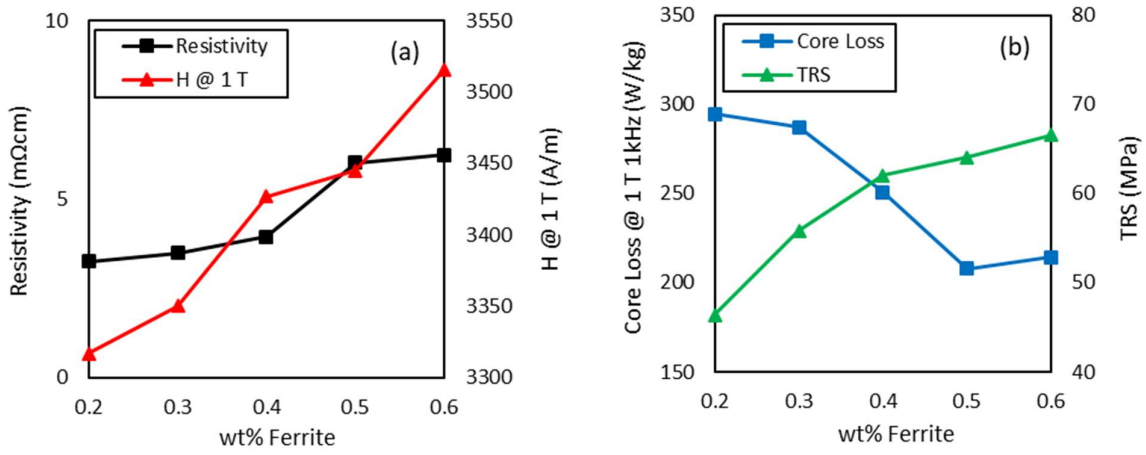

Figure 42: (a) Resistivity and H @ 1 T against wt% ferrite; (b) core loss and TRS against wt% ferrite for ferrite-glass coated samples

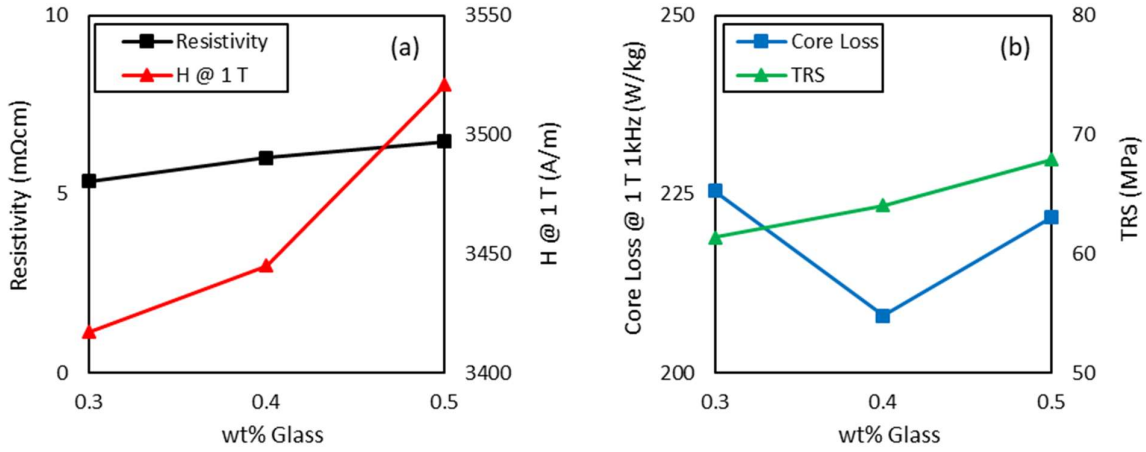

Figure 43: (a) Resistivity and H @ 1 T against wt% glass; (b) core Loss and TRS against wt% glass for ferrite-glass coated samples

Figure 42 shows that as the percentage of ferrite inclusion increases, H @ 1 T increases due to the decreased magnetic volume and decreased density. Even though ferrite is ferrimagnetic, it is less magnetic than the ferromagnetic iron powder it replaces, hence overall magnetisation reduces. Mechanical strength also increases with increasing ferrite inclusion, as the dispersion of additional ferrite within the liquid glass increases the thermal stability of the coating, which then remains intact after the heat treatment process and acts as a binder between iron particles. Resisitivity increases with increasing wt% ferrite due to the additional coating material. Core loss is minimised at 0.5 wt% ferrite, where there is a balance between the increased resistivity and decreased permeability due to the inclusion of additional coating material.

Figure 43 shows a similar trend of increasing H @ 1 T with increasing wt% of glass as observed for ferrite, due to the addition of non-magnetic material. Strength also increases with wt% of glass due to the liquid glass acting as a binder material. Resistivity increases with wt% of glass, but by smaller increments in comparison to the wt% of ferrite, as the glass contributes less to the overall resisitivty than ferrite. Meanwhile, core loss is dependent on the balance of resistivity and permeability which influence core loss in opposing directions. The optimum amount of glass inclusion to minimise core loss was found to be 0.4 wt% glass.

In order to better understand the ferrite-glass coating system, the individual contributions of the glass and ferrite to the properties of the overall composite material were tested. Samples were prepared with ferrite-only coating and with glass-only coating. Samples of iron with ferrite-only had extremely low density as the ferrite material did not adhere well to the iron without the inclusion of the glass binder. Consequently, these samples had very poor compaction behaviour, breaking upon ejection from the die and thus adequate testing of properties was not possible.

Table 15 presents the key magnetic properties of iron with glass-only coating and a control sample of iron with ferrite-glass coating for comparison. All samples were mixed with 0.4 wt% Kenolube, pressed at 800 MPa and subsequently heat treated at 450°C for one hour in a nitrogen atmosphere.

Composition	**Density (g/cm^3)**	**TRS (MPa)**	**Resistivity (mΩcm)**	**H @ 1 T (A/m)**	**Core Loss @ 1 T (W/kg)**		
					50 Hz	**400 Hz**	**1 kHz**
A1000C + 0.5% ferrite + 0.4% glass B	7.31	64.04	6.02	3445	5.8	62.1	208.0
A1000C + 0.4% glass B	7.33	44.89	3.39	2931	6.2	71.6	256.3
Difference (%)	-	**-29.90%**	**-43.69%**	**-14.92%**	**6.90%**	**15.30%**	**23.22%**

Table 15: Key magnetic and mechanical properties of glass-only coated samples

Table 15 shows that the glass-only coating serves to reduce core loss versus pure uncoated iron powder (see “A1000C control” sample in Table 12) by acting as a resistive layer between the iron particles. The removal of ferrite from the glass improves permeability, evidenced by a smaller H-field required to reach 1 T, due to the increased magnetic volume and density. The ferromagnetic iron powder which replaces the ferrimagnetic ferrite in a glass-only sample is more magnetic, hence overall magnetisation increases. However, this increase in permeability is outweighed by a significant decrease in resistivity, resulting in an overall increase in core loss at all frequencies measured. The percentage difference in core loss between glass-only and ferrite-glass coated iron increases with frequency, demonstrating that the reduced resistivity due to the exclusion of ferrite results in higher eddy current losses. Furthermore, the exclusion of ferrite decreases mechanical strength after curing.

In ferrite-glass samples, the dispersion of ferrite within the liquid glass increases the thermal stability of the coating, which then remains intact after the heat treatment process and acts as a binder between iron particles. Without bolstering the thermal stability, the glass-only coating degrades during curing, decreasing the binding effect and the mechanical strength of the overall composite. Therefore, it is concluded that the combination of both ferrite and glass together as a hybrid coating is superior to either of the constituent materials as a standalone coating.

Having completed some basic optimisation of the ferrite-glass coatings a comparison is made with other ferrite-based coatings in the literature. K. J. Sunday used acoustic mixing to coat NiZnCu-ferrite onto iron powder [174]. This is a particularly valid comparison as K. J. Sunday used the same A1000C base iron powder from Hoeganaes Corporation as in this research, and therefore provides a direct comparison of the coating system. Table 16 presents a comparison of these ferrite-based samples in the literature to the ferrite-glass coated samples produced.

Composition	**Curing Temp (°C)**	**Density (g/cm^3)**	**TRS (MPa)**	**H @ 1 T (A/m)**	**Core Loss @ 1 T (W/kg)**		
					50 Hz	**400 Hz**	**1 kHz**
5% ferrite coating	700	7.31	84.3	> 8000	12	298	1238
A1000C + 0.5% ferrite + 0.4% glass B	450	7.31	64.04	3445	5.8	62.1	208.0
Difference (%)	-	-	**-24.03%**	**-56.94%**	**-51.67%**	**-79.16%**	**-83.20%**

Table 16: Comparison of ferrite-glass coated samples with literature values

Table 16 shows that the ferrite-glass samples produced required less than half the applied field to reach an induction of 1 T, demonstrating a permeability more than double that of the ferrite coated samples in the literature. Furthermore, core loss is less than half of the ferrite coated samples at 50 Hz, scaling to one sixth at 1000 Hz. A directly comparable measurement of resistivity is not provided, however from examination of the core loss data, it is clear that resisitivity is significantly superior in the ferrite-glass coated sample. The one limiting factor is the ferrite coated samples produced in the literature have greater mechanical strength than the ferrite-glass coated samples. However, this is a direct consequence of the significantly increased curing temperature from 450°C to 700°C. This shortfall could be made up by simply curing at a higher temperature or using a larger addition of liquid-glass, both of which would come at a cost to the magnetic properties.

To prove the former, samples of iron coated with 5 wt% in-house synthesised NiZn-ferrite were produced and cured at high temperatures. These samples were pressed at 800 MPa and cured at

various temperatures between 300 - 900°C in a nitrogen atmosphere. Figure 44 shows the relationship between strength and curing temperature.

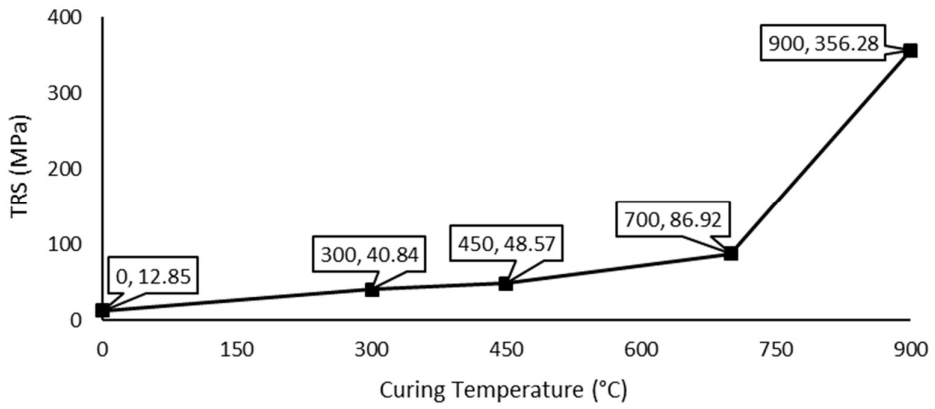

Figure 44: Strength of ferrite coated iron samples against curing temperature

Figure 44 shows that strength increases with curing temperature due to increased thermal oxidation bonding. As temperature is increased to 900°C, the onset of sintering occurs, resulting in a large improvement in strength. The 5 wt% ferrite coated sample has a strength of 86.9 MPa, demonstrating close agreement with the literature value of 84.3 MPa listed in Table 16.

However, we must compare to commercially available SMCs such as Ancorlam to provide a further benchmark for performance. Ancorlam is produced by Hoeganaes corporation and uses the same A1000C base iron powder as in this research, so is a reliable indicator of coating performance. Table 17 provides a comparison of magnetic and mechanical properties between the optimised ferrite-glass coated sample and Ancorlam produced under the same conditions.

Composition	**Density (g/cm^3)**	**TRS (MPa)**	**Resistivity (mΩcm)**	**H @ 1 T (A/m)**	**Core Loss @ 1 T (W/kg)**		
					50 Hz	**400 Hz**	**1 kHz**
Ancorlam Control	7.33	37.90	8.92	3043	6.4	57.6	174.3
A1000C + 0.5% ferrite + 0.4% glass B	7.31	64.04	6.02	3445	5.8	62.1	208.0
Difference (%)	-	**68.97%**	**-32.51%**	**13.21%**	**-9.38%**	**7.81%**	**19.33%**

Table 17: Comparison of Ancorlam and ferrite-glass coated samples

Table 17 shows that the liquid glass coated sample provides better mechanical strength than Ancorlam, owing to the binding properties of the liquid glass. Furthermore, core loss at 50 Hz is improved due to lower coercivity. However, the applied field to reach an induction of 1 T is greater due to having more coating material which decreases magnetic volume. Furthermore, the ferrite-glass coating is less resistive than the Ancorlam coating, resulting in higher core loss at and above 400 Hz.

The ferrite-glass coating provides a good start, with some properties improved at a cost to others. It could be used in applications operating at 50 Hz, and for those where higher strength is required than currently offered by Ancorlam.

5.3 Metal oxide-Glass coatings

Samples of iron powder with ferrite-glass coating showed vastly improved magnetic properties over uncoated iron powder, and were able to compete when benchmarked against commercially available SMCs, demonstrating some improved properties. However, for a clear improvement, the core loss at high frequency must be reduced which requires increased resistivity. The concept of using liquid glass to disperse a coating material shows potential, and as such the use of nanoparticle metal oxides in place of ferrite was investigated to bolster the resistivity.

Metal oxides are a promising candidate coating material due to their high electrical resistivity and thermal stability. Aluminium oxide (alumina) can withstand very high curing temperatures up to 900°C without significant degradation [92]. Magnesium oxide also has very good thermal stability, remaining fully intact after annealing at 600°C, retaining higher resistivity and outperforming the magnetic properties of phosphate coated iron powder samples [29] [83]. Zinc oxide has less coverage in the literature as a coating material, but equally possesses high resisitivity and thermal stability. These three metal oxides; alumina, magnesium oxide and zinc oxide were selected for further trials. These coating materials were procured in a size range of 50 – 100 nm to give increased specific surface area over the previously tested ferrite powder of 1000 nm particle size, therefore improving the surface coverage for a constant amount of coating material.

5.3.1 Methodology and Procedure

The experimental methodology was very similar to that of the ferrite-glass coated samples as detailed in Section 5.2.1. The key difference involved the use of metal oxide nanoparticles in place of the ferrite powder. Zinc oxide, magnesium oxide and aluminium oxide nanopowder with average particle sizes in the range 50 – 100 nm were purchased from Sigma Aldrich. The basic properties of these alternative coating materials are given in in Section 3.1.3. The same processing procedures were followed and testing and analysis performed as for the ferrite-glass samples.

5.3.2 Results

Figure 45 shows the core loss at 1 T for metal oxide-glass coated samples with equal composition (0.5 wt% metal oxide, 0.4 wt% glass), with ferrite-glass sample included as a benchmark. All samples were cured for 1 hour at 450°C in a nitrogen atmosphere. Table 18 shows additional material properties for the same batch of samples to provide further insight.

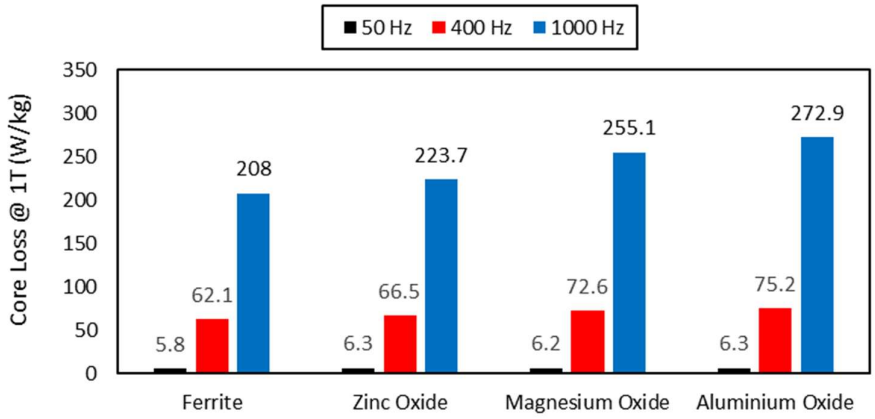

Figure 45: Core loss at 1 T for 0.5 wt% metal oxide-0.4 wt% glass coated samples

Composition	Density (g/cm^3)	TRS (MPa)	Resistivity (mΩcm)	H @ 1 T (A/m)
A1000C + 0.5% ferrite + 0.4% glass B	7.31	64.04	6.02	3445
A1000C + 0.5% ZnO + 0.4% glass B	7.28	75.92	15.73	4462
A1000C + 0.5% MgO + 0.4% glass B	7.23	59.71	9.62	4182
A1000C + 0.5% Al_2O_3 + 0.4% glass B	7.22	51.38	8.61	4354

Table 18: Material properties for 0.5 wt% metal oxide-0.4 wt% glass coated samples

At first glance, Figure 45 shows that none of the metal oxide-glass coated samples provide the same magnetic performance of the ferrite-glass coated samples, with higher core loss at all frequencies measured. However, the data in Table 18 provides valuable additional insight, with the zinc oxide coating offering higher strength and higher resistivity than the ferrite coating. This shows zinc oxide is indeed a promising candidate material, provided the poor permeability can be addressed. Magnesium oxide and aluminium oxide appear to not coat well to the iron, resulting in low density and consequently poor mechanical and magnetic properties in comparison to the ferrite coated sample. This is in agreement with K. J Sunday, who found alumina coated iron powder does not compact well and requires increased compaction pressures or additional lubricants to achieve high density [92]. The magnesium oxide and aluminium oxide coatings did improve resistivity over ferrite due to the smaller particle size giving better surface coverage. However, these smaller particles have a greater tendency to agglomerate, leading to reduced permeability and increased core losses. For particles in the nanometre to micrometer size range, as particle size decreases, the driving force for agglomerations increases, making uniform coating layers more difficult to produce [32].

Table 19 presents the particle size of each coating material alongside the theoretical and measured densities of the compacted samples, which are used to calculate porosity. Theoretical density is calculated assuming any lubricant used during the compaction process has fully burnt off during the

curing process. This assumption is tested by measuring the weight loss of these samples during the curing process and comparing to the weight of the lubricant minus the expected weight gain due to oxidation. The effect of any residual lubricant was found in Section 4.2.2 to be up to 0.06 wt%, or equivalent to < 0.01 g/cm^3, hence any residual lubricant has negligible effect on the measured density.

Composition	Particle Size (nm)	Theoretical Density (g/cm^3)	Measured Density (g/cm^3)	Porosity (%)
A1000C + 0.5% Ferrite + 0.4% glass B	1000	7.83	7.31	6.66
A1000C + 0.5% ZnO + 0.4% glass B	< 100	7.83	7.28	7.07
A1000C + 0.5% MgO + 0.4% glass B	< 50	7.82	7.23	7.58
A1000C + 0.5% Al_2O_3 + 0.4% glass B	< 50	7.82	7.22	7.73

Table 19: Estimated porosity for ferrite-glass and metal oxide-glass coated samples

It is observed from Table 19 that as coating particle size decreases, porosity of the compacted samples increases. The theoretical density, calculated from the proportional weights of the coating materials, is within 0.01 g/cm^3 for all coating materials. However, the measured density varies by 0.09 g/cm^3 - almost an order of magnitude more - showing a poorer distribution of coating material. This is because the finer nanoparticles tend to agglomerate, and hence do not achieve good surface coverage nor do they produce a uniform coating on the surface of the iron powder.

Due to the higher specific surface area of the nanoparticles, it was hypothesised that a smaller amount of coating material was required to fully coat the iron powder surface should they be successfully deagglomerated. Therefore, whilst the optimal amount of ferrite with 1000 nm particle size was found to be 0.5 wt%, the optimal amount of metal oxide nanoparticles was predicted to be lower. The specific surface area of manganese ferrite and zinc oxide nanoparticles are 4.9 m^2/g and 10 - 25 m^2/g respectively, a difference of 2 - 5 times. Therefore, the amount of metal oxide required was estimated to be 2 - 5 times less than the optimal amount of ferrite coating. This predicted a metal oxide coating amount of between 0.1 wt% and 0.25 wt% to give equivalent surface coverage. From this, an addition of 0.2 wt% metal oxide nanoparticles was selected for further trials.

Further samples with 0.2 wt% rather than 0.5 wt% metal oxide coating were produced, whilst maintaining the same amount of glass and otherwise following identical processing parameters. The properties of these 0.2 wt% metal oxide, 0.4 wt% glass coated samples are displayed in Figure 46 and Table 20.

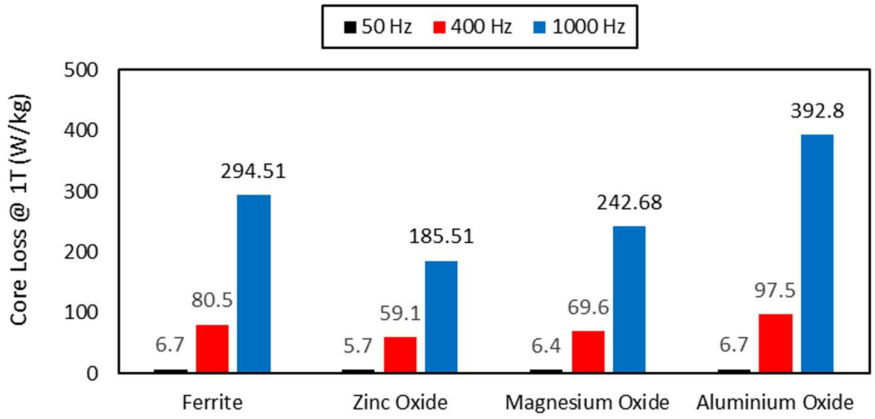

Figure 46: Core loss at 1 T for 0.2 wt% metal oxide-0.4 wt% glass coated samples

Composition	Density (g/cm^3)	TRS (MPa)	Resistivity (mΩcm)	H @ 1 T (A/m)	Core Loss @ 1 T (W/kg)		
					50 Hz	400 Hz	1 kHz
A1000C + 0.2% ferrite + 0.4% glass B	7.35	48.93	3.25	3317	6.7	80.5	294.5
A1000C + 0.2% ZnO + 0.4% glass B	7.36	54.98	11.64	3702	5.7	59.1	185.5
A1000C + 0.2% MgO + 0.4% glass B	7.29	47.37	5.61	3652	6.4	69.6	242.7
A1000C + 0.2% Al_2O_3 + 0.4% glass B	7.32	39.69	1.45	2948	6.7	97.5	392.8

Table 20: Optimisation of metal oxide-glass coated samples

Figure 46 shows that the reduced coating amount from 0.5 wt% to 0.2 wt% metal oxide decreased core loss in the zinc oxide sample below that of any other liquid-glass based sample. Table 20 confirms that the reduced coating amount significantly reduced the required field for an induction of 1 T, without much detriment to resistivity. This indiciates similar surface coverage despite the reduced coating amount. The magnesium oxide and aluminium oxide based coatings also showed improved permeability, but a larger cost to resistivity so this improvement was not reflected in the overall core loss. This may be due to the smaller particle size of the magnesium oxide and aluminium oxide nanoparticles to that of the zinc oxide nanoparticles, resulting in a higher tendency to agglomerate. From observation of the magnetic properties, the zinc oxide appears to have formed a thin uniform coating on the surface of the iron, whilst the aluminium oxide and magnesium oxide coatings appear to have agglomerated, leaving large areas of iron on iron contact with no coating to provide resistivity.

To prove this, the 0.2 wt% zinc oxide-glass and 0.2 %wt magnesium oxide-glass coated samples were examined under the SEM. Figure 47 shows SEM images of the raw fracture surfaces of these samples with EDX to illustrate elemental composition.

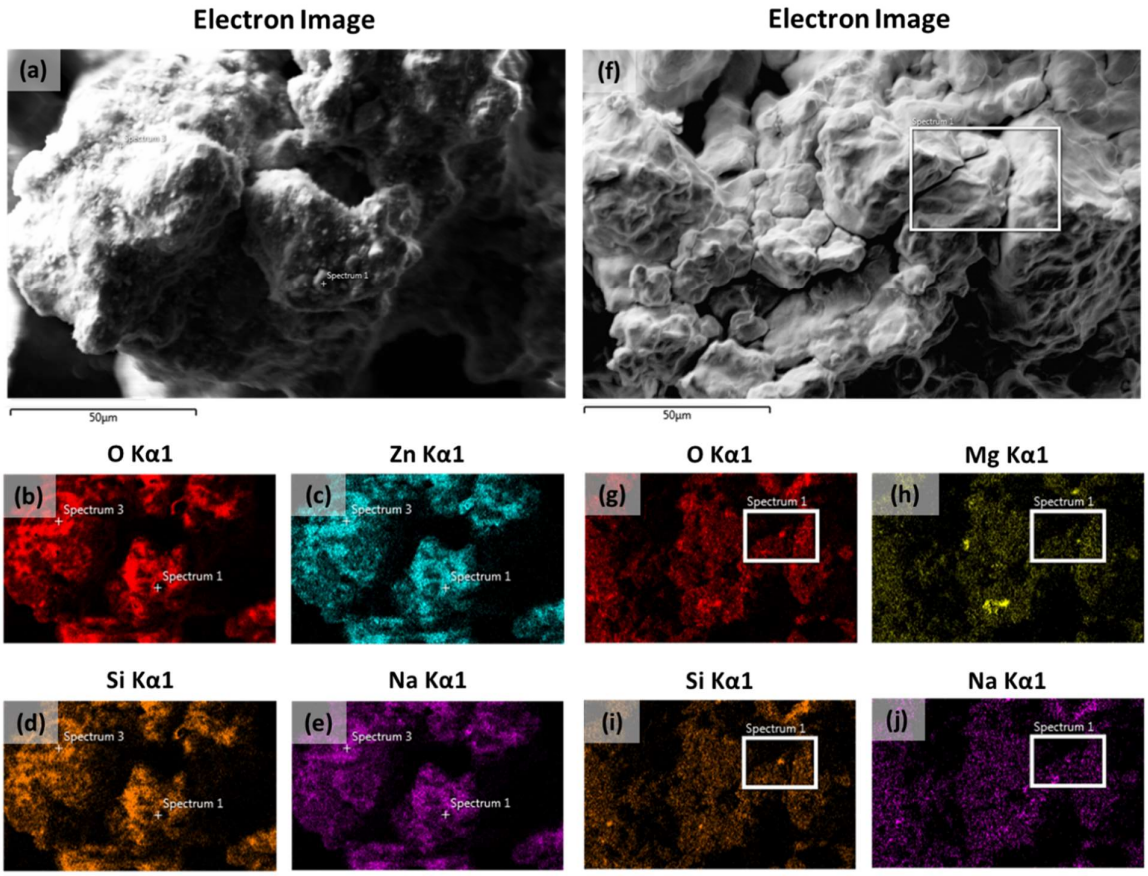

Figure 47: SEM and EDX images of raw fractures surfaces of (a)-(e) zinc oxide-glass coated sample; (f)-(j) magnesium oxide-glass coated sample

Figure 47 shows that the zinc oxide-glass coating is spread evenly over the surface of the iron powder. On the contrary, the magnesium oxide glass coating appears to have agglomerated, and in particular there are more concentrated areas of magnesium oxide in the pores of the iron particles. For example, there is an agglomeration of magnesium oxide particles that can be observed in the lower centre of Figure 47g and Figure 47h. These SEM and EDX images illustrate that the larger zinc oxide particles are more evenly spread over the entire surface of the iron powder than the smaller magnesium oxide particles, giving better surface coverage and improved resistivity.

Having improved the properties of the zinc oxide-glass coated sample by reducing the amount of zinc oxide addition, a comparison is made to the previously optimised ferrite-glass coated sample. Figure 48 shows the comparative hysteresis loops of the two coating materials dispersed in liquid glass.

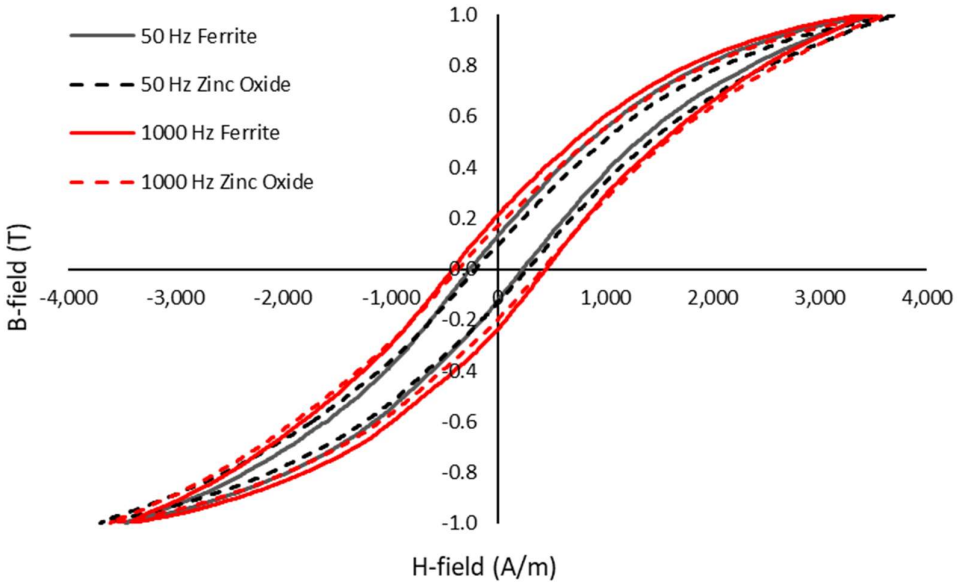

Figure 48: Comparison of ferrite-glass and zinc oxide-glass coated samples

Table 21 provides a comparison of the properties of each after some basic optimisation.

Composition	Density (g/cm^3)	TRS (MPa)	Resistivity (mΩcm)	H @ 1 T (A/m)	Core Loss @ 1 T (W/kg)		
					50 Hz	400 Hz	1 kHz
A1000C + 0.5% ferrite + 0.4% glass B	7.31	64.04	6.02	3445	5.8	62.1	208.0
A1000C + 0.2% ZnO + 0.4% glass B	7.36	54.98	11.64	3702	5.7	59.1	185.5
Difference (%)	-	**-14.15%**	**93.36%**	**7.46%**	**-1.72%**	**-4.83%**	**-10.81%**

Table 21: Comparison of ferrite-glass and zinc oxide-glass coated samples

Figure 48 shows hysteresis loops of similar width at 50 Hz for the zinc oxide-glass coated sample and the ferrite-glass coated sample, indicating similar coercivity and core loss at low frequency. The difference in width of the hysteresis loop is more pronounced at 1000 Hz, indicating improved resisitivity in the zinc oxide-glass coated sample. Table 21 confirms this, with the zinc oxide nanoparticle coating possessing improved resistivity and hence core loss at all frequencies, at a cost to permeability and strength.

Table 22 shows a comparison between the 0.2 wt% zinc oxide, 0.4 wt% glass coating and commercially available Ancorlam to provide a benchmark for performance. Both samples were produced under the same processing paramenters to provide a valid comparison.

Composition	Density (g/cm^3)	TRS (MPa)	Resistivity (mΩcm)	H @ 1 T (A/m)	Core Loss @ 1 T (W/kg)		
					50 Hz	400 Hz	1 kHz
Ancorlam Control	7.33	37.90	15.22	3043	6.4	57.6	174.3
A1000C + 0.2% ZnO + 0.4% glass B	7.36	54.98	11.64	3702	5.7	59.1	185.5
Difference (%)	-	**45.07%**	**-23.52%**	**21.66%**	**-10.94%**	**2.60%**	**6.43%**

Table 22: Comparison of Ancorlam and metal oxide-glass coated samples

Table 22 shows that the zinc oxide coating provides greater strength than commercially available Ancorlam, and thus is useful in strength limited applications. The zinc oxide-glass coated sample exhibits improved core loss at 50 Hz, however this worsens at higher frequencies due to the decreased resisitivity and permeability. In order to address the this, the coating method needs to be refined. If the nanoparticles can be effectively deagglomerated, less coating material would be required to fully coat the iron powder, improving permeability. Furthermore, if the nanoparticles are better spread over the iron, fewer iron-on-iron contact patches will be present, resulting in better resistivity.

5.4 Phosphate-Glass Coatings

Liquid glass based coatings have shown potential, but require improved permeability to compete with commercially available SMCs. In order to achieve high permeability, a thin uniform coating layer is required to maximise magnetic volume of the overall composite material. However, this poses a challenge when dispersing small particles in the liquid glass, as these particles tend to agglomerate. To address this, alternative base coatings without this limitation are sought.

Phosphate coatings do not possess this limitation and thus are an ideal candidate material to be used in conjunction with the liquid glass. Phosphate coatings are typically produced by a conversion process, resulting in a thin, uniform coating of insoluble metal phosphate crystals. This method offers good surface coverage and therefore high magnetic volume and permeability of the compacted composite material. Furthermore, phosphates are one of the most common coating materials used in SMCs, possessing high thermal stability and exhibiting strong adhesion to the base powder [Section 2.3.4] [7] [30]. In this section, the use of a hybrid phosphate-liquid glass coating system was investigated.

5.4.1 Methodology and Procedure

A phosphate layer was applied onto the base A1000C iron powder via a patented process. Liquid glass was dissolved in a solution of ethanol and distilled water, and the phosphated iron powder was added

stepwise whilst stirring continuously. The solution was then heated until all of the solvent had evaporated and the coated powder was then washed three times in deionised water. The resultant powder consisted of a phosphate-glass coating on the surface of the iron powder. The phosphate-glass coated iron powder was mixed with 0.4 wt% Kenolube and compacted into both toroidal and bar samples at 800 MPa.

5.4.2 Results

Figure 49 shows comparative hysteresis loops of ferrite-glass coated and phosphate-glass coated samples at an induction of 1 T at frequencies of 50 Hz and 1000 Hz. The ferrite-glass and phosphate-glass samples contain equal amounts of glass (0.4 wt%) and were both cured for one hour at 450°C in a nitrogen atmosphere.

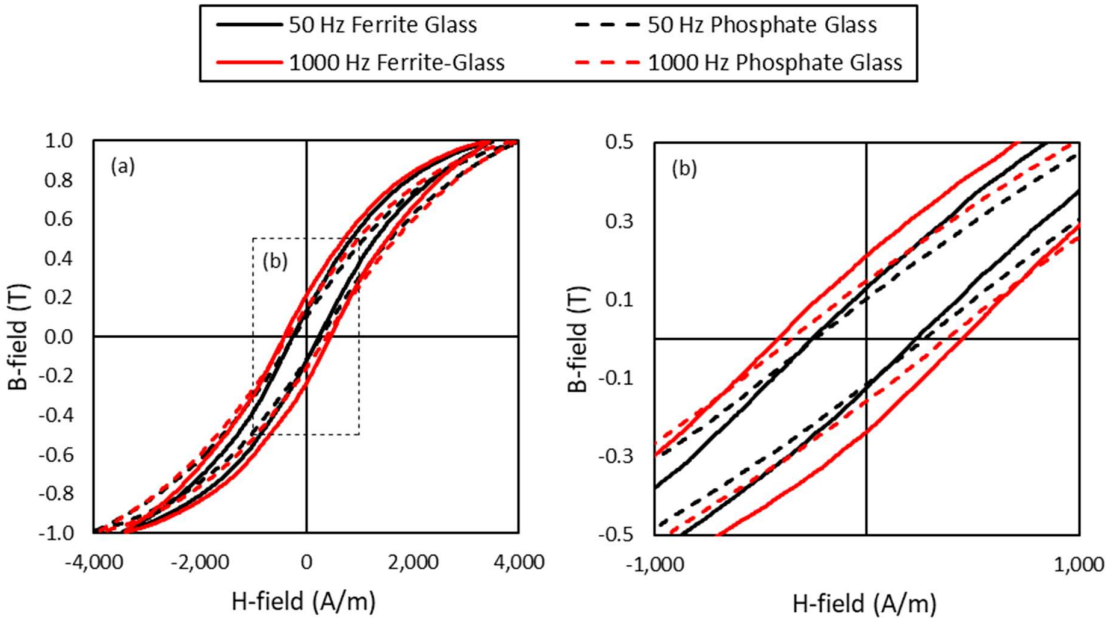

Figure 49: (a) Compariative hysteresis loops for ferrite-glass and phosphate-glass coated samples; (b) zoomed in view

Figure 49a shows that the phosphate-glass sample requires a larger H-field to reach an induction of 1 T, indicating poorer permeability than the ferrite-glass sample at both 50 Hz and 1000 Hz. However, Figure 49b shows that despite both samples having hystereisis loops of similar width at 50 Hz, the phosphate-glass sample has a thinner loop at 1000 Hz. This is due to the increased resisitivity offered by the phosphate coating, which more effectively contains the eddy current losses which are dominant at higher frequencies [Section 2.1.8].

Figure 50 presents core loss values for the ferrite-glass and phosphate-glass coated samples at 50 Hz, 400 Hz and 1000 Hz for an induction of 1 T.

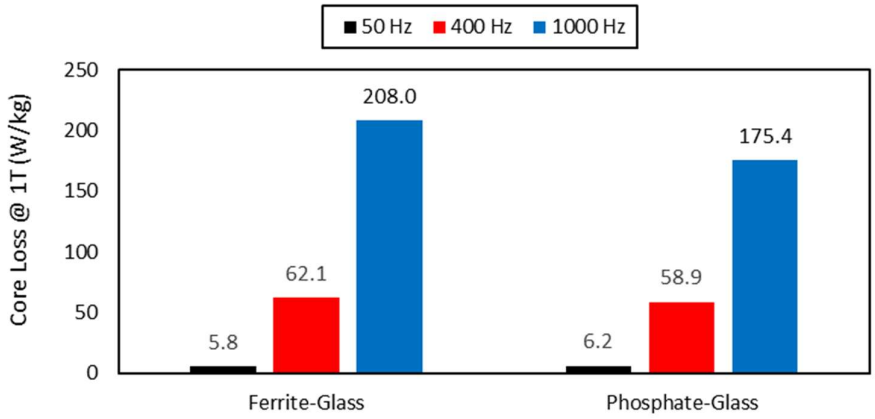

Figure 50: Core loss comparison between ferrite-glass and phosphate glass coated sample

Figure 50 shows that the phosphate-glass coated sample posseses higher core loss than the ferrite-glass coated sample at 50 Hz where hystereis losses are dominant, due to the increased permability. However, the phosphate-glass sample has lower overall core loss at 400 Hz and 1000 Hz where eddy current losses are dominant, due to the effects of the improved resistivity outweighing the cost of the increased permeability. From the promising core loss value of 175 W/kg at 1000 Hz, it is concluded that the phosphate-glass sample has potential to outperform the ferrite-glass sample and thus further trials were undertaken to optimise the phosphate-glass coating.

The amount of glass addition was varied to find the optimal amount for the phosphate-glass coating system. Figure 51 presents the key properties of phosphate-glass coated samples over a range from 0.2 wt% to 0.6 wt% glass.

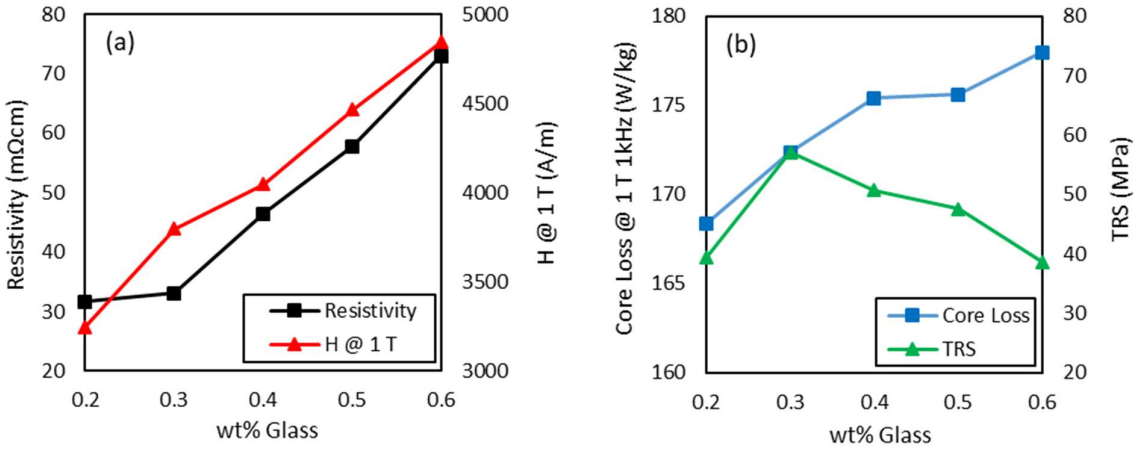

Figure 51: (a) Resistivity and H @ 1 T against wt% glass; (b) Core loss at 1000 Hz and TRS against wt% glass for phosphate-glass coated samples cured at 450°C

Figure 51a shows that as the amount of glass is increased from 0.2 wt% to 0.6 wt%, both resisitivity and the H-field for an induction of 1 T increase. These two properties have contrasting effects on the overall core loss. However, Figure 51b shows that the negative effects of the increased H-field at 1 T outweigh the positive effects of the increased resisitivity, as core loss at 1000 Hz is shown to also increase with wt% glass addition. Mechanical strength increases as the glass addition increases from 0.2 wt% to 0.3 wt%, allowing for full surface coverage of the glass binder over the iron particles. However strength decreases as the amount of liquid glass is increased to 0.6 wt%, as this is beyond the amount required for full surface coverage. The excess glass contributes towards a dual layer, inhibiting the diffusion iron of to the surface of the coating as part of the thermal oxidation bonding process (discussed further in section 4.2). This slows down the rate of oxidation and hence limits the increase in strength during the curing process.

It is concluded that after curing at 450°C, the core loss values at high frequency are promising due to the high resistivity. However, core loss values at low frequency are poor due to increased coercivity. In order to address this, the same set of samples were cured at 500°C, in order to further stress relieve the iron and improve coercivity. It was hypothesised that the promising resistivity of the phosphate-glass coating would be largely retained as phosphate coatings have been shown in the literature to be able to survive up to 500°C [89] [90]. Figure 52 presents the key properties of the set of phosphate-glass coated samples with 0.2 wt% to 0.6 wt% glass addition cured at 500°C.

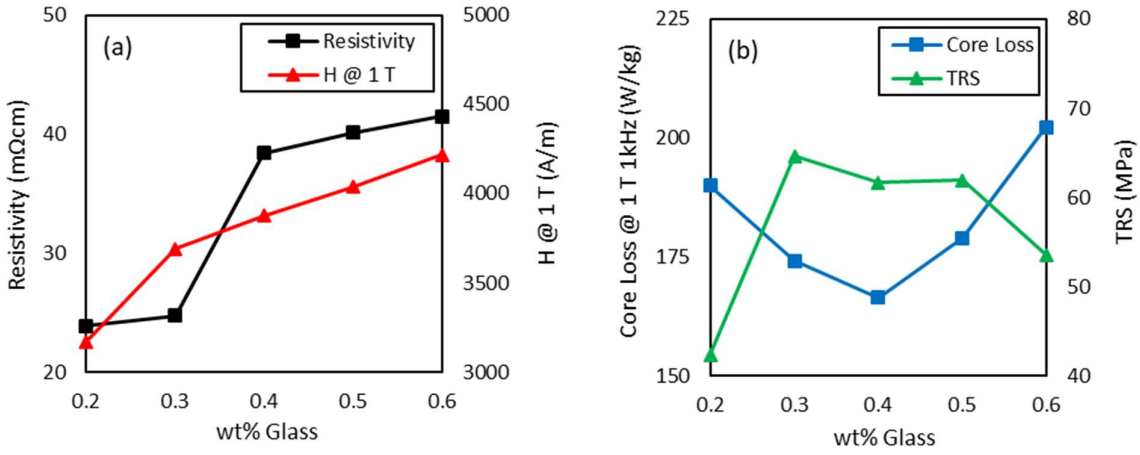

Figure 52: (a) Resistivity and H @ 1 T against wt% glass; (b) Core loss at 1000 Hz and TRS against wt% glass for phosphate-glass coated samples cured at 500°C

Figure 52a shows that H-field for an induction of 1 T and resisitivity both increase with wt% glass addition, as was the case at 450°C. Strength also follows the same trend at 500°C as at 450°C, increasing with extra glass addition from 0.2 wt% to 0.3 wt% as the glass acts as a binder material, but

decreasing as further glass is added up to 0.6 wt%. Core loss at 1000 Hz shows a different trend, displaying a U-curve with increasing glass addition, with core loss minimised at 0.4 wt%.

Assessing the optimal curing temperature, H-field at 1 T is smaller at 500°C than at 450°C, due to the additional stress relief leading to reduced coercivity and improved permeability. Resistivity is slightly lower after curing at 500°C as to be expected, but it is evident that the phosphate-glass coating has remained relatively intact. Figure 53 shows the corresponding effect on the overall core loss at 1000 Hz and strength after curing at 450°C and 500°C over a range of wt% glass additions.

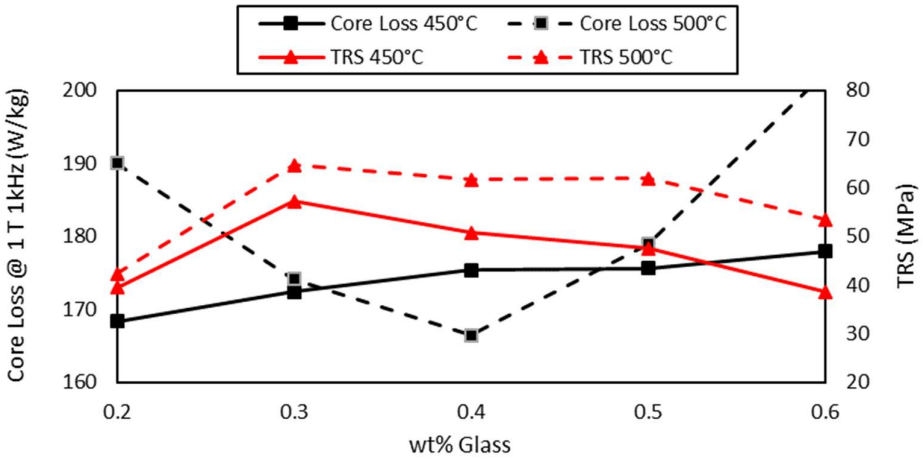

Figure 53: Core loss and TRS against wt% glass for phosphate-glass coated samples cured at 450°C and 500°C

Figure 53 shows that strength is slightly higher after curing at 500°C at all wt% glass additions due to the additional oxidation bonding at this increased temperature. The largest difference between curing at 450°C and 500°C is the overall effect on core loss. The lowest core loss after for all samples was found at 0.4 wt% glass after curing at 500°C. At this increased curing temperature, lower amounts of glass did not provide sufficient resistivity, and greater amounts of glass caused too significant a loss in permeability. The best overall properties are obtained after curing at 500°C, with 0.3 wt% glass for optimal strength, and 0.4 wt% glass for optimal core loss at 1000 Hz.

The mechanical and magnetic properties were found to improve with increasing curing temperature from 450°C to 500°C and thus the upper limits of thermal stability of the phosphate-glass coating were sought. Figure 54 presents the core loss and strength data of phosphate - 0.4 wt% glass samples cured at 450°C to 550°C.

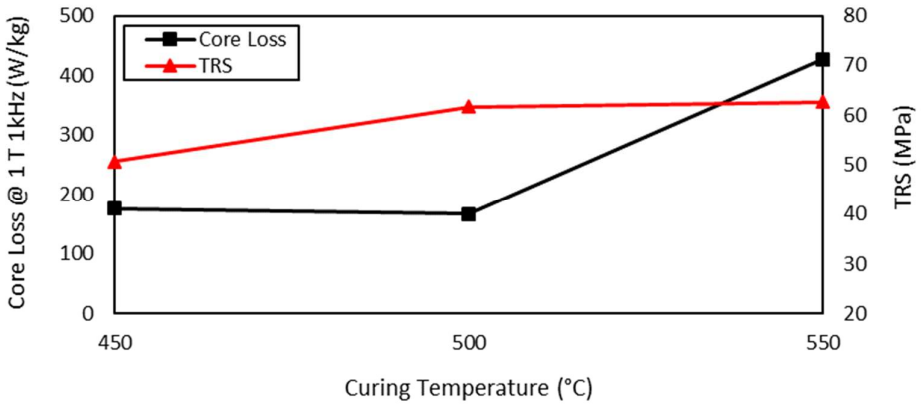

Figure 54: Core loss and TRS against curing temperature for phosphate-0.4 wt% glass samples

Figure 54 shows that whilst strength increases wth increasing curing temperature, core loss at 1000 Hz increases significantly as curing temperature is raised from 500°C to 550°C. The phosphate coating breaks down at 550°C and resistivity falls by more than two orders of magnitude. This is in agreement with the literature, which shows phosphate coatings degrade above 500°C [89] [90]. Overall, the properties of the phosphate-glass sample are optimal after curing at 500°C.

Table 22 shows a comparison between the phosphate - 0.4 wt% glass coating cured at 500°C and commercially available Ancorlam to provide a benchmark for performance. Both samples were compacted under the same conditions with equal 0.4 wt% lubricant additions.

Composition	Curing Temp (°C)	TRS (MPa)	Resistivity (mΩcm)	H @ 1 T (A/m)	Core Loss @ 1 T (W/kg)		
					50 Hz	400 Hz	1 kHz
Ancorlam Control	450	37.90	15.22	3043	6.4	57.6	174.3
A1000C + Phosphate + 0.4% glass B	500	61.64	38.42	3877	5.8	54.5	166.4
Difference (%)	-	62.64%	152.43%	27.41%	-9.38%	-5.38%	-4.53%

Table 23: Comparison of Ancorlam and phosphate-glass coated samples

Table 22 shows that the phosphate-glass coating provides greater strength and lower overall core loss at all frequencies measured than commercially available Ancorlam. The increased thermal stability allows for curing at higher temperature, contributing to both greater strength and lower coercivity. The core loss is further improved by the substantially increased resisitivity. The phosphate-glass coating is a useful alternative to Ancorlam with clear benefits. However, the main limiting factor to the phosphate-glass coating remains the relatively large H-field for an induction of 1 T, hence a thinner coating material is still sought.

5.5 Conclusion

In this chapter, use of liquid-glass as binder material within which to disperse various inorganic coating materials was investigated. Three classes of coating material were researched; ferrite-glass, metal oxide-glass and phosphate-glass. Table 24 provides a comparison of the key mechanical, magnetic and electrical properties of each coating system plus the Ancorlam control sample. Green text highlights superior properties, whilst red text highlights worse properties in comparison to Ancorlam.

Coating	Density (g/cm^3)	TRS (MPa)	Resistivity (mΩcm)	H @ 1 T (A/m)	Core Loss @ 1 T (W/kg)		
					50 Hz	400 Hz	1 kHz
Ancorlam Control	7.33	37.90	15.22	3043	6.4	57.6	174.3
Ferrite-Glass	7.31	**64.04**	**6.02**	**3445**	**5.8**	**62.1**	**208.0**
Zinc Oxide-Glass	7.36	**54.98**	**11.64**	**3702**	**5.7**	**59.1**	**185.5**
Phosphate-Glass	7.31	**61.64**	**38.42**	**3877**	**5.8**	**54.5**	**166.4**

Table 24: Comparison of Ancorlam and samples with liquid glass-based coating systems

Table 24 shows that the mechanical strength is fairly similar across all three coating systems, with ferrite glass having the highest strength and zinc oxide-glass the lowest. As for the magnetic properties, whilst permeability is best in the ferrite-glass samples, core loss is the highest due to poor resistivity. Conversely, permeability is worst in the phosphate-glass sample, but core loss is low, particularly at high frequency, due to the excellent resisitivity. The zinc oxide-glass coating material provides the lowest core loss of all at low frequency, with resisitivity and core loss at high frequency between that of the other two coating systems.

Each coating system was compared to commercially available Ancorlam at the end of each sub-section and again in Table 24. All three of the new coating systems possess greater mechanical strength, but poorer permeability than Ancorlam. Despite having worse permeability, the additional resisitivity offered by the phosphate-glass coating system results in lower overall core loss at all frequencies than the benchmark Ancorlam sample.

These three new coating systems are useful for use in applications where greater mechanical strength is required than currently offered by Ancorlam. The phosphate-glass coating system has lower core loss at all frequencies measured, thus offers better efficiency too. The main area for improvement remains the relatively poor permeability of the compacts offered by all coating systems investigated. This can be addressed by improving the coating procedure to give better surface coverage, requiring less coating material and increasing magnetic volume. Alternatively, a coating system is sought which can survive curing at higher temperatures, as this would serve to further stress relieve the iron, improving coercivity and permeability.

6 Silane-Based Hybrid Coatings

6.1 Introduction

In this chapter, silane coupling agents are investigated as an intermediary binder material to adhere other coating materials to the base iron powder. Silane coupling agents provide a durable bond between organic and inorganic materials [175]. The general formula for a silane is given in Figure 55.

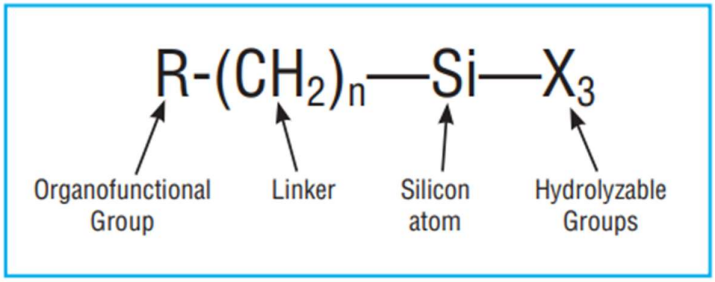

Figure 55: General formula for silane coupling agents *[176]*

The organofunctional group, denoted *R,* is a non-hydrolysable reactive group which forms chemical bonds with organic materials. Typical organofunctional groups include vinyl, epoxy, amino, methacryloxy and mercapto groups.

The hydrolysable silyl group, denoted *X,* hydrolyses to form a reactive silanol group, as shown in Figure 56. These silanol groups condense with other silanol groups to form siloxane linkages, which then condense to form a chemical bond with the hydroxyl groups present on the inorganic substrate, as illustrated in Figure 57. Typical hydrolysable groups include methoxy and ethoxy groups. Methoxy groups hydrolse rapidly to produce methanol, whilst ethoxy groups hydroysle more slowly, but form highly stable compositions and are more environmentally friendly, with a reaction product of ethanol.

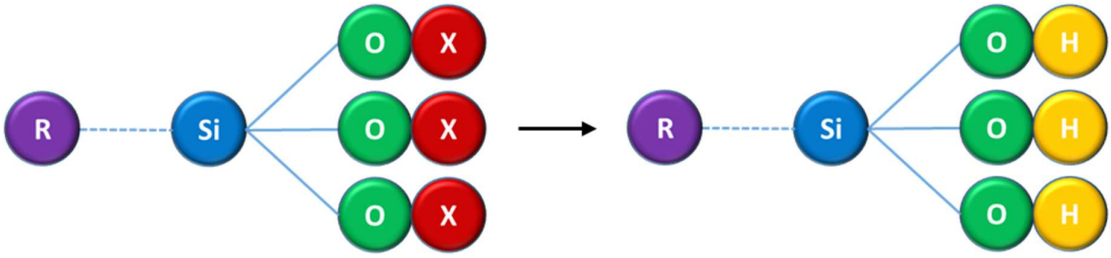

Figure 56: Hydrolysation of silyl group into silanol group

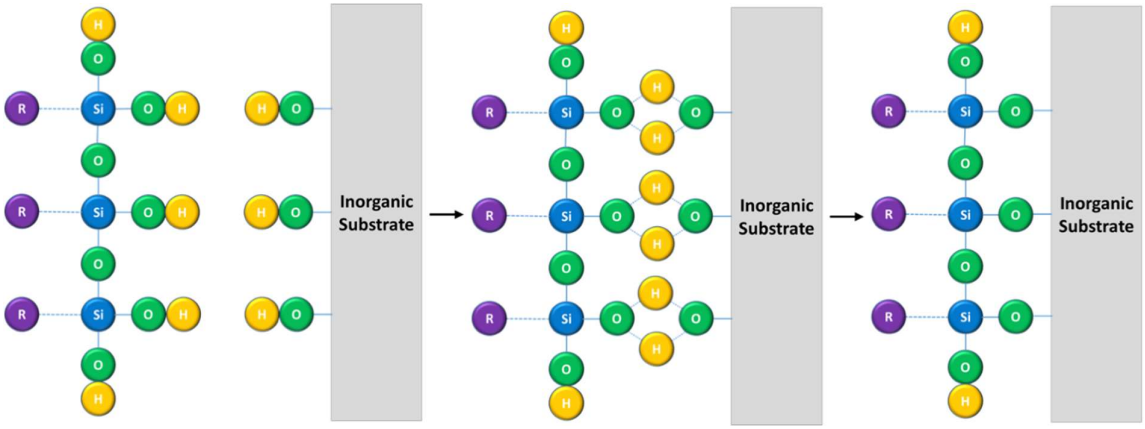

Figure 57: Bonding of silane coupling agent onto inorganic substrate via condensation reaction

Factors affecting the quality of the bond onto the inorganic substrate include the concentration of surface hydroxyl groups, type of surface hydroxyl groups, hydrolytic stability of the bond formed, and physical dimensions of the substrate. Surface modification is maximised when the substrate presents ample accessible hydroxyl sites for the silane to react with. Stable bonds are formed with oxides of aluminium, tin, titatnium and nickel as these materials possess many surface hydroxyl groups. Less stable bonds are formed with the oxides of iron, boron and carbon. Alkali metal oxides and carbonates do not form stable bonds with silanol groups. A list of substrates and their relative ability to form a stable bond with silanol groups is given in Figure 58.

	SUBSTRATES
EXCELLENT	Silica
	Quartz
	Glass
	Aluminum (AlO(OH))
	Alumino-silicates (e.g. clays)
	Silicon
GOOD	Copper
	Tin (SnO)
	Talc
	Inorganic Oxides (e.g. Fe_2O_3, TiO_2, Cr_2O_3)
	Steel, Iron
	Asbestos
	Nickel
	Zinc
	Lead
SLIGHT	Marble, Chalk ($CaCO_3$)
	Gypsum ($CaSO_4$)
	Barytes ($BaSO_4$)
POOR	Graphite
	Carbon Black

Figure 58: Silane effectiveness on inorganic substrates *[176]*

Most widely used organosilanes have one organic functional group and three hydrolysable groups, and are referred to as trialkoxy-silanes. Trialkoxy-silanes possess high reactivity due to significant cross linking density and produce strong bonds. Dialkoxy- and monoalkoxy-silanes are less common, and possess good stability after hydrolosis and produce straight-chain structures. As iron forms less stable bonds with silanol groups, a high cross linking density is required for effective bonding, and thus this research shall focus on trialkoxy silanes.

Silanes are used in SMC materials due to their favourable properties after the post compaction heat treatment process. Aichele and Koch showed that silicon containing coupling agents convert to a silicon-containing ceramic upon heat treatment under inert gas via a pyrolysis reaction, thereby enhancing the coercive field strength and thermal stability of the SMC material [177]. As the temperature is raised further, the silicon alloys into the surface of the iron to form an Fe-Si alloy layer with higher electrical resistance and a lower melting point than pure iron. Furthermore, the inorganic silicon-organic coating possesses good slip properties and lubricating characteristics, improving compressibility and density of the final SMC component.

There are various examples in the literature on the use of silane coupling agents for surface modification. Taghvari et al. demonstrated that coupling agents give better wetting and a more uniform coating distribution between iron powder and organic resin coating [178]. Chaudhury et al. used silane coupling agents to improve the wetting behaviour of inorganic fillers with polymers in inorganic materials, which are usually hydrophilic and therefore incompatible with organic polymers [179]. Jianwen et al. used silane coupling agents for the surface modifications of nanoparticles in order to improve dielectric properties of organic-inorganic nanocomposites [180].

6.2 Dual Silane Coatings

There is much research interest in the literature on the use of silanes for surface modification or as an intermediary binder to attach organic coating materials to the inorganic base powder. However, organic coating materials have lower thermal stability than inorganic coatings, as discussed in Section 2.3.4. This sub-section aims to build upon the literature by using a combination of dual silanes to bond inorganic coating materials to the base iron powder. Theoretically, this can be achieved by firstly surface treating the inorganic iron powder with “silane A”, leaving the organofunctional group exposed and free to bond with an organic group, as illustrated previously in Figure 57. Secondly, the inorganic coating material is surface treated with “silane B”, again leaving the organofunctional group free. By selecting two silanes with compatible organofunctional groups, for example an amine group and epoxide ring, the coupling agents can then be bonded together as illustrated in Figure 59.

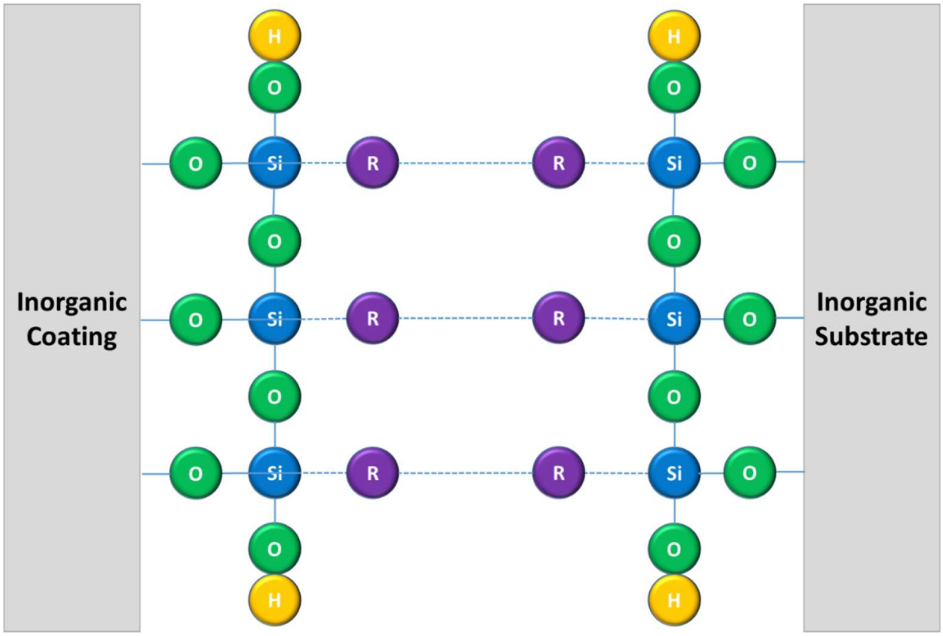

Figure 59: Bonding of inorganic coating material to inorganic substrate via dual silanes

To strengthen the bond between an inorganic coating material and an inorganic substrate material, dipodal silanes can be used. Dipodal silanes, as opposed to standard monopodal silanes, possess two sets of hydrolsable groups as illustrated in Figure 60. Functional dipodal silanes possess one (or more) organofunctional groups whereas non-functional dipodal silanes do not have an organofunctional group. As trialokxy dipodal silanes possess six hydrolsable groups, they have a theoretical cross linking potential of 100,000 times that of monopodal silanes which have only three hydrolsable groups [181]. This results in better substrate bonding and higher mechanical strength of the composite system.

In the same manner that two monopodal silanes linked by their organofunctional groups have two sets of hydrolsable groups available to bond with inorganic materials, it was hypothesised that the same would hold true for the two sets of hydrolsable groups available on a dipodal silane. Therefore, a combination of monopodal and dipodal silanes will be used in order to bind together the base iron powder and inorganic coating material.

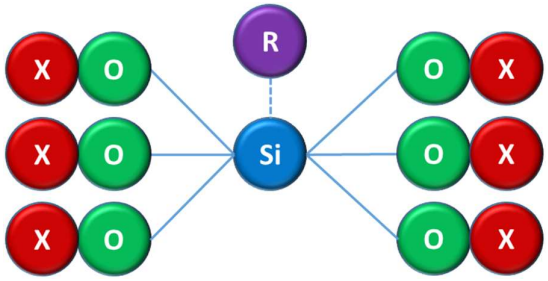

Figure 60: Schematic of functional dipodal silane

6.2.1 Methodology and Procedures

A1000C powder from GKN Hoeganaes Corporation was used as the core powder in the as-received state, as detailed in Section 3.1.1. Dual-silane trials were conducted using magnesium oxide nanopowder and zinc oxide nanopowder as the inorganic coating materials, both purchased from Silma Aldrich. These two coating materials exhibited favourable properties such as high resistivity when dispersed in liquid glass [Section 5.3]. Three silane coupling agents were selected for use in the dual silane trials, all purchased from Gelest Inc;

- 3-aminopropyltriethoxysilane (APTES)
- (3-glycidoxypropyl)-trimethoxysilane (GLYMO)
- 1,2-bis(triethoxysilyl)ethane

APTES is an amine functional monopodal silane, GLYMO a glycidoxy functional monopodal silane and 1,2-bis(triethoxysilyl)ethane a non-functional dipodal silane. Key properties for all coating materials and coupling agents are given in Section 3.1.3.

APTES was selected as the primary silane to bond directly to the iron powder, and either GLYMO or the non-functional dipodal as the secondary silane to bond to the inorganic coating material. Dual silane trials were separated into two separate categories; dual monopodal using APTES and GLYMO, and monopodal-dipodal using APTES and the non-functional dipodal silane. It should be noted that the use of a dual silane should not increase the overall proportion of silane in the final composite, as this would be detrimental to permeability. Rather, the secondary silane is designed to replace some of the primary silane.

APTES was dissolved in a solution of 95 vol% ethanol / 5 vol% distilled water and stirred continuously for ten minutes. A1000C iron powder was added stepwise into the solution whilst stirring continuously and the pH value was adjusted to 8 using acetic acid. The mixture was stirred continuously for thirty minutes to ensure the reaction was complete, resulting in the iron powder being surface treated with the primary silane, APTES.

Similarly, the secondary silanes were dissolved in a solution of 95 vol% ethanol / 5 vol% distilled water and stirred continuously for ten minutes. The inorganic coating material (either magnesium oxide or zinc oxide nanopowder) was added to the solution and dispersed for a further ten minutes using ultrasonic treatment. The resulting solution was adjusted to a pH-value of 8 using acetic acid and stirred for thirty minutes. The corresponding reaction results in the inorganic coating material being surface treated with the secondary silane.

The primary silane and secondary silane solutions were then mixed together and stirred for one hour to complete the desired reaction. In the case of the dual monopodal silane trial (APTES-GLYMO) the organofunctional group of GLYMO is an epoxy ring, which opens up and forms a covalent bond with the amine organofunctional group of the APTES. In the case of the monopodal and non-functional dipodal silane trial (APTES-Dipodal), the unreacted hydrolsable groups on the dipodal silane react with the unreacted hydroxide groups on the surface of the iron powder. In both cases, a continuous bond between iron powder and inorganic coating material is formed. The mixtures were then dried for two hours at 90℃ on a hot plate and the dry powder was washed three times in deionised water to remove impurities.

A lubricant addition of 0.4 wt% Kenolube was mixed into the coated powder prior to uniaxial cold compaction at a pressure of 800 MPa. Toroidal samples with outer diameter 36 mm, inner diameter 22 mm and height 6 mm and bar samples with length 30 mm, width 12 mm and height 6 mm were produced. These samples were heat treated at 450 - 550℃ for one hour in a nitrogen atmosphere to reduce the internal stresses caused by compaction.

After heat treatment, cured density was measured for all samples. Toroidal samples were wrapped with 100 windings on the primary coil and 40 windings on the secondary coil in order to measure AC hysteresis loops at B = 1 T at a frequency range of 50 - 1000 Hz. Bar samples were used to measure resistivity via the four point probe method before measuring TRS through the three point bend test. Fracture surfaces of the broken samples were polished and etched for examination of the microstructure under SEM with EDX capability to understand coating thickness and uniformity.

6.2.2 Results

The constituents amounts of metal oxide and silane for the APTES-Dipodal trials were selected to be 0.2 wt% metal oxide, 1 wt% APTES and 0.2 wt% non-functional dipodal silane. These amounts were chosen due to the favourable properties at a coating amount of 0.2 wt% metal oxide in the liquid-glass trials, whilst 1 wt% APTES and 0.2 wt% dipodal silane were selected to achieve a 5:1 weight ratio of monopodal to dipodal silane ratio as recommended by the supplier [181]. For the APTES-GLYMO trials, equal amounts of the constituent materials were used as per the APTES-Dipodal trials, with the GLYMO replacing the non-functional dipodal silane.

In order to determine the state of the coating on the iron particles, the microstructure was examined under the microscope. Figure 61 presents SEM and EDX images of the fracture surface of the magnesium oxide-(APTES-dipodal) coated sample.

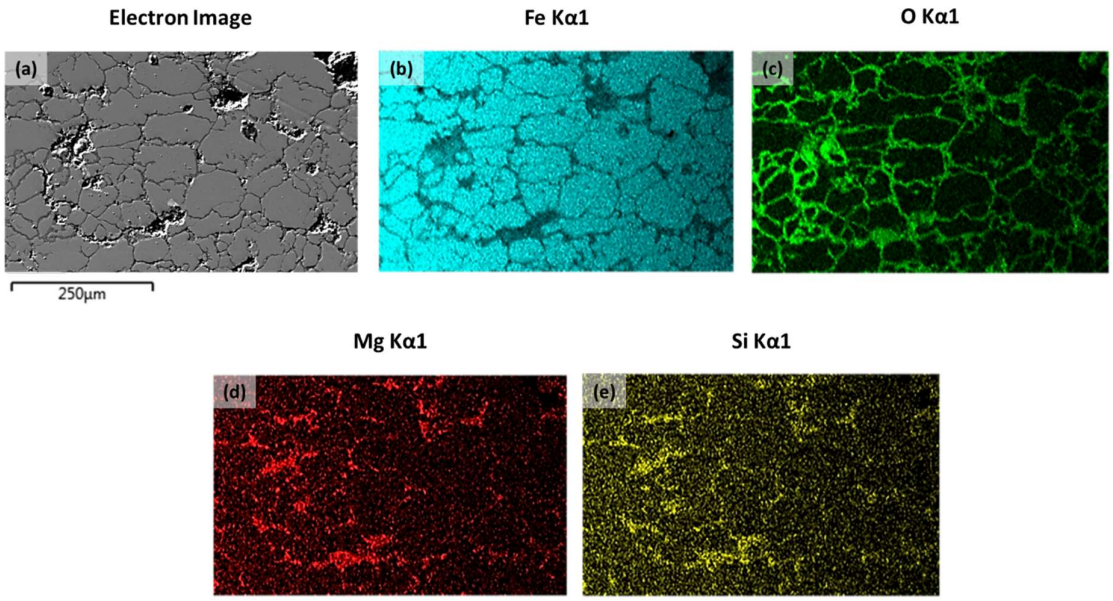

Figure 61: SEM/EDX images of fracture surface of magnesium oxide-dual silane coated sample

Figure 61 shows that the EDX detected the presence of oxygen, magnesium and silicon, the elements present in magnesium oxide and silane. It is therefore concluded that a thin coating of magnesium oxide-silane was formed on the surface of the iron particles. The magnesium and silicon elemental maps show clusters in the pores on the iron, which may be interpreted as agglomerations of the coating material. However, the polished surface creates a cross-sectional slice through the sample, with the topographical features or dips leaving unpolished areas where the coating remains intact. This can be proven by examination of the loose powder prior to compaction, as shown in Figure 62.

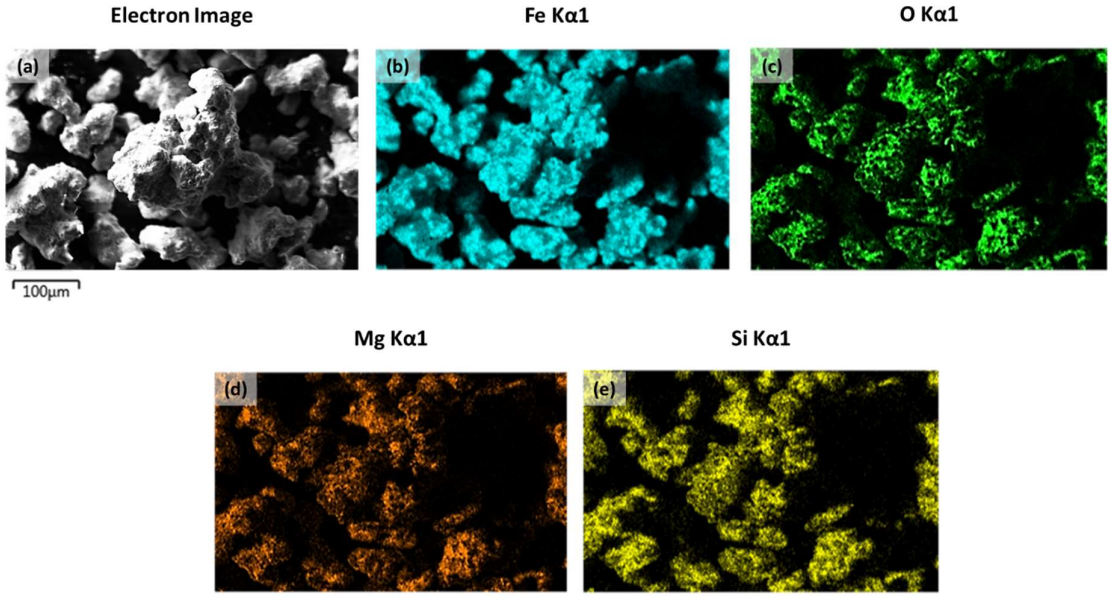

Figure 62: SEM/EDX images of loose magnesium oxide-dual silane coated powder

Figure 62 shows the presence of magnesium oxide and silane coupling agent on the surface of the iron powder. It is noted that there is a lower intensity of oxygen detected relative to the other coating materials than in Figure 61. This is due to these images being taken of the loose powder in the green state, prior to the curing process and the formation of oxide bonds between the iron particles.

Magnetic characterisation was performed in order to assess the magnetic performance of the dual silane metal oxide coated samples. Figure 63 presents comparative AC hysteresis loops for an induction of 1 T over a frequency range of 50 to 1000 Hz for the APTES-dipodal sample and the APTES-GLYMO sample, both using magnesium oxide as the inorganic coating material. Both samples were mixed with 0.4 wt% Kenolube before being compacted under a pressure of 800 MPa and subsequently heat treated for one hour at 450°C in a nitrogen atmosphere.

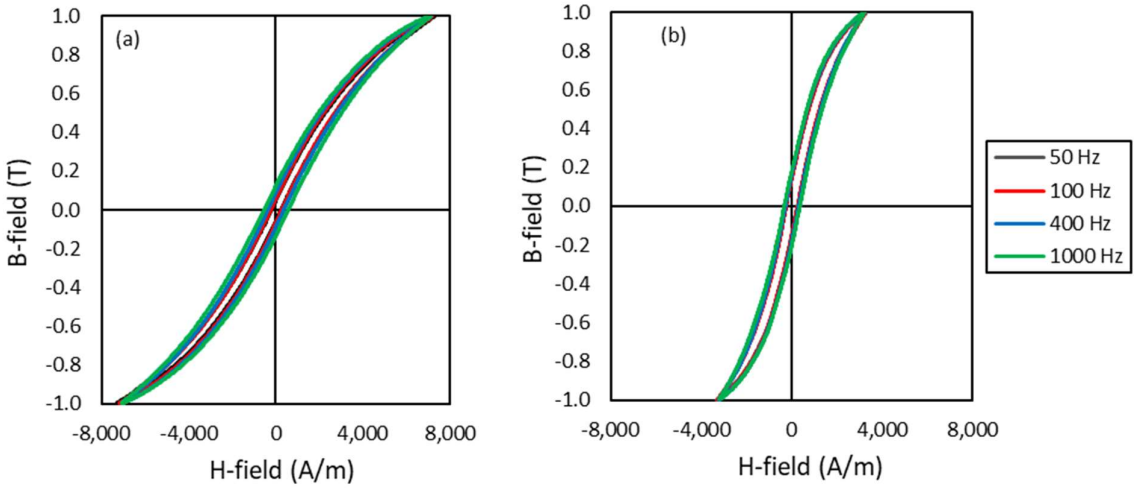

Figure 63: AC hysteresis loops for (a) APTES-GLYMO magnesium oxide coated iron; (b) APTES-dipodal magnesium oxide coated iron

Figure 63 shows that both dual silane mixes provided an electrically insulating coating on the surface of the iron powder, illustrated by the relatively narrow hysteresis loops, which are maintained as frequency is increased. It is clear from the gradient of the hysteresis loops that the sample containing the APTES-Dipodal silane combination has greater permeability than that with the APTES-GLYMO silane combination. Therefore, the APTES-Dipodal silane combination was taken into further trials.

Figure 64 presents comparative AC hysteresis loops for an induction of 1 T over a frequency range of 50 to 1000 Hz for the magnesium oxide and zinc oxide coated iron powder samples, both using the APTES-Dipodal combination of silanes. Both samples were heat treated for one hour at 450°C in a nitrogen atmosphere.

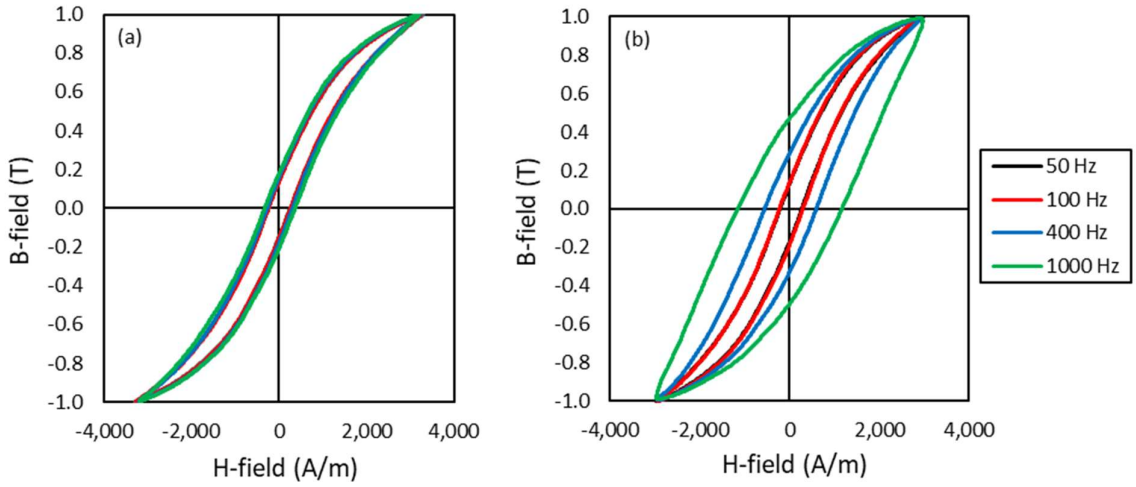

Figure 64: AC hysteresis loops for (a) Dual silane magnesium oxide coated iron; (b) Dual silane zinc oxide coated iron

Figure 64a shows that the magnesium oxide nanoparticles provided an effective insulation layer, producing a narrow hysteresis loop at all frequencies measured and indicating that they bonded well to the iron via the dual silane coupling agents. Figure 64b shows that whilst zinc oxide nanoparticles also provided some level of insulation at lower frequencies, the hysteresis loop broadens significantly at 400 Hz and 1000 Hz. This indicates poor insulation and containment of eddy current losses, suggesting that the zinc oxide nanoparticles did not bond as well to the silane coupling agents as the magnesium oxide nanoparticles.

As the magnesium oxide coated samples demonstrated more potential than the zinc oxide coated samples, further trials were undertaken with the former. In order to understand the role of the dual silanes and whether they offered an improvement over the more conventional use of a single silane coupling agent, samples of magnesium oxide coated via a single silane were prepared. An additional 0.2 wt% of the primary monopodal silane APTES was used in place of the 0.2 wt% non-functional dipodal. The composition for the single silane samples was iron with 1.2 wt% APTES and 0.2 wt% magnesium oxide. Samples were processed using the same compaction and heat treatment parameters as the dual silane samples. Comparative AC hysteresis loops are provided in Figure 65. The corresponding mechanical and magnetic properties are given in Table 25.

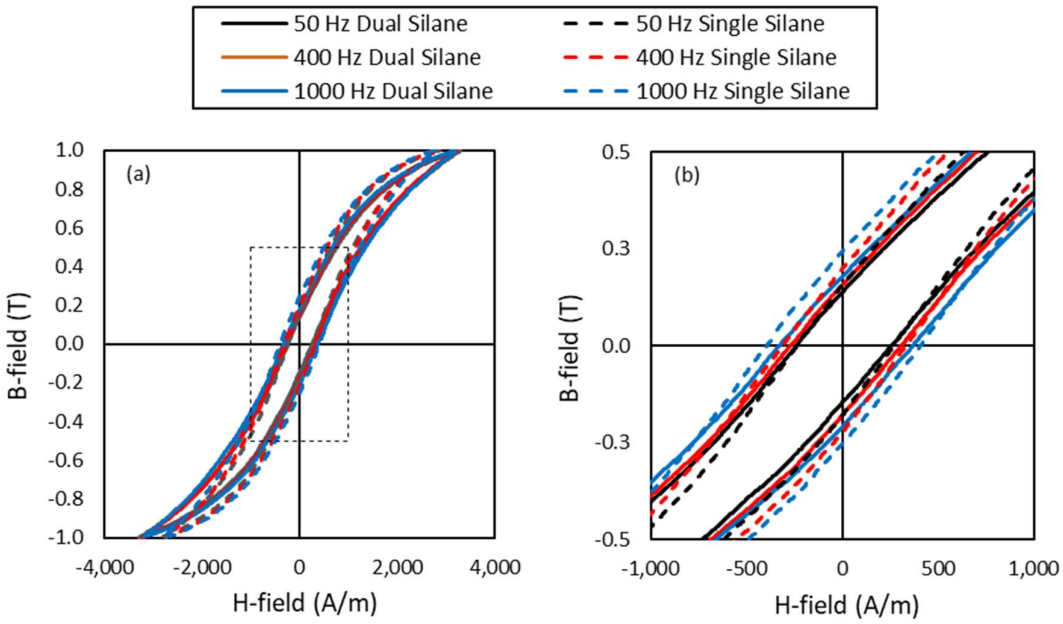

Figure 65: (a) Comparative AC hysteresis loops for dual silane and single silane magnesium oxide coated iron; (b) zoomed in view

Composition	Density (g/cm^3)	TRS (MPa)	Resistivity (mΩcm)	H @ 1 T (A/m)	Core Loss @ 1 T (W/kg)		
					50 Hz	400 Hz	1 kHz
A1000C + (APTES & Dipodal) + MgO	7.32	39.11	16.59	3304	6.3	58.0	170.1
A1000C + (APTES only) + MgO	7.35	33.66	10.80	2862	5.8	58.3	187.4

Table 25: Key properties of single and dual silane magnesium oxide coated samples

Figure 65 shows that the use of a single silane decreases the required H-field for an induction of 1 T, indicating an improvement in permeability. However, this comes at a cost of a broader hysteresis loop due to decreased resistivity, particularly as frequency is increased. Table 25 confirms these observations, with the single silane sample possessing better permeability and core loss at 50 Hz, but the dual silane sample having better resistivity and core loss at 1000 Hz. Furthermore, the dual silane has better mechanical strength due to the replacement of some of the base silane with the dipodal silane, which results in an increased cross linking density between iron powder and magnesium oxde coating.

The dual silane combination results in better mechanical strength and core loss at high frequency. To address the poorer permeability and core loss at low frequency, samples were cured at a higher temperature in order to further stress relieve the iron and improve coercivity. Table 26 presents a

comparison of the properties of the dual silane magnesium oxide coated sample cured at the original 450°C and at an increased temperature of 500°C.

Curing Temperature (°C)	Density (g/cm³)	TRS (MPa)	Resistivity (mΩcm)	H @ 1 T (A/m)	Core Loss @ 1 T (W/kg)		
					50 Hz	400 Hz	1 kHz
450°C	7.32	39.11	16.59	3304	6.3	58.0	170.1
500°C	7.34	42.20	6.35	2982	5.5	58.7	192.7
Difference (%)	-	**7.90%**	**-61.72%**	**-9.75%**	**-12.70%**	**1.21%**	**13.29%**

Table 26: Key properties of dual silane magnesium oxide coated samples cured at 450°C and 500°C

Table 26 demonstrates that curing at an elevated temperature does indeed have the desired effect of improving coercvitiy, as observed by the decrease in H @1 T and core loss at 50 Hz. This also has the beneficial effect of increasing strength through further thermal oxidation bonding. However, as observed in Chapter 5 in the liquid glass based samples, curing at elevated temperature also comes at a cost to the resisitivity, and consequently increased core loss at high frequency.

In Chapter 5, it was concluded that phosphating the base iron led to a large increase in resistivity and improved thermal stability. Therefore, it was hypothesised that samples could be heat treated at 500°C and benefit from the reduced coercivity without an overall increase in core loss. The following trial assesses whether the increase in resistivity and thermal stability brought by phosphating the base iron powder can also be afforded to the dual silane magnesium oxide coating. The constituent amounts of silanes and magnesium oxide coating were halved in order to account for the additional phosphate layer without much detriment to the permeability, due to increased non-magnetic volume. Iron powder was phosphated according to a patented process as per Chapter 5.

Samples were prepared with the phosphated iron powder, plus 0.5 wt% APTES, 0.1 wt% non-functional dipodal and 0.1 wt% magnesium oxide nanopowder. Figure 66 presents the core loss values at 1 T and 50 - 1000 Hz for the standard (unphosphated) iron and the phosphated iron, each after curing at 450°C and 500°C.

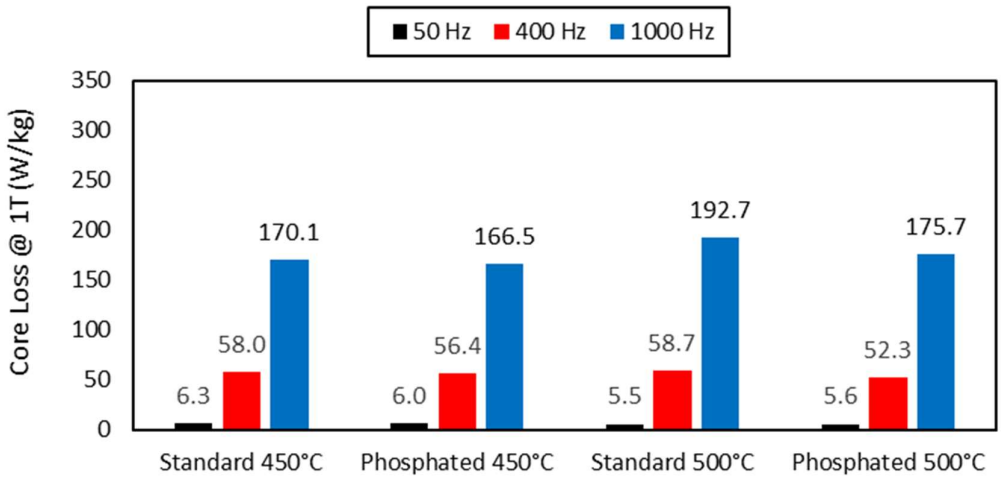

Figure 66: Core loss of pure iron and phosphated iron with dual silane magnesium oxide coating

Figure 66 shows that phosphating the base iron powder has a positive impact on core loss at all frequencies and temperatures measured. The only exception is core loss at 50 Hz after curing at 500°C, which is marginally higher in the phosphated sample, as the positive effects of the increased resisitivity are not realised at low frequency. Essentailly, half of the dual silane magnesium oxide coating system was substituted for a phosphate pre-coating to maintain a similar non-magnetic volume.

For the phosphated samples, core loss at 50 Hz and 400 Hz is minimised after curing at 500°C, as the increased temperature results in further stress relief of the iron. At a frequency of 1000 Hz, core loss is minimised in the phosphate sample cured at 450°C, due to the better retention of resistivity at this curing temperature. The ideal curing temperature therefore depends upon the frequency of the desired application.

Table 27 presents a comparison between the phosphate-dual silane-magnesium oxide coated sample and commercially available Ancorlam, both cured at 450°C.

Composition	**Density (g/cm^3)**	**TRS (MPa)**	**Resistivity (mΩcm)**	**H @ 1 T (A/m)**	**Core Loss @ 1 T (W/kg)**		
					50 Hz	**400 Hz**	**1 kHz**
Ancorlam Control	7.33	37.90	15.22	3043	6.4	57.6	174.3
Phosphate-Dual Silane-MgO	7.32	24.99	99.58	3559	6.0	56.4	166.5
Difference (%)	-	**-34.06%**	**554.27%**	**16.96%**	**-6.25%**	**-2.08%**	**-4.48%**

Table 27: Comparison of Ancorlam and phosphate dual silane magnesium oxide coated sample

Table 27 shows a similar pattern to the results of the liquid glass in Chapter 5. The phosphate-dual silane-magnesium oxide coating system provides lower overall core loss than Ancorlam through greatly increased resistivity at a smaller cost to permeability. However, unlike where the liquid glass

offers an increase in strength, the phosphate-silane binder decreases strength. It is concluded that the phosphate-dual silane-magnesium oxide coating relies on too many intermediate bonds, and a simpler bonding model should be considered. One major benefit of the phosphate - dual silane - magnesium oxide coating system is the excellent resisitivity, more than five times that of Ancorlam, and as such phosphate-silane based coatings systems do show potential.

6.3 Phosphate-Silane Coatings

In this sub-section, phosphate-silane based coating systems were further investigated due to their excellent resistivity measured in section 6.2.2. The use of dual silanes to bond a coating material onto the iron powder relies on too many intermediate bonds, impacting permeability. Therefore, a simpler coating system was sought.

Phosphate-silane based coating systems have been researched in the literature, for example Fan et al. investigated the use of APTES to surface treat phosphated iron to improve bonding behavior to an organic resin coating [182]. However, this research only measured magnetic properties in the frequency range greater than 1000 kHz, at which point hysteresis losses are negligible in comparison to eddy current losses [Section 2.1.7]. Taghvaei et al. also investigated the use of phosphated iron powder with APTES surface treatment, measuring magnetic performance but not considering mechanical properties [89]. As in these two examples, current research into the use of silanes in SMC materials focuses heavily of the use of the silane APTES, but does not consider alternative silanes. Whilst these materials display good magnetic properties, APTES has a slow reaction time and is hazardous in large quantities and therefore is not ideal for large scale production [133].

This research builds upon the concept of phosphate-silane coating systems, but seeks to find alternate silanes to the commonly used silane known as APTES. Furthermore, the mechanical performance of the final SMC composite material shall also be investigated in addition to the magnetic properties.

6.3.1 Methodology and Procedures

Silane coupling agents with either amine or sulphur based groups adhere most strongly to iron substrates [176]. Therefore, alternate silanes were identified with either of these two groups. Two silane mixes and three functional dipodal silanes were identified for use;

- Sivate A610 Activated Amine Functional Silane (herein referred to as Activated APTES)
- Sivate E610 Enhanced Amine Functional Silane (herein referred to as Enhanced APTES)
- Bis[3-TriMethoxy-SilylPropyl]Amine (herein referred to as Amine Dipodal)
- N,N'-Bis[3-(TriMethoxySilyl)-Propyl] EthyleneDiamine (herein referred to as Di-amine Dipodal)
- Bis[3-(TriEthoxySilyl)-Propyl]DiSulphide (herein referred to as Di-sulphide Dipodal)

All five selected silanes were purchased from Gelest Inc, and their properties are given section 3.1.3.

A1000C powder from GKN Hoeganaes Corporation was used as the core powder in the as-received state, as detailed in Section 3.1.1. A phosphate layer was reacted onto the surface of the base iron powder according to a patented process. The five selected silanes were each dissolved in a solution of 95 vol% ethanol / 5 vol% distilled water and stirred continuously for ten minutes.

A1000C iron powder was added stepwise into each previously prepared solution whilst stirring continuously. The pH-value was adjusted to 8 using acetic acid, and the resulting mixture was stirred for one hour to complete the reaction. One exception to this was the surface treatment using Activated APTES, which was stirred for five minutes, due to the faster reaction time [183].

The resultant mixtures were dried for two hours at 90℃ on a hot plate and the dry powders were washed three times in deionised water to remove impurities. The same processing conditions for compaction and heat treatment, and subsequent measurement and anlaysis techniques were used as per the dual silane trials detailed in Section 6.2.1.

6.3.2 Results

Initial phosphate-silane coating trials were conducted using phosphated iron powder with 0.5 wt% silane surface treatment. Figure 67 presents SEM and EDX images of the fracture surface of a phosphate-activated APTES coated sample.

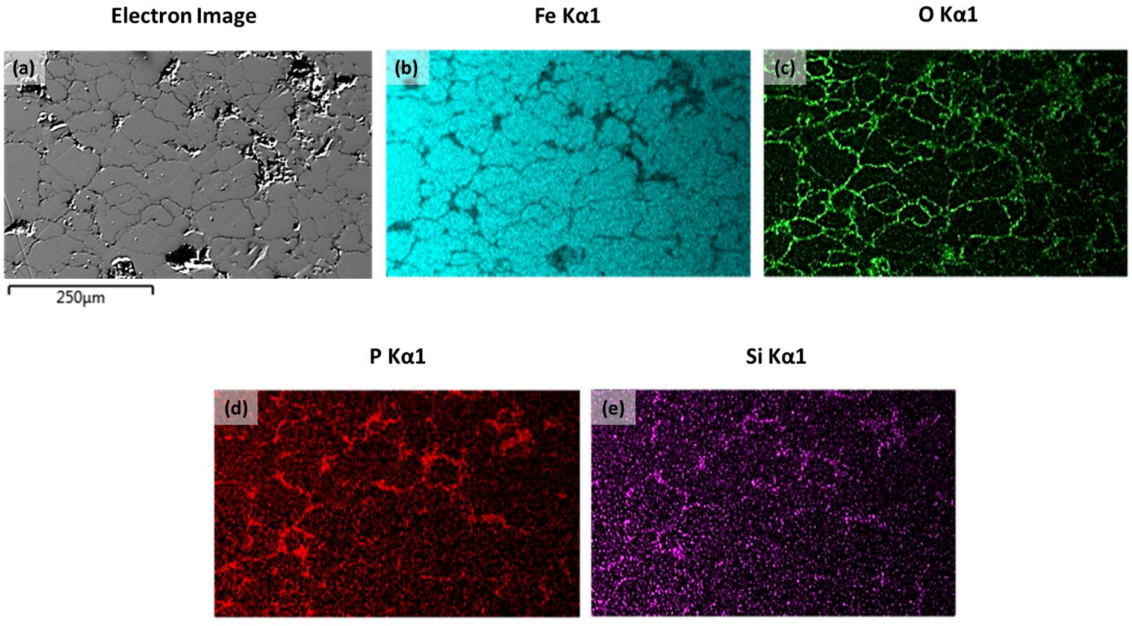

Figure 67: SEM/EDX images of polished fracture surface of activated APTES treated phosphated iron powder sample

Figure 67 shows that oxygen, phosphorus and silicon, the main elements present in phosphate and silane were detected by the EDX. It follows that a thin layer of phosphate-silane was formed on the surface of the iron particles. The intensity of the oxygen detected is greater than that of the other coating materials as oxygen is present in both phosphate and silane, and due to the formation of oxide bonds between the iron particles as part of the thermal oxidation bonding process during heat treatment.

Figure 68 presents the comparative hysteresis loops at a frequency of 50 Hz and induction of 1 T for each of the five silanes selected. Figure 69 shows the corresponding core loss at 1 T for a frequency range of 50 - 1000 Hz. Results are shown for the samples cured at 500°C which possess lower core loss than those cured at 450°C due to the increased thermal stability offered by the phosphate-silane coating.

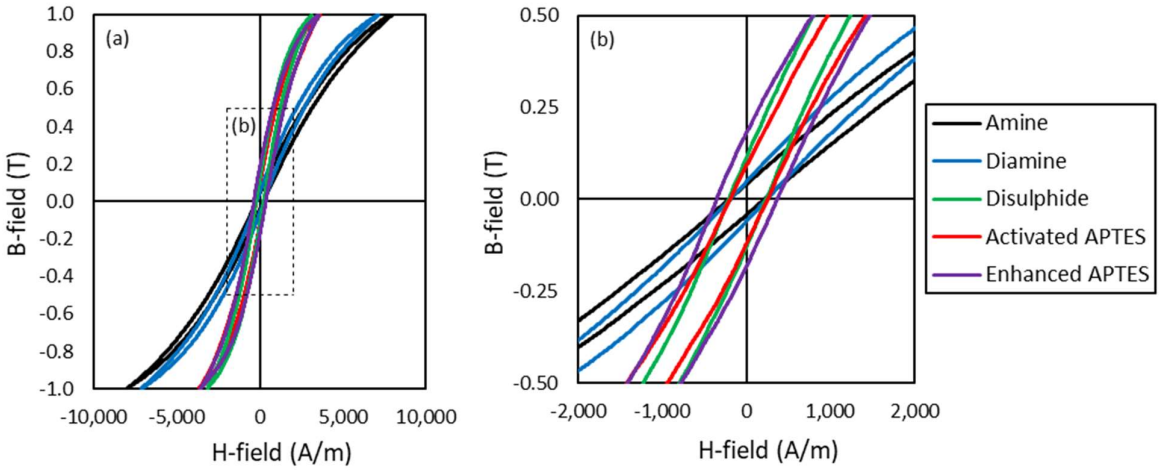

Figure 68: (a) Comparative AC hysteresis loops at 50 Hz for silane-treated phosphated iron powder samples cured at 500°C; (b) zoomed in view

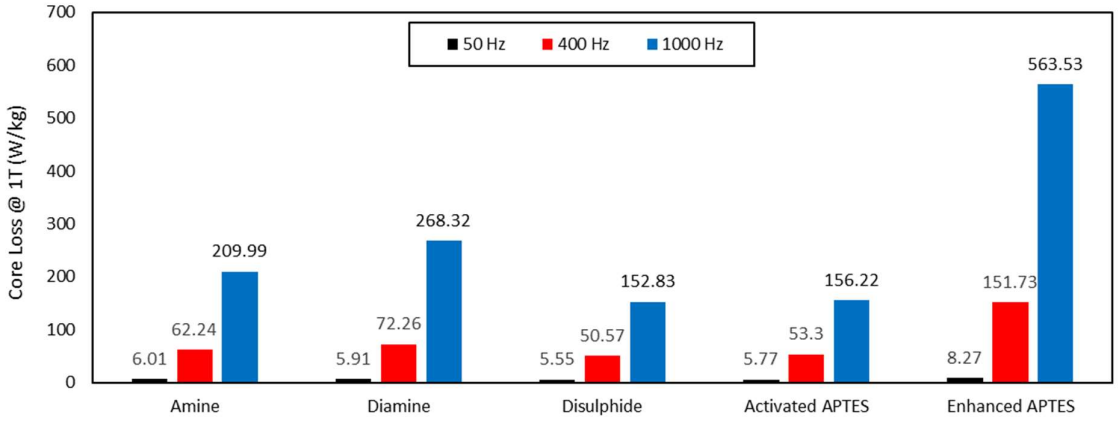

Figure 69: Core loss of silane-treated phosphated iron powder samples cured at 500°C

Figure 68 shows that the samples treated with the disulphide dipodal silane, activated APTES and enhanced APTES have superior permeability over those treated with the amine dipodal and diamine dipodal silanes, as evidence by a steeper gradient of hysteresis loop. Coercivity is relatively low across all of the samples, with the exception of the one treated with enhanced APTES, illustrated by a broader hysteresis loop. These results are reflected in Figure 69 which shows that the enhanced APTES treated phosphated iron powder sample has larger core loss than the other four samples at all frequencies measured. The combination of superior permeability and improved coercivity in the disulphide dipodal and activated APTES treated samples results in lower core loss across all frequencies measured. From these intial trials, the disulphide dipodal silane and activated APTES silane are selected for further investigation.

In order to find the effects of varying the amount of silane treatment on the properties of the sample, the wt% of the disulphide dipodal and the activated APTES mix were varied from 0.4 wt% to 0.7 wt% in 0.1 wt% increments. Figure 70a displays the core loss at 1 T and 1000 Hz against wt% silane, whilst Figure 70b shows the transverse rupture strength against wt% silane, for both of the selected silanes.

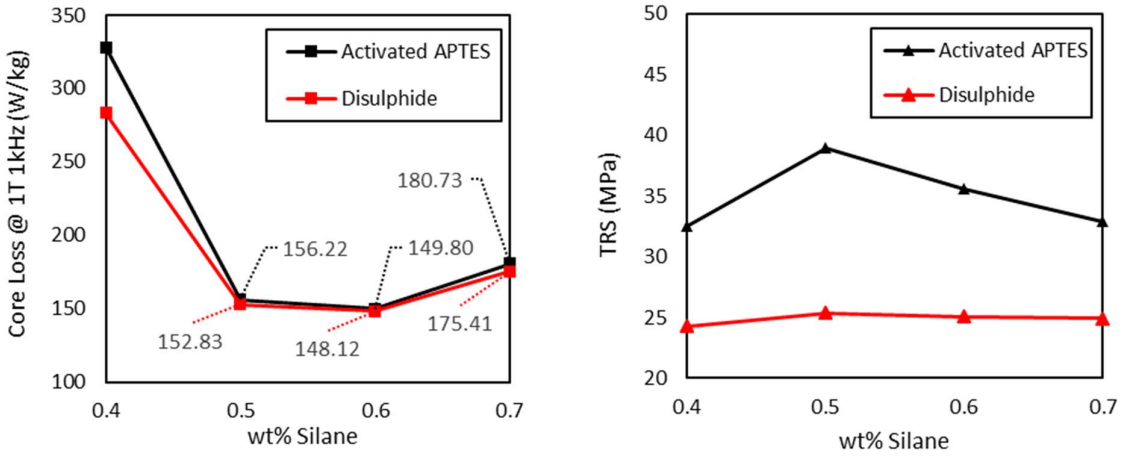

Figure 70: (a) Core loss at 1000 Hz and 1 T and; (b) TRS of activated APTES and disulphide treated phosphated iron powder samples

Figure 70a shows that core loss is lowest at 0.6 wt% silane for both the activated APTES and disulphide dipodal. This is the amount of silane where there is the optimal balance between the increased resistivity and decreased permeability offered by the increasing silane addition. The core loss of the disulphide dipodal treated samples is lower than that of the activated APTES treated samples at every wt% of silane measured. However, the difference at the optimised 0.6 wt% is very small and it should be highlighted that both phosphate-silane coatings have a core loss less than 150 W/kg at 1T and 1000 Hz, lower than any values obtained with liquid glass-based coatings [Chapter 5].

Figure 70b shows that strength is greatest at 0.5 wt% silane for both the activated APTES and disulphide dipodal. As silane addition increases, strength initially rises due to a higher cross linking density of the coupling agent. However, once a complete silane layer has formed on the iron, any additional silane has fewer or no vacant hydroxide ions to bond to on the surface of the iron powder. Combined with a thicker silane layer inhibiting the thermal oxidation bonding process, there is a resulting decrease in strength above 0.5 wt% silane. The strength of the activated APTES treated samples is greater than that of the disulphide dipodal treated samples at all wt% of silane measured, but it should be noted that neither silane offers the levels of strength obtained with liquid glass-based coatings [Chapter 5].

Table 28 presents a comparison between the phosphate - dipodal disulphide coated iron powder and commercially available Ancorlam. The phosphate-silane coated sample was cured at a slightly increased temperature to take advantage of the additional thermal stability offered by this coating system.

Composition	Curing Temp (°C)	TRS (MPa)	Resistivity (mΩcm)	H @ 1 T (A/m)	Core Loss @ 1 T (W/kg)		
					50 Hz	400 Hz	1 kHz
Ancorlam Control	450	37.90	15.22	3043	6.4	57.6	174.3
Phosphate-Dipodal Disulphide Silane	500	25.10	118.00	3097	5.3	50.3	148.1
Difference (%)	-	**-33.77%**	**675.30%**	**1.77%**	**-16.41%**	**-12.66%**	**-15.02%**

Table 28: Comparison of Ancorlam and phosphate-dipodal disulphide coated sample

Table 28 shows that the phosphate - dipodal disulphide coated sample possesses vastly improved resistivity over Ancorlam, and the required H-field for an induction of 1 T is within 2%, indicating only marginally decreased permeability. The increased curing temperature has allowed for further stress relief, offsetting the loss in permeability caused by adding extra coating material. Consequently, core loss is lower in the phosphate-silane sample at all frequencies measured. Whilst magnetic properties are superior, the strength of the phosphate-silane sample is significantly lower than Ancorlam, and that of the liquid-glass coated samples too [Chapter 5].

Table 29 presents a comparison between the phosphate - activated APTES coated iron powder and commercially available Ancorlam. Similarly to the phosphate - dipodal disulphide coated sample, the phosphate - activated APTES coated sample was cured at a slightly higher temperature to take advantage of the increased thermal stability.

Composition	Curing Temp (°C)	TRS (MPa)	Resistivity (mΩcm)	H @ 1 T (A/m)	Core Loss @ 1 T (W/kg)		
					50 Hz	400 Hz	1 kHz
Ancorlam Control	450	37.90	15.22	3043	6.4	57.6	174.3
Phosphate-Activated APTES Silane	500	35.58	59.95	2957	5.2	49.5	149.8
Difference (%)	-	-6.12%	293.89%	-2.83%	-18.75%	-13.99%	-14.06%

Table 29: Comparison of Ancorlam and phosphate-activated APTES coated sample

Table 29 shows that all magnetic properties are superior in the phosphate – activated APTES coated sample to that of Ancorlam. The addition of the silane surface treatment increases the thermal stability, allowing for a higher curing temperature, which offsets any loss in permeability from the addition of the silane layer. Mechanical strength is improved in comparison to the phosphate - disulphide dipodal coated sample, but still marginally worse than Ancorlam, due to the silane surface layer inhibiting the thermal oxidation bonding process.

Further increases in thermal stability would likely yield even greater magnetic performance and offset the decrease in strength, however phosphate degrades after curing above 530°C at low oxygen partial pressures, as per phase diagram in [79].

6.4 Conclusion

In this chapter, the use of silane coupling agents as part of a hybrid coating system was investigated. The research was broadly split into two parts; the use of dual silanes to bond inorganic coating materials on the base iron powder, and the use of a single silane in combination with a phosphate coating layer.

In the first part, dual silanes were used to coat inorganic materials onto the base iron powder. The most promising initial composition used APTES and a non-functional dipodal silane in a ratio of 5:1 to coat magnesium oxide onto the iron. Similarly, this dual silane approach was adapted to coat magnesium oxide onto phosphated powder to bolster the resistivity.

In the second part, five different alternative silanes were selected to be trialled as a surface treatment onto phosphated iron powder. Two silanes were taken forward into further trials after positive results, a disulphide functional dipodal silane and a functional silane mix known as “Activated APTES”. Table 30 presents the key properties of each of the four most promising samples from both part 1 and part 2, alongside an Ancorlam control sample. Green text highlights superior properties, whilst red text highlights worse properties in comparison to Ancorlam.

Coating	Curing Temp (°C)	TRS (MPa)	Resistivity (mΩcm)	H @ 1 T (A/m)	Core Loss @ 1 T (W/kg)		
					50 Hz	400 Hz	1 kHz
Ancorlam Control	450	37.90	15.22	3043	6.4	57.6	174.3
Dual Silane-MgO	450	**39.11**	**16.59**	**3304**	**6.3**	**58.0**	**170.1**
Phosphate-Dual Silane-MgO	450	**24.99**	**99.58**	**3559**	**6.0**	**56.4**	**166.5**
Phosphate-Disulphide Dipodal	500	**25.10**	**118.00**	**3097**	**5.3**	**50.3**	**148.1**
Phosphate - Activated APTES	500	**35.58**	**59.95**	**2957**	**5.2**	**49.5**	**149.8**
Phosphate - APTES	500	**55.50**	**181.83**	**2987**	**5.3**	**50.2**	**145.9**

Table 30: Comparison of Ancorlam and samples with silane-based coating systems

Table 30 shows that all five samples have promising magnetic properties, with lower overall core loss than Ancorlam at all frequencies measured. However, mechanical strength is generally lower, with only the dual silane - magnesium oxide coating system offering marginally greater strength than Ancorlam. The use of phosphating the base iron powder prior to silane treatment greatly increases resistivity at a cost to the mechanical strength. The phosphate layer inhibits the ability of the silane coupling agent to bond to the hydroxyl groups on the surface of the base iron powder. The lowest core loss values were obtained from the phosphate-silane coated samples, which was in part due to the increased thermal stability allowing for greater stress relief of the base iron.

The activated APTES silane treatment has the added advantage of a very fast reaction time, reacting in a matter of seconds rather than hours for conventional silanes [183]. This is a useful advantage when considering the economic implications of mass production. On the other hand, the disulphide dipodal is less hazardous than APTES, which is the main ingredient in the activated APTES mix, which is also a key consideration due to the large volumes required exceeding safe exposure limits during industrial production.

In summary, silane based coating systems offer superior magnetic properties over Ancorlam, at a cost of mechanical strength.

7 Conclusions & Further Work

7.1 Conclusions

In this thesis, novel coating systems for iron-based SMC materials were developed. The experimental work was split into two main parts; understanding current commercially available SMCs and applying this understanding to develop new SMC coating systems. The two classes of coating systems developed were liquid glass-based coatings and silane-based coatings. Liquid glass-based coating systems generally produced superior mechanical properties whilst silane-based coating systems generally produced superior magnetic properties.

The initial research problem involved the investigation into the drop in mechanical strength of commercially available Ancorlam powder at high density. This was concluded to be due to the lack of porosity inhibiting the thermal oxidation bonding process, which is responsible for the strength gain during heat treatment. This drop in strength at high density does not occur in competitor product Somaloy 700HR 5P due to the use of a coarser particle size allowing for larger pores. Therefore, the reason for the drop in strength of Ancorlam is down to the relatively fine particle size of the base A1000C iron powder upon which the phosphate coating system is applied.

The strengthening mechanism of Ancorlam powder was identified as thermal oxidation bonding. This process increases strength at a cost of resistivity. The feasibility of controlling the rate of oxidation was investigated, with the aim of achieving a balance of strength and resistivity to suit the particular application. The available oxygen was reduced in order to inhibit the oxidation bonding process. However, the required oxygen partial pressure for the oxidation of iron at the recommended curing temperature of Ancorlam powder remains many orders of magnitude below the minimum pressure that can be achieved inside the furnace.

The reduction of oxygen partial pressure in the furnace atmosphere by curing in a vacuum served to increase the initial rate of oxidation at the pressure and temperature range of the heat treatment process. In order to maximise the strength of Ancorlam powder, the oxygen partial pressure was minimised with a flow of 5% hydrogen in argon through the vacuum furnace acting as a reducing atmosphere. This yielded superior mechanical strength at low to medium densities, but the drop in strength of Ancorlam at the highest density remained due to the lack of porosity preventing the passage of gases into and out of the compacted powder. Therefore, an alternative strengthening mechanism was sought, in order to yield greater mechanical strength at high density, where magnetic properties are optimal.

Liquid glass was used as a binder material in conjunction with other highly resistive coating materials. The dispersion of ferrite and zinc oxide nanoparticles in the liquid glass as a coating system yielded superior mechanical strength and core loss at low frequency to Ancorlam, at a cost to the resistivity, permeability and core loss at high frequency. The combination of a phosphate base layer with liquid glass binder addition yielded superior strength, resistivity and core loss at all frequencies measured, at a cost of only permeability. This coating system has potential in many applications where the critical performance parameters include mechanical strength and core loss.

Silane coupling agents were used to adhere highly resistive coating materials to the base iron powder, and as a potential coating material in themselves. Highly resistive magnesium oxide was adhered to the iron through the use of a dual silane coupling agent, producing marginally improved strength, resisitivity and core loss to Ancorlam, at a small cost to permeability. The addition of a phosphate base coating to the dual silane magnesium oxide coating system yielded greatly improved resisitivity at a cost to permeability, as well as reduced strength as the phosphate coating inhibits the bonding of silane to the base iron.

The use of silanes as a coating material themselves was also investigated. The addition of a silane layer onto phosphated iron powder improved all magnetic properties in comparison to Ancorlam due to increased thermal stability from 450°C to 500°C allowing for greater stress relief of the base iron powder. However, this improvement in magnetic performance comes at a cost of reduced strength due to the coating material inhibiting the thermal oxidation bonding process.

In summary, the strengthening mechanisms of commercially available SMCs were investigated. For both SMCs studied, namely Ancorlam and Somaloy, the gain in strength during heat treatment was found to be due to thermal oxidation bonding. The formation of oxide bonds between particles increases strength at a cost of resistivity, and therefore a balance between the mechanical and magnetic properties must be found. The magnetic properties of existing commercially available SMCs deteriorate significantly after curing above a temperature of 450°C, due to the diffusion of iron through the coating which is then oxidised to form oxide bonds between the iron particles. This improved understanding of heat treatment mechanisms was used to create two new coating systems, namely liquid glass-based coatings with increased mechanical strength, and silane-based coating systems with improved magnetic properties over commercially available SMCs.

7.2 Further Work

7.2.1 Hybrid Glass-Silane Coating System

This thesis documented the development of two types of coating system; liquid glass-based and silane-based coatings. Liquid glass-based coating systems yield greater mechanical performance, whilst silane-based coating systems posess superior magnetic properties. Whilst these attributes are useful for specific applications, all round improved performance may be achieved by combining the superior properties of both. It is recommended to treat the iron powder with an initial layer of silane to produce a resistive layer that is well adhered to the base powder. A liquid glass coating would then be treated on top of the silane layer to provide additional binding strength and further resistivity to the SMC material.

7.2.2 Hybrid Lubricant-Coating Material

The coating systems developed as part of this research project possess superior properties over commercially available SMC materials, but still have poor permeability in comparison to existing laminate materials [Section 2.3.1]. The addition of any non-magnetic lubricant or coating material reduces the total available magnetic volume of the final composite material, and is therefore detrimental to permeability and saturation magnetisation. Furthermore, the deleterious effect of nonmagnetic regions are even more dominant than that of grain boundaries or dislocations, as these nonmagnetic regions act as internal demagnetising regions. The coating material also inhbits the compaction process, resulting in a lower final density than uncoated powder for equal compaction pressure. In order to address these issues, the amount of non-magnetic material addition should be minimised.

The SMC materials studied in this thesis utilise a lubricant to aid the compaction process, which is subsequently burnt off during the curing process. A hybrid lubricant-coating system, which acts as a lubricant during the compaction process, and reacts to form a resisitive coating after exposure to high curing temperatures would both reduce non-magnetic volume and aid compaction behaviour. Gelinas et al. developed an example of such a material, named ATOMET EM-1, which utilises a dielectric coating material which acts as a lubricant during compaction and an electrical insulator after heat treatment [152]. This is seen as a potential route of development for the silane-based coating systems described in Chapter 6, as the silane surface treatment can act as both a lubricating agent and a resisitive coating material [184].

7.2.3 Alternative Strengthening Mechanism

Current commercially available SMCs such as Ancorlam rely on thermal oxidation bonding during the curing process to increase the relatively poor strength attained in the green state. However, the formation of oxides comes at a cost to resitivity, which increases core loss of the final composite material. The use of a binder material can mitigate the strength losses, as was utilised in the liquid glass-base coating system developed in Chapter 5.

A more novel strengthening approach for SMC materials involves partial sintering of the coating to achieve the required mechanical strength. The processes of sintering standard iron powder and curing coated iron powder are fundamentally different. Sinter necks are driven by the elimination of surface energy, which is achieved by reducing the total surface area through atomic diffusion into the neck region. Surface oxides on the powder particles negatively affect the formation of sinter necks. Therefore, sintering atmospheres aim to prevent oxidisation and assist in the reduction of residual oxides from the power production process. Thus, we have a strengthening mechanism that hinges on the prevention of oxidisation. The theoretical potential involves a mechanically strong powder with no oxidation, thus retaining the resistivity of the coated powder.

One challenge is to find a coating material possessing greater resistivity than the oxide bonds, whilst being thermally stable at the required temperatures to form adequately strong sinter necks. The sintering process initiates at approximately half of the absolute melting temperature. This challenge may be mitigated using enhanced sintering methods, including hot pressing, phase stabilisation, activated sintering or liquid phase sintering. Another challenge is to ensure that the coating is sufficiently thick, such that formation of sinter necks does not cause contact between iron particles, but not too thick as to impact permeability and overall magnetic volume. This is another potential development route of the silane-based coating systems, already possessing increased thermal stability over commercially available phosphate-based SMCs. If these limits of thermal stability can be further increased, it may be possible to utilise this alternate strengthening mechanism.

7.2.4 SMC Modelling Software

As demonstrated by the experimental work in this thesis, the SMC production process involves multiple different process variables including coating material, composition, coating method, compaction parameters and heat treatment parameters. Consequently, developing new coating systems for SMC materials is very time consuming and resource heavy. The creation of modelling software to predict the material properties of a given coating mix or set of processing parameters could help to accelerate the advancement of SMCs. Using the knowledge gained from the extensive experimental work in this thesis, the development of such software is therefore recommended.

Bibliography

[1] P. Waide and C. U. Brunner, "Energy-Efficient Policy Opportunities for Electic Motor-Driven Systems," International Energy Agency, Paris, 2011.

[2] D. Hirst, "Electric vehicles and infrastructure," *House of Commons Library,* p. Briefing Paper Number 7480, 2020.

[3] Department for Enviornment, Food & Rural Affairs; Department for Transport, "UK plan for tackling roadside nitrogen dioxide concentrations," UK Governent, 2017.

[4] Committee on Climate Change, "Net Zero The UK's contribution to stopping global warming," 2019.

[5] HM Government Department for Transport, "The Road to Zero," 2018.

[6] International Air Transport Association (IATA), "Passenger Forecast Global Report 2019-02," 2019.

[7] H. Shokrollahi and K. Janghorban, "Soft magnetic composite materials (SMCs)," *Journal of Materials Processing Technology,* vol. 189, pp. 1-12, 2007.

[8] K. J. Sunday and M. L. Taheri, "Soft magnetic composites: recent advancements in the technology," *Metal Powder Report,* vol. 72, 2017.

[9] K. Ochiai, H. Horie, I. Arima and M. Morita, "Magnetic powder composition". United States Patent US4820338A, 11 04 1989.

[10] P. Viarouge, J. Cros and M. R. Dubois, "Experience with ATOMET Soft Magnetic Composites Properties, Pressing Conditions and Applications," in *UK Magnetic Society Seminar 16 November 2004*, 2004.

[11] J. Cros and P. Viarouge, "New Structures of Polyphase Claw-Pole Machines," *IEEE Transactions on Industry Applications,* vol. 40, no. 1, pp. 113-120, 2004.

[12] M. R. Dubois, L.-P. Lefebvre and E. Lemieux, "Compaction of SMC powders for high saturation flux density," in *Dusablon International Conference on Electrical Machines, Paper n. 230*, Grakow, Poland, 2004.

[13] I. Hemmati, H. R. Madaah Hosseini and A. Kianvash, "The correlations between processing parameters and magneticproperties of an iron–resin soft magnetic composite," *Journal of Magnetism and Magnetic Materials,* vol. 305, pp. 147-151, 2006.

[14] Hoeganaes Corporation, "Ancorlam Data Sheet," Cinnaminson, NJ, 2015.

[15] Höganäs AB, Processing Guidelines Somaloy 5P Materials, 2017.

[16] Cogent Power Ltd, "Electical Steel Thin Non-Oriented Grades," 2003.

[17] J. M. D. Coey, Magnetism and Magnetic Materials, Cambridge: Cambridge University Press, 2009.

[18] S. C. Hopkins, "Materials Science M13: Magnetic & Superconducting Materials Lecture Notes," University of Cambridge, 2014.

[19] H. Skarrie, "Design of Powder Core Inductors, PhD Thesis," Lund University, Lund, 2001.

[20] C. W. Chen, Magnetism and Metallurgy of Soft Magnetic Materials, New York: Dover Publications, 1986.

[21] N. A. Spaldin, Magnetic Materials: Fundamentals and Applications, 2nd Edition, Cambridge: Cambridge University Press, 2011.

[22] M. Anhalt, "Systematic investigation of particle size dependence of magnetic properties in soft magnetic composites," *Journal of Magnetism and Magnetic Materials,* vol. 320, pp. 366-369, 2008.

[23] B. D. Cullity and C. D. Graham, Introduction to Magnetic Materials, Second Edition, Piscataway: Wiley-IEEE, 2008.

[24] Muljadi, P. Sardjono and Suprapedi, "Preparation and Characterization of 5 wt.% Epoxy Resin Bonded Magnet NdFeB for Micro Generator Application," *Enery Procedia,* vol. 68, pp. 282-287, 2015.

[25] R. Allock, "Magnetic Measuring Techniques for Both Magnets and Assemblies," Arnold Magnetic Technologies, Sheffield, 2017.

[26] C. R. Hendricks, V. W. R. Amarakoon and D. Sullivan, "Processing of Manganese Zinc Ferrites for High-Frequency Switch-Mode Power Supplies," *Ceramic Bulletin,* vol. 70, pp. 817-823, 1991.

[27] H. Hojo, T. Kamijo, Y. Taniguchi, N. Akagi and H. Mitani, "Dust Core with Low Core-Loss for High-Frequency Applications," *Kobelco Technology Review,* vol. 35, pp. 23-27, 2017.

[28] G. Bertotti, F. Fiorillo and G. Soardo, "The Prediction of Power Losses in Soft Magnetic Materials," *Journal de Physique Colloques,* vol. 49, pp. C8 1915-1918, 1988.

[29] A. H. Taghvaei, A. Ebrahimi, K. Gheisari and K. Janghorban, "Analysis of the magnetic losses in iron-based soft magnetic composites with MgO insulation produced by sol–gel method," *Journal of Magnetism and Magnetic Materials,* vol. 322, pp. 3748-3754, 2010.

[30] D. Z. Xie, K. H. Lin and S. T. Lin, "Effects of processed parameters on the magnetic performance of a powder magnetic core," *Journal of Magnetism and Magnetic Materials,* vol. 353, pp. 34-40, 2014.

[31] K. J. Sunday, F. G. Hanejko and M. L. Taheri, "Magnetic and microstructural properties of Fe3O4-coated Fe powder soft magnetic composites," *Journal of Magnetism and Magnetic Materials,* vol. 423, pp. 164-170, 2017.

[32] R. M. German, Powder Metallurgy Science (2nd Ed.), Metal Powder Industry, 1994.

[33] W. B. James, "Powder Metallurgy Methods and Applications," in *Powder Metallurgy, Vol 7, ASM Handbook*, ASM International, 2015, pp. 9-19.

[34] J. P. Adams, "History of Powder Metallurgy," in *Powder Metallurgy, Vol 7, ASM Handbook*, ASM International, 2015, pp. 3-8.

[35] "Conventional Powder Metallurgy Process," Metal Powder Industries Federation, [Online]. Available: https://www.mpif.org/IntrotoPM/Processes/ConventionalPowderMetallurgy.aspx. [Accessed 01 01 2021].

[36] O. Bergman, "Studies of Oxide Reduction and Nitrogen Uptake in Sintering of Chromium-alloyed Steel Powder," KTH Royal Institute of Technology, Stockholm, Sweden, 2008.

[37] Höganäs AB, "Material and Powder Properties - Höganäs Handbook for Sintered Components," Höganäs AB, 2013.

[38] W. R. Nolan, "Electrically Insulating Phosphate Coatings for Iron Powder," Massachusetts Institute of Technology, Cambridge, USA, 2009.

[39] K. J. Sunday, "Development of Ferrite-Coated Soft Magnetic Composites: Correlation of Microstructure to Magnetic Properties," Drexel University, 2017.

[40] S. Kalpakjian, Manufacturing Engineering and Technology, India: Pearson Education, 2013.

[41] G. F. Bocchini, "Warm compaction of metal powders: why it works, why it requires a sophisticated engineering approach," *Powder Metallurgy,* vol. 42, no. 2, pp. 171-180, 1999.

[42] S. Buytoz, A. Orhan, A. K. Gur and U. Caligulu, "Microstructural Development of Fe–Cr–C and B4C Powder Alloy Coating on Stainless Steel by Plasma-Transferred Arc Weld Surfacing," *Arabian Journal for Science and Engineering,* vol. 38, pp. 2197-2204, 2013.

[43] B. AlMangour, "Chapter 2 - Powder Metallurgy of Stainless Steel: State-of-the-Art, Challenges and Development," in *Stainless Steel*, Nova Science Publishers, 2015, pp. 37-77.

[44] R. M. German, "1- Thermodynamics of Sintering," in *Sintering of Advanced Materials*, Woodhead Publishing, 2010, pp. 3-32.

[45] F. Magnussen, D. Svechkarenko, P. Thelin and C. Sadarangani, "Analysis of a PM Machine with Soft Magnetic Composites Core," KTH Royal Institute of Technology, 2004.

[46] E. Bayramli, O. Golgelioglu and H. Bulent-Ertan, "Powder metal development for electrical motor applications," *Journal of Materials Processing Technology,* vol. 161, no. 1-2, pp. 83-88, 2005.

[47] A. G. V. Hamler, B. Sustarsic and A. Sirc, "The use of soft magnetic composite materials in synchronous electric motor," *Journal of Magnetism and Magnetic Materials,* vol. 304, no. 2, pp. 816-819, 2006.

[48] D. E. Gay, "Soft magnetic composite materials for AC electrical applications," *Metal Powder Report,* vol. 52, pp. 42-45, 1997.

[49] Höganäs AB, "Somaloy 5P Material Data," 2018.

[50] L. Frayman, S. Quinn, R. Quinn, D. Green and F. Hanejko, "Advanced Soft Magnetic Materials for AC Applications with Reduced Iron Losses," *Powder Metallurgy,* vol. 58, no. 5, pp. 335-338, 2015.

[51] M. C. Levin, "Charakterisierung von weichmagnetischen Pulververbundwerkstoffen für den Einsatz in Traktionsantrieben," Technische Universitat Munchen, 2014.

[52] M. Karbowiak, B. Jankowski, M. Przybylski and B. Slusarek, "Influence of Grain Size on Mechanical Properties of Soft Magnetic Composites," *Euro PM2012 - PM Functional Materials,* 2012.

[53] R. O'Handley, Modern Magnetic Materials: Principles and Applications, New York: Wiley-Blackwell, 2000.

[54] R. Hilzinger and W. Rodewald, Magnetic Materials: Fundamentals, Products, Properties, Applications, Erlangen: Publicis Publishing, 2013.

[55] H. Gavrila and V. Ionita, "Crystalline and Amorphous Soft Magnetic Materials and their Applications - Status of Art and Challenges," *Journal of Optoelectronics and Advanced Materials,* vol. 4, no. 2, pp. 173-192, 2002.

[56] A. Krings, M. Cossale, A. Tenconi, J. Soulard, A. Cavagnino and A. and Boglietti, "Characteristics comparison and selection guide for magnetic materials used in electrical machines," *2015 IEEE International Electric Machines & Drives Conference (IEMDC),* pp. 1152-1157, 2015.

[57] B. D. Cullity and C. D. Graham, Introduction to Magnetic Materials, 2nd Ed, Hoboken: Wiley, 2011.

[58] D. Jiles, Introduction to Magnetism and Magnetic Materials, London: Chapman & Hall, 1998.

[59] N. Nishiyama, K. Tanimoto and A. Makino, "Outstanding efficiency in energy conversion for electric motors constructed by nanocrystalline soft magnetic alloy “NANOMET®” cores," *AIP Advances,* vol. 6, no. 055925, 2016.

[60] E. Y. Kang and Y. H. Chung, "Surface oxidation and magnetic properties of Fe-Si-B-Nb amorphous alloy," *IEEE Transactions on Magnetics,* vol. 45, pp. 2597-2600, 2009.

[61] C. Suryanarayana and C. C. Koch, "Nanocrystalline materials – Current research and future directions," *Hyperfine Interactions,* vol. 130, no. 1-4, pp. 5-44, 2000.

[62] K. Suzuki, A. Makino, N. Kataoka, A. Inoue and T. Masumoto, "High Saturation Magnetization and Soft Magnetic Properties of bcc Fe–Zr–B and Fe–Zr–B–M (M=Transition Metal) Alloys with Nanoscale Grain Size," *Materials Transactions, JIM,* vol. 32, no. 1, pp. 93-102, 1991.

[63] Y. Yoshizawa, S. Oguma and K. Yamauchi, "New Fe-based soft magnetic alloys composed of ultrafine grain structure," *Journal of Appled Physics,* vol. 64, pp. 6044-6046, 1988.

[64] A. Kojima, H. Horikiri, Y. Kawamura, A. Makino, A. Inoue and T. Masumoto, "Production of nanocrystalline b.c.c. Fe-Nb-B bulk alloys by warm extrusion and their magnetic properties," *Materials Science and Engineering,* Vols. A179-A180, pp. 511-515, 1994.

[65] H. Iwanabe, B. Lu, M. E. McHenry and D. E. Laughlin, "Thermal stability of the nanocrystalline Fe–Co-Hf-B-Cu Alloy," *Journal of Applied Physics,* vol. 85, pp. 4424-4426, 1999.

[66] W. J. Yuan, S. J. Pang, F. J. Liu and T. Zhang, "Frequency and magnetic field dependences of coercivity and core loss in Fe–Mo–Si–P–C–B amorphous alloys," *Journal of Alloys and Compunds,* vol. 504, pp. S142-S145, 2010.

[67] F. Fiorillo, G. Beriotti, C. Appino and M. Pasquale, "Soft Magnetic Materials," *Wiley Encyclopedia of Electrical and Electronics Engineering,* pp. 1-42, 2016.

[68] T. Liu, F. Li, A. Wang, L. Xie, Q. He, J. Luan, A. He, X. Wang, C. T. Liu and Y. Yang, "High performance Fe-based nanocrystalline alloys with excellent thermal stability," *Journal of Alloys and Compounds,* vol. 776, pp. 606-613, 2019.

[69] A. Krings, M. Cossale, A. Tenconi, J. Soulard, A. Cavagnino and A. Boglietti, "Magnetic materials used in electrical machines: a comparison and selection guide for early machine design," *IEEE Industry Applications Magazine,* vol. 23, pp. 21-28, 2017.

[70] E. Hirota, T. mihara, A. Ikeda and H. Chiba, "Hot-pressed Mn-Zn ferrite for magnetic recording heads," *IEEE Transactions on Magnetics,* vol. 7, pp. 337-341, 1971.

[71] H. Shokrollahi and K. Janghorban, "Influence of additives on the magnetic properties, microstructure and densification of Mn–Zn soft ferrites," *Materials Science and Engineering B,* vol. 141, pp. 91-107, 2007.

[72] J. Kulikowski and A. Lesniewski, "Properties of Ni-Zn Ferrites for Magnetic Heads: Technical Possibilities and Limitations," *Journal of Magnetism and Magnetic Materials,* vol. 19, pp. 117-119, 1980.

[73] E. Rezlescu, R. N, C. Pasnico, M. L. Craus and D. P. Popa, "The influence of additives on the properties of Ni-Zn ferrite used in magnetic heads," *Journal of Magnetism and Magnetic Materials,* vol. 117, pp. 448-454, 1992.

[74] A. Makino, A. Inoue and T. Masumoto, "Nanocrystalline soft magnetic Fe–M–B (M= Zr, Hf, Nb) alloys produced by crystallization of amorphous phase (overview)," *Materials Transactions, JIM,* vol. 36, no. 7, pp. 924-938, 1995.

[75] M. A. Willard and V. G. Harris, "Soft magnetic materials: Nanocrystalline alloys from amorphous precursors," *Journal of Metals,* vol. 54, no. 3, pp. 44-46, 2002.

[76] A. Makino, T. Kubota, C. Chang, M. Makabe and A. Inoue, "FeSiBP Bulk Metallic Glasses with Unusual Combination of High Magnetization and High Glass-Forming Ability," *Materials Transactions,* vol. 48, no. 11, pp. 3024-3027, 2007.

[77] M. E. McHenry, M. A. Willard and D. E. Laughlin, "Amorphours and nanocrytalline materials as applications as soft magnets," *Progress in Materials Science,* vol. 44, pp. 291-433, 1999.

[78] H. Okumura, D. J. Twisselmann, R. D. McMichael, M. Q. Huang, Y. N. Hsu, D. E. Laughlin and M. E. McHenry, "Magnetic and structural characterization and ferromagnetic resonance study of thin film HITPERM soft magnetic materials for data storage applications," *Journal of Applied Physics,* vol. 93, pp. 6528-6530, 2003.

[79] C. Oikonomou, R. Oro, E. Hryha and L. Nyborg, "Effect of Heat Treatment in Air on Surface Composition of Soft Magnetic Composite Components," *Materials Science and Engineering: B,* vol. 189, pp. 90-99, 2014.

[80] K. Asaka, C. Ishihara and T. Takata, "Proceedings of the Euro PM2004 Conference, Vienna, Austria," pp. 611-615, 2004.

[81] ASM Handbook, "Stress-Relief Heat Treating of Steel, Volume 1, 10th Edition," USA, 1009, pp. 33-34.

[82] I. Hemmati, H. R. M. Hosseini and A. Kianvash, "The correlations between processing parameters and magnetic properties of an iron-resin soft magnetic composite," *Journal of Magnetism and Magnetic Materials,* vol. 305, pp. 147-151, 2006.

[83] G. Uozumi, M. Watanabe, R. Nakayama, K. Igarashi and K. Morimoto, "Properties of Soft Magnetic Composite with Evaporated MgO Insulation Coating for Low Iron Loss," *Materials Science Forum,* Vols. 534-536, pp. 1361-1364, 2007.

[84] C. Oikinonmou, "PhD Thesis: On Surface Characteristics and Microstructural Development of Soft Magnetic Composite Powder and Components," Chalmers University, Gothenburg, 2015.

[85] M. Przybylski, D. Kapelski and B. Slusarek, "Mechanical Properties of SMCs at the Temperature of Liquid Nitrogen," *Acta Physcia Polonica A,* vol. 131, pp. 1199-1203, 2017.

[86] L. Xiao, Y. Sun, C. Ding, L. Yang and Y. L, "Annealing effects on magnetic properties and strength of organic-silicon epoxy resin-coated soft magnetic composites," *Journal of Mechanical Engineering Science,* vol. 228, no. 12, pp. 2049-2058, 2014.

[87] P. Kollar, Z. Bircakova, J. Fuzer, R. Bures and M. Faberova, "Power loss separation in Fe-based composite materials," *Journal of Magnetism and Magnetic Materials,* vol. 327, pp. 146-150, 2013.

[88] M. Streckova, E. Medvecky, J. Fuzer, P. Kollar, R. Bures and M. Faberova, "Design of Novel Soft Magnetic Composites Based on Fe-Resin Modified with Silica," *Material Letters,* vol. 101, pp. 37-40, 2013.

[89] A. H. Taghvaei, H. Shokrollahi and K. Janghorban, "Properties of iron-based soft magnetic composite with iron phosphate–silane insulation coating," *Journal of Alloys and Compounds,* vol. 481, pp. 681-686, 2009.

[90] M. Huang, C. Wu, J. Y and M. Yan, "Evolution of phosphate coatings during high-temperature annealing and its influence on the Fe and FeSiAl soft magnetic composites," *Journal of Alloys and Compounds,* vol. 644, pp. 124-130, 2015.

[91] S. Lee, M. Choi and J. Kim, "Magnetic Properties of Pure Iron Soft Magnetic Composites Coated by Manganese Phosphates," *IEEE Transactions on Magnetics,* vol. 53, no. 11, 2017.

[92] K. J. Sunday, K. A. Darling, F. G. Hanejko, B. Anasori, Y. C. Liu and M. L. Taheri, "Al2O3 'self-coated' iron powder composites via mechanical milling," *Journal of Alloys and Compounds,* vol. 653, pp. 61-68, 2015.

[93] F. Jay, V. Gauthier and S. Dubois, "Iron Particles Coated with Alumina: Synthesis by a Mechanofusion Process and Study of the High-Temperature Oxidation Resistance," *Journal of the American Ceramics Society,* vol. 89, no. 11, pp. 3522-3528, 2006.

[94] M. Yaghtin, A. H. Taghvaei, B. Hashemi and K. Jangorban, "Effect of heat treatment on magnetic properties of iron-based soft magnetic composites with Al2O3 insulation coating produced by sol–gel method," *Journal of Alloys and Compounds,* vol. 581, pp. 293-297, 2013.

[95] H. Y. Jiang, W. Zhong, X. L. Wu, N. J. Tang, W. Liu and Y. W. Du, "Direct and alternating current magnetic properties of FeNi particles coated with SiO2," *Journal of Alloys and Compounds,* vol. 384, pp. 264-267, 2004.

[96] H. Brunckova, M. Kabatova and E. Dudrova, "The effect of iron phosphate, alumina and silica coatings on the morphology of carbonyl iron particles," *Surface and Interface Analysis,* vol. 42, pp. 13-20, 2009.

[97] B. Yang, Z. Wu, Z. Zou and R. Yu, "High-performance Fe/SiO2 soft magnetic composites for low-loss and high-power applications," *journal of Physics D: Applied Physics,* vol. 43, pp. 1-6, 2010.

[98] M. Streckova, J. Fuzer, L. Medvecky, R. Bures, P. Kollar, M. Faberova and V. Girman, "Characterization of composite materials based on Fe powder (core) and phenol–formaldehyde resin (shell) modified with nanometer-sized SiO2," *Bulletin of Materials Science,* vol. 37, pp. 167-177, 2014.

[99] T. A. Laxminarayana, S. K. Manna, B. G. Fernandes and N. Venkataramani, "Study of AC Magnetic Properties and Core Losses of Fe/Fe3O4-Epoxy Resin Soft Magnetic Composite," *Physics Procedia; 20th International Conference on Magnetism,* vol. 75, pp. 1396-1403, 2015.

[100] H. Gheisari, S. Javadpour, H. Shokrollahi and B. Hashemi, "Magnetic losses of the soft magnetic composites consisting of iron and Ni–Zn ferrite," *Journal of Magnetism and Magnetic Materials,* vol. 320, no. 8, pp. 1544-1548, 2008.

[101] M. Lauda, J. Fuzer, P. Kollar, M. Streckova, R. Bures, J. B. M. Kovac and I. Batko, "Magnetic properties and loss separation in FeSi/MnZnFe2O4 soft magnetic composites," *Journal of Magnetism and Magnetic Materials,* vol. 411, pp. 12-17, 2016.

[102] M. Wang, Z. Zan, N. Deng and Z. Zhao, "Preparation of pure iron/Ni–Zn ferrite high strength soft magnetic composite by spark plasma sintering," *Journal of Magnetism and Magnetic Materials,* vol. 361, pp. 166-169, 2014.

[103] W. Li, W. Wang, J. Lv, Y. Ying, J. Yu, J. Zheng, L. Qiao and S. Che, "Structure and magnetic properties of iron-based soft magnetic composite with Ni-Cu-Zn ferrite silicone insulation coating," *Journal of Magnetism and Magnetic Materials,* vol. 456, pp. 333-340, 2018.

[104] Y. Peng, J. Nie, W. Zhang, C. Bao, J. Ma and Y. Cao, "Preparation of soft magnetic composites for Fe particles coated with (NiZn)Fe2O4 via microwave treatment," *Journal of Magnetism and Magnetic Materials,* vol. 395, pp. 245-250, 2015.

[105] S. Wu, A. Sun, W. Xu, Q. Zhang, F. Zhai, P. Logan and A. A. Volinsky, "Iron-based soft magnetic composites with Mn–Zn ferrite nanoparticles coating obtained by sol–gel method," *Journal of Magnetism and Magnetic Materials,* vol. 324, no. 22, pp. 3899-3905, 2012.

[106] A. Goldman, Modern Ferrite Technology, 2nd Edition, Springer, 2006.

[107] G. Zhao, C. Wu and M. Yan, "Enhanced magnetic properties of Fe soft magnetic composites by surface oxidation," *Journal of Magnetism and Magnetic Materials,* vol. 399, pp. 51-57, 2016.

[108] G. Zhao, C. Wu and M. Yan, "Evolution of the insulation matrix and influences on the magnetic performance of Fe soft magnetic composites during annealing," *Journal of Alloys and Compounds,* vol. 685, pp. 231-236, 2016.

[109] L. L. Evangelista, G. Tontini, A. I. Ramos Filho, L. E. Machado, B. S. Silva, I. P. C. Silva, G. Hammes, R. Binder, C. Binder, N. J. Batistela, A. N. Klein and V. Drago, "Developments on soft magnetic composites with double layer insulating coating: Synergy between ZnO and B2O3," *Journal of Magetism and Magnetic Materials,* vol. 497, p. 166023, 2020.

[110] W. Xu, C. Wu and M. Yan, "Preparation of Fe–Si–Ni soft magnetic composites with excellent high-frequency properties," *Journal of Magnetism and Magnetic Materials,* vol. 381, pp. 116-119, 2015.

[111] S. Wu, A. Sun, Z. Lu, C. Cheng and X. Gao, "Magnetic properties of iron-based soft magnetic composites with SiO2 coating obtained by reverse microemulsion method," *Journal of Magnetism and Magnetic Materials,* vol. 381, pp. 451-456, 2015.

[112] P. Jansson and L. A. Larsson, "US Patent". USA Patent 6,346,265, 23 Feb 1996.

[113] N. Bay, A. Azushim, P. Groche, I. Ishibashi, M. Merklein, M. Morishita, T. Nakamura, S. Schmid and M. Yoshida, "The state of the art in cold forging lubrication," *Journal of Materials Processing Technology,* vol. 46, pp. 19-40, 1994.

[114] Höganäs AB, Processing Guidelines Somaloy 1P Materials, 2017.

[115] P. Jansson, "Heat treating of magnetic iron powder". WO Patent WO1995029490A1, 02 11 1995.

[116] K. S. Narasimhan and C. Schade, "Iron-Silicon Water Atomized Powders for Electromagnetic Applications," in *World Congress on Powder Metallurgy and Particulate Materials*, Orlando, Florida, 2014.

[117] Höganäs AB, Production of Sintered Components Handbook, 2013.

[118] M. Renowden and P. Pourtalet, "Experimental studies on lubricant removal," *Metal Powder Report,* vol. 45, no. 9, pp. 625-628, 1990.

[119] L. P. Lefebvre, I. P. Swainson, Y. Deslandes, G. Pleizier and P. Chartrand, "Microstructure and properties of heat treated iron powder compacts intended for ac soft magnetic applications," *Materials Science and Technology,* vol. 17, pp. 45-53, 2001.

[120] L. P. Lefebvre, S. Pelletier and C. Gelinas, "Iron Compacts for Low Frequency AC Magnetic Applications - Effect of Thermal Treatments," *Advances in Powder Metallurgy & Particulate Materials,* vol. 2, no. 8, pp. 61-73, 1998.

[121] Höganäs AB, "Processing Guidelines Somaloy 3P Materials," 2017.

[122] K. S. Narasimhan, F. G. Hanejko and M. L. Marucci, "Effect of Particle Size and 2P2C Technology on the Soft Magnetic Properties of Composite Iron Compacts," in *APMA International Conference*, Yokohama, Japan, 2012.

[123] Hoeganaes Corporation, "Ancorsteel 1000C Data Sheet," Cinnaminson, NJ, 2015.

[124] K. Sunday, "Email from Kaite Jo Sunday of Hoeganaes Coorporation on 1st May 2018".

[125] Z. Ye and B. Skårman, "The Effect of Manufacturing Processes on the Properties of Multi-layer Coated SMC Components," *WorldPM Conference,* pp. 1-6, 2016.

[126] PowderTech, "Manganese Ferrite M035 Safety Data Sheet," 2019.

[127] Q. Xu, S. Zhou and H. Schmidt, "Magnetic properties of ZnO nanopowders," *Journal of Alloys and Compounds,* vol. 487, no. 1-2, pp. 665-667, 2009.

[128] Sigma Aldrich, "Aluminium Oxide Safety Data Sheet," 2021.

[129] Sigma Aldrich, "Magnesium Oxide Safety Data Sheet," 2021.

[130] Sigma Aldrich, "Zinc Oxide Safety Data Sheet," 2021.

[131] VWR Chemical, "Sodium Silicate Technical Solution - Safety Data Sheet v7.2," 2021.

[132] Diatom, "R2447 Sodium Silicate Solution - Safety Data Sheet," 2021.

[133] Gelest Inc, "SIA0610.0 - 3-AMINOPROPYLTRIETHOXYSILANE Safety Data Sheet," 2015.

[134] Gelest, Inc, "SIG5840.0 - (3-GLYCIDOXYPROPYL)TRIMETHOXYSILANE Safety Data Sheet v2.0," 2016.

[135] Gelest, Inc, "SIB1817.0 - 1,2-BIS(TRIETHOXYSILYL)ETHANE Safety Data Sheet v2.5," 2019.

[136] Gelest, Inc, "SIB1833.0 - BIS(3-TRIMETHOXYSILYLPROPYL)AMINE, 96% Safety Data Sheet v2.0," 2019.

[137] Gelest, Inc, "SIB1834.0 - N,N'-BIS[3-(TRIMETHOXYSILYL)PROPYL] ETHYLENEDIAMINE, 62% in methanol Safety Data Sheet," 2015.

[138] Gelest, Inc, "SIB1824.6 - BIS[3-(TRIETHOXYSILYL)PROPYL]DISULFIDE, 90% Safety Data Sheet," 2015.

[139] Gelest, Inc, "SIA0610.E1 - SIVATE™ E610: ENHANCED AMINE FUNCTIONAL SILANE Safety Data Sheet v1.3," 2019.

[140] Gelest, Inc, "SIA0610.A1 - SIVATE™ A610: ACTIVATED AMINE FUNCTIONAL SILANE Safety Data Sheet v1.2," 2018.

[141] Y. Thomas, D. Bernier, S. St Laurent and V. Paris, "Effect of Lubricant Particle Size Distribution on the Processing and Properties of P/M Ferrous Parts," *Euro PM2013 - Lubricants,* 2013.

[142] Avantor, "Image of 3 Dimensional shaker, Turbula® T 2 F," VWR International, [Online]. Available: https://uk.vwr.com/store/product/3222118/3-dimensional-shaker-turbula-t-2-f. [Accessed 21 01 2021].

[143] International Organisation for Standardisation, "ISO 3995, Metallic powders — Determination of green strength by transverse rupture of rectangular compacts," 1996.

[144] International Organisation for Standardisation, "ISO 3325, Sintered metal materials, excluding hardmetals - Determination of transverse rupture strength," 1996.

[145] ASTM International, "ASTM-A712, Standard Test Method for Electrical Resistivity of Soft Magnetic Alloys," 2014.

[146] ASTM International, "ASTM A927: Standard Test Methods for Alternating-Current Magnetic Properties of Toroidal Core Specimens Using te Voltmeter-Ammeter-Wattmeter Method," 2018.

[147] G. Tontini, L. L. Evangelista, A. I. Ramos Filho, R. I. Elias, G. Hammes, N. J. Batistela, C. Binder, A. N. Klein and V. Drago, "Study of soft magnetic composites of iron coated with nanoparticles dispersion in liquid glass," *Journal of Magnetism and Magnetic Materials,* vol. 487, p. 165351, 2019.

[148] Y. Yi, Y. Peng, C. Xia, L. Wu, X. Ke and J. Nie, "Influence of heat treatment on microstructures and magnetic properties of Fe-based soft magnetic composites prepared by co-precipitation method," *Journal of Magnetism and Magnetic Materials,* vol. 476, pp. 100-105, 2019.

[149] K. Ouda, H. Danniger, C. Gierl-Mayer, R. Hellein and A. Müller, "Ferrothermal reduction of iron(III)phosphate insulating layers in soft magnetic composites," *Powder Metallurgy,* p. DOI: 10.1080/00325899.2021.1909211, 2021.

[150] C. Oikonomou, E. Hryha and L. Nyborg, "An XPS investigation on the thermal stability of the insulating surface layer of soft magnetic composite powder," *Surface and Interface Analysis,* vol. 48, pp. 445-450, 2016.

[151] R. Bidulsky, J. Bidulska, R. De Oro, E. Hryha, M. M. I. Forno and M. Actis Grande, "Interparticle Neck Connections in Innovative Insulated Iron Powder Compounds," *Acta Physica Polonica,* vol. 128, pp. 647-650, 2015.

[152] C. Gelinas, S. Pelletier, P. Lemieux and L. Azzi, "Properties and Processing of Improved SMC Materials," *Advances in Powder Metallurgy and Particulate Materials,* vol. 9, pp. 108-120, 2005.

[153] S. Rebeyrat, J. L. Grosseau-Poussard, J. F. Dinhut and P. O. Remault, "Oxidation of Phosphated Iron Powders," *Thin Solid Films,* pp. 139-146, 2000.

[154] H. E, S. Karamchedu and L. Nyborg, "Delubrication of PM Components Based on Cr Prealloyed Steel Powder Chances and Risks," *Euro PM2011,* vol. 3, pp. 105-110, 2011.

[155] S. Karamchedu, E. Hryha and L. Nyborg, "Influence of Process Parameters on the Delubrication of PM Steels," *Powder Metallurgy Progress,* vol. 11, pp. 90-96, 2011.

[156] R. K. Rajput, A Textbook of Engineering Thermodynamics, 4th Edition, New Dehli: Laxmi Publications Ltd, 2010.

[157] D. R. Gaskell, Introduction of the Thermodynamics of Materials, 4th Edition, New York: Taylor & Francis, 2003.

[158] R. J. Hussey and M. Cohen, "The oxidation of Fe in the temperature range 450-550°C - I. The pressure range 10-6 - 10-4 torr," *Corrosion Science,* vol. 11, no. 10, pp. 699-711, 1971.

[159] R. J. Hussey and M. Cohen, "The oxidation of Fe in the temperature range 450 - 550°C - II. The pressure range 10-3 - 760 torr," *Corrision Science,* vol. 11, no. 10, pp. 713-721, 1971.

[160] W. E. Boggs, R. H. Kachik and G. E. Pellissier, "The Effect of Oxygen Pressure on the Oxidation of Zone-Refined Iron," *Journal of the Electrochemical Society,* vol. 112, pp. 539-546, 1965.

[161] D. Caplan, M. J. Graham and M. Cohen, "Effect of Oxygen Pressure and Experimental Method on the High Temp Oxidation of Pure Fe," *Corrosion Science,* vol. 10, pp. 1-8, 1970.

[162] S. Pelletier, L. P. Lefebvre and C. Gelinas, "Resin Impregnation of Soft Magnetic Materials for Low Frequency Applications"," *Advances in Powder Metallurgy & Particulate Materials,* vol. 1, p. 27, 1997.

[163] Organisation for Economic Co-operation and Development, "SIDS Initial Assessment Report for SIAM 18," Paris, France, 2004.

[164] C. H. Baehr and W. Koehl, "Soluble Silicates - Highly Versatile and Safe," *International Journal for Applied Science,* vol. 133, pp. 88-94, 2007.

[165] Human & Enviornmental Risk Assessment (HERA), "HERA Risk Assessment of Soluble Silicates," 2005.

[166] PQ Europe, "Sodium and Potassium Silicates: Versatile Compounds for your Applications," 2004.

[167] PQ Corporation, "PQ Sodium Silicates: Liquids and Solids," 2004.

[168] CEES Centre Europeen D'Etudes Des Silicates, "Soluble Silicates: Chemical, Toxicological, Ecological and Legal Aspects of Production, Transport, Handling and Application," 2019.

[169] Y. Peng, Y. Yi, L. Li, H. Ai, X. Wang and L. Chen, "Fe-based soft magnetic composites coated with NiZn ferrite prepared by a co-precipitation method," *Journal of Magnetism and Magnetic Materials,* vol. 428, pp. 148-153, 2017.

[170] Z. Zhong, Q. Wang, L. Tao, L. Jin, X. Tang, F. Bai and H. Zhang, "Permeability Dispersion and Magnetic Loss of Fe NixZn1−xFe2O4 Soft Magnetic Composites," *IEEE Transactions on Magnetics,* vol. 48, no. 11, pp. 3622-3625, 2012.

[171] M. Streckova, R. Bures, M. Faberova, P. Kurek, P. Roupcova, H. Hadraba, V. Girman and J. Strecka, "A Novel Composite Material Designed from FeSi Powder and Mn0. 8Zn0. 2Fe2O4 Ferrite," *Advances in Materials Science and Engineering,* pp. 1-8, 2015.

[172] I. Chicinas, T. F. Marinca, B. V. Neamtu, P. Pascuta and V. Pop, "Thermal stability of the manganese-nickel mixed ferrite and iron phases in the Mn0.5Ni0.5Fe2O4 Fe composite nanocomposite powder," *Journal of Thermal Analysis and Calorimetry,* vol. 118, pp. 1269-1275, 2014.

[173] F. Sánchez, A. Bolarín, P. Molera, J. Mendoza and M. Ocampo, "Relationship between particle size and manufacturing processing and sintered characteristics of iron powders," *Revista Latinoamericana de Metalurgia y Materiales,* vol. 23, no. 1, pp. 35-40, 2003.

[174] K. J. Sunday and M. L. Taheri, "NiZnCu-ferrite coated iron powder for soft magnetic composite applications," *Journal of Magnetism and Magnetic Materials,* vol. 463, pp. 1-6, 2018.

[175] E. P. Plueddemann, Silane Coupling Agents, New York: Springer, 1982.

[176] Gelest Inc, "Silane Coupling Agents," 2014.

[177] W. Aichele and H. P. Koch, "Soft magnetic, deformable composite material and process for producing the same". United States Patent US6537389B1, 14 08 1997.

[178] A. H. Taghvaei, H. Shokrollahi, A. Ebrahimi and K. Janghorban, "Soft magnetic composites of iron-phenolic and the influence of silane coupling agent on the magnetic properties," *Materials Chemistry and Physics,* vol. 116, pp. 247-253, 2009.

[179] M. K. Chaudhury, T. M. Gentle and E. P. Plueddemann, "Adhesion mechanism of polyvinyl chloride to silane primed metal surfaces," *Journal of Adhesion Science and Technology,* vol. 1, pp. 29-38, 1987.

[180] X. Jianwen and C. P. Wong, "Characterization and properties of an organic–inorganic dielectric nanocomposite for embedded decoupling capacitor applications," *Composites Part A: Applied Science and Manufacturing,* vol. 38, no. 1, pp. 13-19, 2007.

[181] Gelest Inc, "Special Topics - Dipodal Silanes," 2006.

[182] L. F. Fan, H. I. Hsiang and J. J. Hung, "Silane surface modification effects on the electromagnetic properties of phosphatized iron-based SMCs," *Applied Surface Science,* vol. 433, pp. 133-138, 2018.

[183] Gelest Inc, "Sivate A610 Activated Amine Functional Silane," 2016.

[184] M. Kejzelman, P. Skoglund, O. Andersson, P. Knutsson, H. Vidarsson and B. Skårman, "Iron-based powder". United States Patent US7153594B2, 23 12 2003.